First-Principles study of Structural, Elastic and Electronic Properties of AlN and GaN Semiconductors under Pressure Effect and Magnetism in AlN:Mn and GaN:Mn systems

Mohammed Benali Kanoun

▶ To cite this version:

Mohammed Benali Kanoun. First-Principles study of Structural, Elastic and Electronic Properties of AlN and GaN Semiconductors under Pressure Effect and Magnetism in AlN:Mn and GaN:Mn systems. Material chemistry. Université de Tlemcen, 2004. English. NNT : . tel-00009654

HAL Id: tel-00009654
https://theses.hal.science/tel-00009654

Submitted on 3 Jul 2005

HAL is a multi-disciplinary open access archive for the deposit and dissemination of scientific research documents, whether they are published or not. The documents may come from teaching and research institutions in France or abroad, or from public or private research centers.

L'archive ouverte pluridisciplinaire **HAL**, est destinée au dépôt et à la diffusion de documents scientifiques de niveau recherche, publiés ou non, émanant des établissements d'enseignement et de recherche français ou étrangers, des laboratoires publics ou privés.

DEMOCRATIC AND POPULAR REPUBLIC OF ALGERIA
MINISTRY OF HIGH EDUCATION AND SCIENTIFIC RESEARCH

THESIS

Presented at

ABOU-BAKR BELKAID UNIVERSITY - TLEMCEN
FACULTY OF SCIENCES – PHYSICS DEPARTMENT

To obtain the degree of

DOCTOR OF PHYSICS

Option: MATERIALS SCIENCE

By

Mr KANOUN Mohammed Benali

Theme

First-Principles study of Structural, Elastic and Electronic Properties of AlN and GaN Semiconductors under Pressure Effect and Magnetism in AlN:Mn and GaN:Mn systems

At 7 November 2004 with the board of examiners:

Mr B. BENYOUCEF	**Chairman**	Professor	University of Tlemcen
Mr G. MERAD	**Thesis Advisor**	Professor	University of Tlemcen
Mr H. AOURAG	**Examiner**	Professor	University of Belfort
Mr J. CIBERT	**Examiner**	Director of Research	University of Grenoble I
M^r A-E. KADOUN	**Examiner**	Professor	University of Sidi Bel Abbès
Mr B. KHELIFA	**Examiner**	Professor	University of Artois

Laboratoire d'Etude et Prédiction de Matériaux
Unité de Recherche Matériaux et Energies Renouvelables

DEDICATIONS

I dedicate this thesis to :

My lovely parents

My very dear Souraya

My brothers Mohammed Adil and Ahmed-Ali

My Sisters as well as their husbands

My nieces' pair, my well liked Sannae and Rawida.

KANOUN Mohammed Benali

Acknowledgments

This Thesis is realized within the « Laboratoire d'Etude et Prédiction de Matériaux, Unité de Recherche Matériaux et Energies Renouvelables» at Abou-Bekr Belkaid University of Tlemcen.

I hold to express my deep gratitude to Mr. Ghouti MERAD, Professor at University of Tlemcen and my thesis advisor, to have guided me all along this work, for his permanent follow-up, his attentive readings like for his confidence and the liberty that he has left me during these years of research.

I would like to thank Mr. B BENYOUCEF Professor at University of Tlemcen, to have accepted to chair the jury of this thesis.

I hold to present my thanks to Mr. H. AOURAG, Professor at University of Belfort-Montbéliard (France), Mr. J. CIBERT, Director of Research (CNRS) at J. Fourier University of Grenoble I (France), Mr. A-E. KADOUN Professor at University of Sidi Bel Abbès, and Mr. B. KHELIFA, Professor at University of Artois (France), that makes me honor to judge this thesis.

I thank particularly Mr. Joël CIBERT, Director of Research at University of J. Fourier, Grenoble I, which has welcomed me within its laboratory "Laboratoire de Spectrométrie Physique, UMR 588, CNRS, Université de Grenoble I". That he finds here, the expression of my high consideration and my deep respect.

I hold to warmly thank my brother and my faithful friend, Mr. Abdelkarim MERAD for his assistance, his support, his councils and his contribution to the outcome of this thesis.

I hold highly to express my deep recognition and my gratitude to Mrs. S. GOUMRI-SAID, for the precious assistance that she has provide me, the encouragements that she has not ceased to lavish me all along this work and his contribution to the outcome of this thesis

I thank particularly Dr. Hervé BOUKARI, Dr. Régis ANDRE and for their assistance concerning of bibliography. I wish to thank Dr. Thierry DEUTSCH, for his assistance with the computer code in CEA (Grenoble).

I hold to thank highly my dear brother Mr. Mohammed Adil KANOUN for his assistance, his support, his confidence and his councils during these years of research.

I thank particularly D.R. LE SI DANG, D.R. H MARIETTE, Dr. D. FERRAND, D.R. S TATARENKO, D.R. J BLEUSE, Dr. M BETOLINI for their assistance and their fruitful scientific discussions that me have a lot enriched and guided. Without forgetting Mr. Y. GENUIST that was always available to help us (thank you). I express my sincere salutations to my dear friend Mr L MAINGAULT.

I express my sincere salutations to my dear most intimate friends, to members of the "Laboratoire d'Etude et Prédiction de Matériaux", the members of "Unité de Recherche Matériaux et Energies Renouvelables" and thus to all my colleagues of the Physics Department.

Contents

Nomenclature...…………………………………………………………………... iv

List of figures……………………………………………………………………. v

List of tables……………………………………………………………………... viii

Introduction ………………………………………………………………….... 1

I. Group III-Nitride semiconductors - AlN and GaN - 5

I.1. Current interest……..……………………..…………………………………… 6

I.2. III-Nitrides physical properties..……………………………………………… 7

II.2.1. Some basic material properties…..………………………………….……. 7

II.2.2. Common crystal structures………...…………………………………….…... 9

II.2.3. Phase Diagram……………………….…………………………………… 10

II.3. Technological applications……..……………………………..……………………. 11

II.3.1. Light-emitting diodes (LEDs)………………………………...…….……. 11

II.3.2. Laser diodes (LEDs)…………………........……………………..…............. 12

II.3.3. UV detectors……………………………………..……………………. 13

References……………………………………………………………………………… 14

II. Diluted magnetic semiconductors - DMS - 18

II.1. Spintronics………………………..……………………………………………… 19

II.2. Diluted magnetic semiconductors…..……………………………….………... 21

II.3. Ferromagnetic semiconductors……..………………………………………… 24

II. 4. III-Nitrides based diluted magnetic semiconductors…………………………... 27

References……………………………………………………………………….. 28

III. Density functional theory - DFT - 32

III.1. Introduction…………………………………………………………………… 33

III.2. The basic principles of the method……………………………………………. 35

III.3. The local –(spin-) density approximation (LDA, LSDA)……………………… 37

III.4. Generalized gradient approximation (GGA)………………………………... 38

III.5. Single particle Kohn-Sham equation………………………………………….. 38

III.6. The basis sets…………………………………………………………………... 42

III.7. The self consistent field in DFT……………………………………………... 42

References………………………………………………………………………. 44

IV. Full potential linearized / augmented plane wave plus local orbitals – FP-L/APW+lo – 45

IV.1. The augmented plane wave method (APW) ……...…………………………… 46

IV.2. The linearized augmented plane wave method (LAPW)…...………………….. 49

IV.3. The augmented plane wave plus local orbitals method (APW+lo)…...………... 50

IV.4. The full potential calculation…………………………………….………….. 52

References……………………………………………………………………… 53

V. Results and discussions 54

V. Part I: properties of AlN and GaN compounds 55

V.I.1. Numerical details…………………………………………………………… 55

V.I.2. Structural properties……………………………………………………….… 58

V.I.2.1.Zincblende phase ……………………………………………….. 58

V.I.2.2.Wurtzite phase ………..……………………………………………. 61

V.I.2.3. Rocksalt phase…………………………….…………………… 67

V.I.2.1.The relative stability and phase transitions……..………………... 69

V.I.3. Electronic properties……………………….…………………………….. 73

V.I.3.1 Band structures……………………….…………..…………….. 73

V.I.3.1.1. AlN compound ……………...………………………... 73

V.I.3.1.2. GaN compound ……………………………………….. 76

V.I.3.2. Densities of states….. 79

V.I. 3.2.1. AlN compound 79

V.I.3.2.1. GaN compound 82

V.I.3.3. Electronic charge density.. 85

V.I.3.4. Ionicity factor.. 90

V.I.3.5. Observation of semiconducting aspect at rocksalt phase............ 92

V.I.4. Elastic Properties 95

V.I.4.1 Elastic constants.. 96

V.I.4.2. Internal-strain parameters 96

V.I.5. Piezoelectric properties.. 98

V.I.6. Bandgaps pressure coefficients.. 101

V.I.7. Deformation potential constants.. 105

V.I.8. Chemical trends in the pressure coefficient.................................... 106

V.I.9. Ionicity factor under pressure.. 107

V.I.10. Effect of pressure on elastic properties.. 110

V.I.11. Pressure effect of piezoelectric constants and transverse effective

Charges.. 113

V.I.12. Calculation of energy loss near edge structure.................................. 117

V. Part II: AlN and GaN doped with Mn 120

V.II.1. Computational details.. 120

V.II.2. Structural optimization.. 121

V.II.3. Electronic structures and magnetic properties 123

V.II.4. The exchange coupling.. 125

References.. 130

Conclusion.. 135

Nomenclature

Frequently used abbreviations:

AlN	Aluminium Nitride
GaN	Galmium Nitride
ZB	Zincblende structure
WZ	Wurtzite structure
RS	Rocksalt structure
DMS	Diluted magnetic semiconductors
DFT	Density functional theory
KS	Kohn-sham equation
xc	Exchange-correlation functional
R_{mt}	Muffin-tin radius
LDA	Local density approximation
GGA	Generalized gradient approximation
LSDA	Local spin density approximation
APW	Augmented plane wave
LAPW	Linearized augmented plane wave
APW+lo	Augmented plane wave plus local orbitals
FP-LAPW	Full-potential linearized augmented plane wave
FP-L/APW+lo	Full-potential linearized / augmented plane wave plus local orbitals
DOS	Density of states
ELNES	Energy loss near edge structure
m_B	Bohr magneton

List of Figures :

I.1. Equilibrium pressures of phase as function to the opposite of the temperature (s=solid, g=gaseous, l= nitrogen dissolved in Ga liquid) according to I. Grzegory [35] (1bar=0,1MPa).. 11

II.1. Concept of spin-electronics (spintronics). In semiconductor spin-electronics spin properties as well as electronic and optical properties are utilized at the same time.. 23

II.2. Computed values of the Curie temperature T_C for various p-type semiconductors containing 5% of Mn per cation (2.5% per atom) and 3.5×10^{20} holes per cm^3. (after [61,62]).. 26

III.1. One indicator of the increasing use of DFT is the number of records retrieved from the INSPEC databases by searching for the keywords ‘‘density,’’ ‘‘functional,’’ and ‘‘theory.’’ This is compared here with a similar search for keywords ‘‘Hartree’’ and ‘‘Fock,’’ which parallels the overall growth of the INSPEC databases for any given year, approximately 0.3% of the records have the Hartree–Fock keywords [6].. 33

III.2. Schematic representation of various DFT-based methods of calculation........ 39

III.3. Flow-chart for self-consistent density functional calculations....................... 41

IV.1. Adaptation of the basis set by dividing the unit cell into atomic spheres and interstitial regions... 47

V.I.1. Schematic illustration of (a) the zincblende and (b) the wurtzite structures....... 57

V.I.2. Total energy as a function of the volume for zincblende AlN and GaN with LDA and GGA calculations.. 59

V.I.3. Total energy as a function of the volume, c/a ratio and u for wurtzite AlN with (a) LDA and (b) GGA calculations.. 62

V.I.4. Total energy as a function of the volume, c/a ratio and u for wurtzite GaN with (a) LDA and (b) GGA calculations.. 64

V.I.5. Total energy as a function of the volume for rocksalt AlN and GaN with LDA and GGA calculation.. 68

V.I.6. Total energy as a function of the volume for zincblende, wurtzite and rocksalt AlN and GaN with LDA and GGA calculation.................................. 71

V.I.7. LDA and GGA Band structures of AlN along the principle high-symmetry directions in the brillouin zone in (a) zincblende and (b) wurtzite phases. The energy zero is taken at the valence band maximum………………………….. 74

V.I.8. LDA and GGA Band structures of GaN along the principle high-symmetry directions in the brillouin zone in (a) zincblende and (b) wurtzite phases, the Ga 3d treated as valence states. The energy zero is taken at the valence band maximum………………………………………………………………….... 77

V.I.9. Calculated total and partial density of states of AlN in (a) zincblende and (b) wurtzite structures……………………………………………………….……. 80

V.I.10. The angular-momentum decomposition of the atom-projected densities of states in (a) ZB-AlN and (b) WZ-AlN…………………………………………..…….. 81

V.I.11. Calculated total and partial density of states in (a) ZB-GaN and (b) WZ-GaN, when Ga 3d are treated as valence states……………………………….………….. 83

V.I.12. The angular-momentum decomposition of the atom-projected densities of states in (a) WZ-GaN and (b) ZB-GaN, when Ga treated as valence states…………… 84

V.I.13. Line plot of the calculated total valence charge densities along the Al-N bond direction for (a) ZB-AlN and (b) WZ-AlN……………………………….……... 86

V.I.14. Line plot of the calculated total valence charge densities along the Ga-N bond direction for (a) ZB-GaN and (b) WZ-GaN…………………………………….... 87

V.I.15. Contour plot of the total valence charge density in the (110) plane of AlN (a) zincblende and (b) wurtzite………………………………………………….... 88

V.I.16. Contour plot of the total valence charge density in the (110) plane of GaN (a) zincblende and (b) wurtzite………………………………………………….... 89

V.I.17. The Phillips ionicity as function of the Garcia and Cohen factor ionicity. The open circles represent our calculated values………………………………….. 92

V.I.18. LDA and GGA Band structure of rocksalt (a) AlN and (b) GaN along the principle high-symmetry directions in the brillouin zone. The energy zero is taken at the valence band maximum…………………………………….………. 93

V.I.19. Direct and indirect bandgap energies versus pressure in zincblende (a) AlN and (b) GaN…………………………………………………………………………... 102

V.I.20. Calculated dependence of the direct and indirect bandgaps in zincblende (a) AlN and (b) GaN on change lattice constant…………………………….……… 103

V.I.21. Line plot of calculated total valence charge densities along the (a) Al-N and (b) Ga-N bond direction under pressure………………………..…… 108

V.I.22. Calculated dependence of the ionicity factor as a function of pressure for zincblende (a) AlN and (b) GaN…………………………………..……………. 109

V.I.23. Calculated pressure dependence of C_{ij}, C_S, B and ζ for zincblende (b) AlN and (a) GaN………………………………………………………………..…… 112

V.I.24. Variation of the piezoelectric coefficient versus pressure of zincblende (a) AlN and (b) GaN…………………………………………………………..…………. 114

V.I.25. Transverse effective charge versus pressure for zincblende (a) AlN and (b) GaN………………………………………………………………………… 115

V.I.26. Theoretical Al-K and N-K ELNES of zincblende AlN. The spectra for the inequivalent atoms positions have been calculated separately and weighted in the present Figure………………………………………………….……………. 116

V.I.27. Theoretical Ga-$L_{2,3}$ and N-K ELNES of zincblende GaN. The spectra for the inequivalent atoms positions have been calculated separately and weighted in the present Figure …………………………………………………….………… 119

V.II.1. The variation of total energies with the total volume for nomagnertic (nm) and ferromagnetic (fm) states of GaN:Mn and AlN:Mn systems…………………… 122

V.II.2. Total and local partial densities of states in the ferromagnetic of (a) GaN:Mn and (b) AlN:Mn at 25% of Mn……………………………………….………………. 124

V.II.3. Partial densities of states of Mn impurity in the ferromagnetic of (a) GaN:Mn and (b) AlN:Mn at 25% of Mn. Peaks for majority and minority e_g and t_{2g} states are labelled……………………………………………………………….. 125

V.II.4. Spin polarized band structure of GaN:Mn system, (a) majority spin and (b) minority spin……………………………………………………………………….. 127

V.II.5. Spin polarized band structure of AlN:Mn system, (a) majority spin and (b) minority spin. ……………………………………………………………………… 128

List of Tables :

V.I.1. Lattice constants *a*, bulk modulus *B*, and pressure derivations of the bulk modulus B' of zincblende AlN…………………….………………………. 60

V.I.2. Lattice constants *a*, bulk modulus *B*, and pressure derivations of the bulk modulus B' of zincblende GaN. ………………………………………….…. 60

V.I.3. Lattice constants *a* and *c*, c/a, internal parameter u, bulk modulus B, and derivative B' of wurtzite AlN..…………………………………………….…….. 66

V.I.4. Lattice constants *a* and *c*, c/a, internal parameter u, bulk modulus B, and derivative B' of wurtzite GaN …………………………………………………….. 66

V.I.5. Lattice constants *a*, bulk modulus B, and pressure derivations of the bulk modulus B' of rocksalt AlN ……………………………………………………… 69

V.I.6. Lattice constants *a*, bulk modulus B, and pressure derivations of the bulk modulus B' of rocksalt GaN ………………………………………………………. 69

V.I.7. Transition pressures (p_t) for AlN and GaN.……………………………………. 72

V.I.8. Calculated bandgaps, antisymmetric gap (E_{asy}) upper-valance bandwidth (UVBW) and total valence bandwidth (TVBW) for wurtzite and zincblende structures of AlN compared to other theoretical calculations and experiments. All energies are in eV……………………………………………….………….. 75

V.I.9. Calculated bandgaps, antisymmetric gap (Easy) upper-valance bandwidth (UVBW) and total valence bandwidth (TVBW) for wurtzite and zincblende of GaN structures compared to other theoretical calculations and experiments. All energies are in eV…………………………………………………………………….. 78

V.I.10. Calculated ionicity factor *f*; of AlN and GaN in both zincblende and wurtzite structures. The differences in electronegativities, χ_N -$\chi_{Ga\ ou\ Al}$; are also listed for comparison …………………………………………………………………….….. 91

V.I.11. Calculated bandgaps of AlN and GaN in rocksalt structure to other theoretical calculations. All energies are in eV……………………………………………... 94

V.I.12. Elastic constants and internal-strain parameter and of zincblende AlN ……….. 97

V.I.13. Elastic constants and internal-strain parameter and of zincblende GaN ……..… 97

V.I.14. Polarity, piezoelectric charge, piezoelectric constants (in units of C/m^2) and transverse effective charge (in units of e) of zincblende AlN.……………..….. 100

V.I.15. Polarity, piezoelectric charge, piezoelectric constants (in units of C/m^2) and transverse effective charge (in units of e) of zincblende GaN.………………… 100

V.I.16. Piezoelectric constants (in C/m^2) and transverse effective charge (in e) of several zincblende compounds reported in Refs. [80-85]………………………. 100

V.I.17. Pressure coefficients related to $E_g(P)=E(a_0)+\alpha P + \beta P^2$ of the calculated values of the energy gaps for zincblende AlN and Compared with other calculations…………………………………………………………………... 104

V.I.18. Pressure coefficients related to $E_g(P)=E(a_0)+\alpha P + \beta P^2$ of the calculated values of the energy gaps for zincblende GaN and Compared with other calculations..…………………………………………………………………….. 104

V.I.19. Coefficients obtained from least-squares fits to $E_g(a)=E(a_0) +\gamma (\Delta a/a_0) + \delta (\Delta a/a_0)^2$ of zincblende AlN, where a is the lattice constant (a_0 is the equilibrium value).………………………………………………………………………… 104

V.I.20. Coefficients obtained from least-squares fits to $E_g(a)=E(a_0)+\gamma (\Delta a/a_0) + \delta (\Delta a/a_0)^2$ of zincblende GaN, where a is the lattice constant (a_0 is the equilibrium value) ……………………………………………….……………... 105

V.I.21. Bandgap deformation potential constants for zincblende AlN and GaN……….. 106

V.I.22. *Calculated pressure coefficients related to* $f_i(P)=f_i(P=0)+ \lambda P + \mu P^2$ *of the ionicity factor for zincblende AlN and GaN*... 110

V.I.23. Calculated pressure derivatives of the elastic modulus and internal-strain parameter for zincblende AlN and GaN.………………………………………... 113

V.I.24. Pressure coefficients of the polarity, piezoelectric charge, piezoelectric constants (in C/m^2) and transverse effective charge (in e) for zincblende AlN… 116

V.I.25. Pressure coefficients of the polarity, piezoelectric charge, piezoelectric constants (in C/m^2) and transverse effective charge (in e) for zincblende GaN... 116

V.I.26 Positions of the peaks I-IV Figures VI.I.25 and VI.I.26 values are in units of eV. The experiment values are compiled in ref. [103]………………………….. 117

V.II.1 Lattice constants a, bulk modulus B, and its pressure derivative B' and energy difference between fm and nm magnetic states ΔE_{fm-nm} of GaN:Mn and AlN:Mn at 25%………………………………………………………………. 121

V.II.2 Magnetic moments in AlN:Mn and GaN:Mn systems with a 25%……………... 123

V.II.3 Conduction ΔE^c and valence ΔE^v band-edge spin-splitting, and exchange constants for AlN:Mn and GaN:Mn…………………………………………….. 129

Introduction

It is not astonishing that the Nobel Prize Committee decided to single out in 2000 milestone concepts of *Zores I. Alferov*, *Jack S. Kilby*, and *Herbert Kroemer*. Actually, the outcome of the laureate ideas is surpassing the speculations of *Richard Feynman* about manipulating and controlling things on a small scale[1], regarded as totally unrealistic in time of his visionary speech 40 years ago. Kilby was among those who put forward the notion of integrated circuits. By now, semiconductor processors and memories, despite containing several hundreds of millions of submicron elements, are both cheap and redundant.

Semiconductor materials constitute today basic building blocks of emitters and receivers in cellular, satellite, and fibreglass communication. Among them, the III-nitrides which are nowadays widely used by the industry. With respect to ”classical” III-V semiconductors, the group-III nitrides semiconductors have attracted much attention in recent years to their great potential for technological applications. AlN and GaN are regarded as promising wide bandgaps semiconductors, ranging from the ultraviolet (UV) to the visible regions of the spectrum. They have a high melting point, a high thermal conductivity, and a large bulk modulus. These properties, as well as the wide band gaps are closely related to strong (ionic and covalent) bonding. These materials can therefore be used for short-wavelength light-emitting diodes (LEDs) laser diodes and optical detectors as well as for high-temperature, high-power and high-frequency electronic devices. Bright and highly efficient blue and green LEDs are already commercially available and diode lasers have been reported, emitting in the blue-violet range initially under pulsed conditions and subsequently under continuous operation[2].

When the nitrides are doped with magnetic elements they give birth to Dilute magnetic semiconductors (DMS’s) which have attracted considerable attention, because they hold the promise of using electron *spin*, in addition to its *charge*, for creating a new class of ‘‘spintronic’’ semiconductor devices with unprecedented functionality. It has been intensively studied in order to fabricate a new functional semiconductor taking advantage of the spin degree of freedom in DMS’s.

[1] R.P. Feynman, in: Miniturization, ed H.D. Gilbert (Reynhold, New York, 1960) p. 282

[2] S. Nakamura and G. Fasol, *The Blue Laser Diode* (Berlin: Springer, 1997).

The suggested applications include, e.g., ‘‘spin field effect transistors,’’[3] which could allow for software reprogramming of the microprocessor hardware during run time, semiconductor-based ‘‘spin valves,’’ which would result in high-density nonvolatile semiconductor memory chips, and even ‘‘spin qubits,’’ to be used as the basic building block for quantum computing[4]

Owing to the development of the computational power of recent computers and the progress in the calculation method for the electronic structure, it has become to calculate the electronic structure of a crystal with high precision from first principles without any empirical parameters. Today, it is possible not only to explain the already known properties of a given material but also to predict what property will be expected for a hypothetical material.

Given the complexity of the synthesis/characterization procedure, computer-modeling investigation has here been used to determine and to predict their material properties. The computational methods have already been applied to many, with great success, provoking a considerable interest in investigating other materials for example AlN and GaN and doped with Mn.

From crystallography point of view and under ambient conditions AlN and GaN crystallize in the hexagonal wurtzite structure. Recent epitaxy of thin GaN films has been demonstrated to result in the cubic zincblende structure (3C). The remarkable progress in the synthesis of such 3C-GaN films is related to the plasma-assisted molecular beam epitaxy on GaAs (001) or 3C-SiC (001) substrates. Due to the reactivity of AlN, high-purity source material and an oxygen-free environment are required to grow AlN crystals of good quality. Some problem may arise during the growth process of nitrides layers on crystalline substrates like e.g. SiC, Si or GaAs. This is related to the large lattice mismatch and the difference in the thermal expansion coefficients between epitaxial layer and substrate, which can cause large stresses in the epitaxial layers.

[3] G. Prinz, Science, 282, 1660 (1998);
[4] G. Burkard et al, Phys. Rev. B 59, 2070 (1999).

In order to help understand and control the material and device properties, we report in this thesis numerical investigations based on a first-principles study of ground states properties and comparison between GGA and LDA calculations of the both zincblende and wurtzite AlN and GaN and under high pressure. Electronic properties such as band structures, density of states and charge density are detailed for GGA and LDA calculations of the both zincblende and wurtzite AlN and GaN. In addition, the influence of hybridization on the chemical bonding and stability has been discussed in terms of the site projected densities of states as well as the crystal orbital overlap population. Thus, we study the elastic properties, as well as their behavior when a hydrostatic pressure is applied. Principal features of the calculated band structures such as energy bandgaps and ionic character are examined when we apply a hydrostatic stress. Moreover, we determine the piezoelectric constants and transverse effective charges and their behavior under pressure. Finally, we study the structural optimization, electronic structures and magnetic properties of the AlN and GaN-based diluted magnetic semiconductors. The results show the half-metallic ferromagnetism for the AlN:Mn and GaN:Mn.

The present thesis is divided into five chapters. In Chapters 1 and 2, we give a general introduction to the domain of the III-nitride semiconductors and diluted magnetic semiconductors and their technological applications. In particular, Chapter 3 resumes the basic ideas behind the DFT, while Chapter 4 contains a brief description of the method of calculations. Chapter 5 is divided into two parts. In part I, we report the numerical investigations of the structural, elastic and electronic properties under hydrostatic pressure. The study of pressure effect consolidates and leads us to achieve the essential goal of this part. In part II, we report an analysis of the magnetic and electronic properties of the AlN and GaN doped with Mn. Finally a general conclusion is presented for each of the investigated class of systems.

Chapter I

Group III-Nitride Semiconductors
- AlN and GaN -

Abstract :

We attempt in this chapter to draw the motivation and aims of our study. This chapter begins with an introduction to the current interest of the III-nitride semiconductors. In the next section, we will present the some basic physical properties and thermodynamic stability of these materials. The last section is devoted to the presentation of the different technological applications of AlN and GaN.

I. 1. Current interest

Wide band gap semiconductor materials extend the field of semiconductor applications to the limits where classical semiconductors such as Si and GaAs fail [1-7]. They can emit light at shorter wavelengths (blue and ultraviolet). In addition, AlN and GaN have a high melting point, a high thermal conductivity, a large bulk modulus [8-10] and chemical inertness. These properties, as well as the large bandgaps, are closely related to their strong (ionic and covalent) bonding.

There have been few periods of semiconductor materials research more stimulating and satisfying than that currently experienced by the rapidly growing of III-V researchers who have taken up the study of group III nitrides. Not only have some formidable materials problems been overcome in a remarkably short time, but also commercially viable applications are immediately clear for all to see. Much progress is yet to be made in developing these materials.

The excitement generated by these recent developments, which is well illustrated by the number of review articles already written [1,3,4,11-20] stems from the fact that the nitride semiconductors AlN and GaN are indirect and direct band gap materials, what is more, they form a complete serie of ternary alloys which spans the whole of the visible spectrum and extends well into the ultraviolet (UV) region, i.e. continuously variable from 650 to 200 nm, for those readers who think more readily in wavelength terms. This makes them ideal candidates for carefully tailored optoelectronic devices operating anywhere within this wavelength range, but more specifically, for visible light emitters in the previously difficult blue and green parts of the spectrum.

Two important applications have been apparent some time, for example, those of short wavelength laser diodes (LDs) for optical disk readout and high-efficiency light-emitting diodes (LEDs) for full colour display. Red LEDs with efficiencies greater than 10% have been commercially available for some years (see, for example, Smith [21]) but the efficiencies of green and, particularly, blue diodes fell a long way short of this, seriously restricting the possibilities for LED display panels.

While attempts to improve the efficiency of blue devices using II-VI compounds have been partially successful (see, for example, Gunshor et al [22]), the problem of achieving acceptably long operating lifetimes has yet to be solved, leaving the field open to the III-V alternative. Much of the current euphoria depends on the recent commercial development of both green and blue InGaN LEDs with efficiencies in the 5–10% range by The Nichia Chemical Company in Japan [8,23,24,25]. This led rapidly to the development of large outdoor full color displays [26] and opens up many other display possibilities, which are yet to emerge. In addition, it has stimulated work towards the long-sought blue LD, which now shows considerable promise. Several reports have appeared which describe room-temperature-pulsed operation of short wavelength LD's based on the same materials system [15,27-31].

I. 2. III-Nitride physical properties

I. 2. 1. Some basic material properties

Concerning the physical and electronic properties of the nitrides, we present the several obvious differences between the nitrides and the better known III-V compound semiconductors, which can be related to two basic properties of the N atom, its size and the nature of the chemical bond between it and the relevant group III atom.

The small covalent radius of N (0.7 Å, compared with 1.10 for P, 1.18 for As, 1.36 for Sb) [32] results in significantly reduced lattice parameters for the nitrides, (4.37 Å for AlN and 4.50 Å for GaN) [32], compared with other III-V compounds (5.4505 Å for GaP, 5.653 Å for GaAs and 6.095 Å for GaSb) [32], and the large bond energies (2.28 eV for AlN, 2.2 eV for GaN) [33] imply high melting temperatures. Both are critical in relation to the growth of bulk crystals and to epitaxy. First, the relatively small size of N compared with the group III atoms appears to play a role in determining the crystal structure, the thermodynamically stable structure for these materials (AlN and GaN) being the hexagonal wurtzite (WZ) structure [13] which corresponds to that of several of the well known II–VI compounds, i.e. CdS, ZnS and CdSe. We should point out that the cubic zincblende (ZB) structures do exist and GaN, in particular, has been studied in some depth [13], nevertheless by far the majority of work reported so far concerns the hexagonal form.

High melting temperatures make for serious difficulty in the growth from the melt and the only bulk crystals so far available are relatively small GaN crystals grown from gallium solution, which again requires high temperatures combined with high nitrogen pressures [34,35]. Such crystals take the form of hexagonal platelets with the hexagonal c-axis normal to the plane of the plate. This is convenient for epitaxial growth but they are not yet widely available. The lack of a ready supply of bulk substrate material has resulted in epitaxial growth being performed largely on foreign substrates, with all the problems associated with this form of deposition. What is more, the small lattice parameters make for large mismatch with any of the well-established group IV or III-V semiconductor crystals and have led to the use of sapphire substrates by the majority of workers. However, this, also, implies a large lattice mismatch and significant differences in the thermal expansion coefficient, both of which cause serious problems in achieving adequate crystal quality in the deposited films. The fact that it is an electrical insulator can also be a disadvantage in certain applications. SiC has been used by some workers because of its much closer lattice match and the fact that it can be doped both n and p-type but it is relatively expensive for routine applications. Two other consequences of the high bond energies are noteworthy. It is good to recognize that high-quality epitaxy requires good surface mobility for the group III atom and this, also, implies a choice of growth temperature somewhat higher than usual for other III-V compounds. On the other hand, it seems clear that GaN, at least, is an unusually stable compound, which probably has some bearing on its apparent immunity to the deleterious effects of extended defects.

The reduced symmetry of the WZ structure (compared with the ZB structure of the majority of III-V compounds) has immediate consequences for the band structure (in particular for the valence band structure) of the nitrides. In the ZB compounds the valence band maximum at the Γ point in the Brillouin zone is doubly degenerate, the so-called heavy and light hole bands being coincident at $k = 0$, while the 'split-off' band is typically a few tenths of an electron volt lower in energy.

As it is well known from studies of quantum well (QW) structures, in the presence of an axial component of crystal field the degeneracy at the zone centre is lifted, yielding three separate valence bands whose relative energies are determined by a combination of spin–orbit coupling and the strength of the axial crystal field. This, then, is the situation found for WZ semiconductors even in the absence of any artificially imposed structural perturbation (see, for example, Dimmock [36]).

I. 2. 2. Common Crystal Structures

There are three common crystal structures shared by the group III-V nitrides : the wurtzite, zincblende, and rocksalt structures. At ambient conditions, the thermodynamically stable structures are wurtzite for bulk AlN and GaN [37-39]. The zincblende structure for GaN has been stabilized by epitaxial growth of thin films on the (001) crystal planes of cubic substrates such as Si, 3C-SiC, MgO, and GaAs [40-46]. The remarkable progress in the synthesis of such cubic AlN layers is related to the plasma-assisted molecular beam epitaxy [43]. In these cases, the innate tendency to form the wurtzite polytypes is overcome by topological compatibility. The rocksalt structure can be induced in AlN and GaN at very high pressures. The wurtzite polytype has a hexagonal unit cell and thus two lattice constants, c and a. It contains 6 atoms of each type. The space group for the wurtzite structure is $P6_3mc$ (C_{6v}^4). The wurtzite structure consists of two interpenetrating hexagonal close-packed (HCP) sublattices, each of which is with one type of atoms, offset along the c axis by 5/8 of the cell height (5/8 c).

The zincblende structure has a cubic unit cell, containing four group III and four nitrogen elements. The space group for the zincblende structure is F-43m (T_d^2). The position of the atoms within the unit cell is identical to the diamond crystal structure in that both structures consist of two interpenetrating face-centered cubic sublattices, offset by one quarter of the distance along a body diagonal. Each atom in the structure may be viewed as situated at the center of a tetrahedron, with its four nearest neighbors defining the four corners of the tetrahedron.

The zincblende and wurtzite structures are similar. In both cases, each group III atom is coordinated by four nitrogen atoms. Conversely, each nitrogen atom is coordinated by four group III atoms. The main difference between these two structures is in the stacking sequence of the closest packed diatomic planes. For the wurtzite structure, the stacking sequence of (0001) planes is ABABAB in the <0001> direction. For the zincblende structure, the stacking sequence of (111) planes is ABCABC in the <111> direction.

I. 2. 3. Phase Diagram

The data on phase diagrams of GaN and AlN are limited and contradictory by reason of high melting temperatures (T_M) and high nitrogen dissociation pressures (P_{N2}^{dis}). Dissociation Pressure of MN, where M stays for Al and Ga is defined as nitrogen pressure at the thermal equilibrium of the reaction [18]: MN(s) =M(l) + (1/2)N2(g), where s, l and g stay for solid, liquid and gas. Reported values for P_{N2}^{dis} for GaN (see Figure I.1) show large discrepancies. Sasaki and Matsuoka [47] concluded that the data of Madar et al. [48] and Karpinski et al. [49] are the most reliable. According to Figure I.1 the nitrogen dissociation pressure equals 1 atm. at approximately 850 °C, and 10 atm. at 930 °C. At 1250 °C the GaN decomposed even under pressure of 10.000 bar of N_2. It should therefore come as no surprise that; the incorporation of nitrogen is not a trivial problem at high temperatures. For the pressures below equilibrium at given temperatures, the thermal dissociation occurs at a slow and apparently constant rate suggesting a diffusion controlled process of dissociation.

Due to the above mentioned N dissociation, the data on the melting points are contradictory. Landolt and Börnstein [50] give T_M of AlN equal to 2400 °C at a pressure of 30 bar, and T_M of GaN >1700 °C at a pressure of 2000 bar. Thus, the nitrogen dissociation pressure of AlN is orders of magnitude smaller than that of GaN. Massalski [51] cites T_M of AlN equal to 2800 °C. There are reports estimating T_M of AlN at 2200 °C [52] and 2450 °C [53]. Van Vechten [54] determined theoretically the T_M of AlN to be 3487 K. Porowski and Grzegory [34] estimate T_M of AlN to be larger than 3000 K at a dissociation pressure of a few hundred bar, and T_M of GaN larger than 2500 K at tens of kbar. Moon and Hwang [55] and

Goumri-Said et al [56] determined theoretically the T_M of GaN and AlN in zincblende phase to be 2302 K and 2387 K respectively.

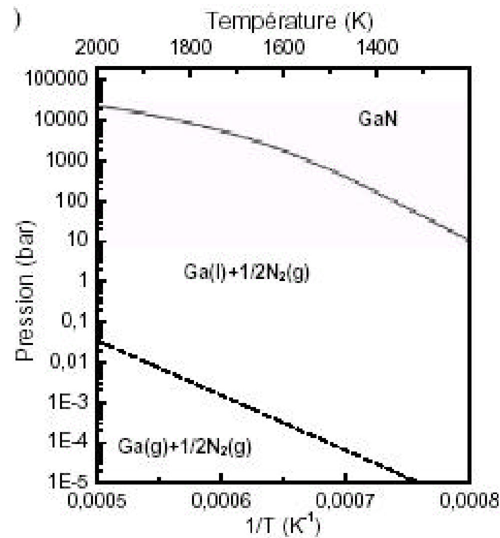

Figure I. 1. Equilibrium pressures of phase as function to the opposite of the temperature (s=solid, g=gaseous, l= nitrogen dissolved in Ga liquid) according to I. Grzegory [35] (1bar=0,1MPa)

I. 3. Technological applications :

I. 3. 1. Light-emitting diodes (LEDs) :

The LEDs present an important market, with for applications the signaling, the display with color screens, or again sources of white light with especially the public lighting [57,58].

The red LEDs based on GaAlAs alloy have been commercialized for a long time already, with a luminous efficiency of 20-30 $m.W^{-1}$ and a high brilliance of 2Cd. since a certain time, the green LEDs based on AlInGaP alloy are also produced but they are green-yellowish (564nm) instead of green pure, and possess a weak efficiency external quantum (0,6%) and a weak intensity (0,1Cd). These materials being equally useful for the signaling.

The white LEDs are based either on the association of three LEDs (red, green, blue) or on the association of a blue LED or UV and a material that, excited, emits lower energy photons, the combination giving then the white light. The realization of LEDs to basis of GaN has become a contest since the beginning of years 1990, period to which their realization has been able to be envisaged thanks to a certain improvement of the crystalline film quality epitaxy of GaN. Some LEDS have been conceived and are currently commercialized.

I. 3. 2. Laser diodes (LDs)

The market of the laser diodes [Laser Diodes (LDs)] is for half attributed to communications and for half to the impression and to the storage of the information. Concerning communications, used optical fibers being transparent between 1,3 and 1,55µm. The used LDs are manufactured from GaAs and InP. However, an emission to 1,55µm has been put in obviousness for InGaAsN on GaAs [57].

Concerning the impression and the storage of the information, the market is for the moment dominated by red LDs to 780nm for CD and to 635 or 650nm for DVD. Very compact LDS emitting at shot wave length (400-600nm) and medium (5mW) or high (35 - 50mW) power are required to enhance performances. Indeed, a diminution of the length of wave allows a best focusing of the spotlight of a beam, the surface of the spotlight being proportional to the square of the length of wave. The quality of the impression and the density of storage on optical disks will be therefore considerably improved by the utilization of blue or violet LDs. Thus, the capacity of storage of a DVD would pass from 2,9Gbyte to 30Gbyte by decreasing the length of wave from 635-650nm to 410nm. Furthermore, the perusal asks only a power of 5mW while the handwriting (engraving) necessitates a power of 35-50mW [57].

The Blue LDs currently produced are LDs DBR infrared high power associated with materials nonlinear as LiNbO3 capable to generate a beam at 425nm (violet-blue). The former are powerful enough (15mW), with less noise effects and have a coherent beam. They are however very expensive, not compact and necessitate a precise mechanical alignment. The LDs based on InGaN are therefore promised to a great future for less expensive and simpler devices [57].

I. 3. 3. UV detectors

The sun produces a great quantity of UV, whose a great part is absorbed by the ozone and gas layer of the atmosphere. Alone radiation whose wave length is large than 280nm get on earth. Detectors of UV radiation produced on earth, told "solar blind", have to detect radiations between 265nm and 280nm, zone presenting the less parasitic radiation. UV detection possesses military or civil applications as the personal dosimeters for UV rich environments, detection of fires, and identification of missiles by their trail, or the guidance of missiles [59].

The photo-detectors currently available are based on thin film of diamond (Eg =5,4eV - 230nm), or of SiC (E_g=2,9eV - 430nm). However, they necessitate the usage of filters and do not present a good UV/visible selectivity. The nitrides of elements of column III present a strong interest for optical detection because the gap of alloy AlInGaN can vary between 1,9eV (650nm) and 6,2eV (200nm). Especially, the UV detection can be realized with the help of AlGaN alloy, GaN having an absorption at 365nm and AlN at 200nm. Moreover the III-V nitrides are stable in severe physical and chemical environment [60].

[1] S. N. Mohammad, A. Salvador, and H. Morkoç, Proc. IEEE, **83**, 1306 (1995).

[2] H. Morkoç, in Proceeding of International Symposium on Blue Lasers and Light Emitting Diodes, Chiba Univ., Japan, March 5-7, 1996, p. 23-29.

[3] H. Morkoç, S. Strite, G. B. Gao, M. E. Lin, B. Sverdlov, and M. Burns, J. Appl. Phys. **76**, 1363 (1994).

[4] S. Strite and H. Morkoç, GaN, AlN, and InN: A Review, J. Vac. Sci. and Technol. B. **10**, 1237 (1992).

[5] J. F. Schetzina, International Symposium on blue Lasers and Light Emitting Diodes, Chiba Univ., Japan, March 5-7, 1996, p. 74-79.

[6] I. Akasaki and H. Amano, International Symposium on blue Lasers and Light Emitting Diodes, Chiba Univ., Japan, March 5-7, p. 11-16, (1996).

[7] M.E. Lin, S. Strite and H. Morkoç, "*The Physical Properties of AlN, GaN and InN*," *in The Encyclopedia of Advanced Materials*, Eds. D. Bloor, M. C. Fleming, R. J. Brook, S. Mahajan, Senior Ed. R. W. Cahn, pp. 79-86, Pergamon Press, (1994).

[8] S. Nakamura, T. Mukai, and M. Senoh, Appl. Phys. Lett. **64**,1687 (1994).

[9] S. Nakamura, T. Mukai, and M. Senoh, Jpn. J. Appl. Phys. **30**, 1998 (1991).

[10] S. Nakamura, M. Senoh, S. Magahama, N. Iwasa, T. Yamada, T. Matsushita, H. Kiyoku, and Y. Sugimoto, Jpn. J. Appl. Phys. **L74** , 1998 (1996).

[11] R.F. Davis, Physica B **185,** 1 (1993).

[12] R.F. Davis, M.J. Paisley, Z. Sitar, D.J. Kesler, K.S. Ailey and C. Wang, Microelectron. J. **25** 1 (1994).

[13] J.H. Edgar, *Properties of Group III Nitrides (ed. EMIS Datareviews Series 11)* (London: INSPEC, IEE, 1994).

[14] S.N. Mohammad and H. Morkoc, *Progress in Quantum Electronics* ed M. Osinski (London: Elsevier 1995)

[15] I. Akasaki, S. Sota, H. Sakai, T. Tanaka, M. Koike and H. Amano, Electron. Lett. **32,** 1105 (1996).

[16] D.A. Neumayer and J.G. Ekerdt, Chem. Mater. **8**, 9 (1996).

[17] F.A. Ponce and D.P. Bour, Nature **386,** 351 (1997).

[18] S. Nakamura and G. Fasol, *The Blue Laser Diode* (Berlin: Springer, 1997).

[19] J.W. Orton and C.T. Foxon, A Review, Rep. Prog. Phys. **61,** 1 (1998)

[20] A. Trampert, O. Brandt and K.H. ploog, in *Crystal Structure of Group III Nitrides*, edited by J.I. Pankove and T.D. Moustakas, Semiconductors and Semimetals Vol. 50 (Academic, San Diogo 1998).

[21] S. D. Smith, *Optoelectronic Devices* (London: Prentice-Hall, 1995) p 92

[22] R. Gunshore, A. Nurmikko and M. Kobayashi, Physics World March 47 (1992).

[23] S. Nakamura, M. Senoh, N. Iwasa and S. Nagahama, Appl. Phys. Lett. **67,** 1868 (1995).

[24] S. Nakamura, M. Senoh, N. Iwasa and S. Nagahama, *Japan.* J. Appl. Phys. **34,** L797 (1995).

[25] S. Nakamura, M. Senoh, N. Iwasa , S. Magahama, T. Yamada and T. Mukai, Japan. J. Appl. Phys. **34,** L1332 (1995).

[26] R.A. Metzger, Compound Semicond. **1,** 26 (1995).

[27] S. Nakamura, M. Senoh, S. Magahama, N. Iwasa, T. Yamada, T. Matsushita, H. Kiyoku, and Y. Sugimoto, Jpn. J. Appl. Phys. **35,** L74 (1996).

[28] S. Nakamura, M. Senoh, S. Magahama, N. Iwasa, T. Yamada, T. Matsushita, H. Kiyoku, and Y. Sugimoto, Jpn. J. Appl. Phys. **35,** L217 (1996).

[29] S. Nakamura, M. Senoh, S. Magahama, N. Iwasa, T. Yamada, T. Matsushita, H. Kiyoku, and Y. Sugimoto, Appl. Phys. Lett. **68,** 2105 (1996).

[30] S. Nakamura, M. Senoh, S. Magahama, N. Iwasa, T. Yamada, T. Matsushita, H. Kiyoku, and Y. Sugimoto, Appl. Phys. Lett. **68,** 3269 (1996).

[31] S. Nakamura, M. Senoh, S. Magahama, N. Iwasa, T. Yamada, T. Matsushita, H. Kiyoku, and Y. Sugimoto, Appl.Phys. Lett. **69,** 1568 (1996).

[32] O. Madelung, *Physics of III–V Compounds* (New York: Wiley, 1964) p 18.

[33] S. Porowski and I. Grzegory, in Group III nitrides, edit. J. H. Edgar, INSPEC, London UK, 1994, pp. 71-88.

[34] S. Porowski, J. Jun, M. Bockowski, M. Leszezynski, S.T. Krukowski, M. Wroblewski, B. Lucznik and I. Grzegory *Proc. 8th Conf. on Semi -Insulating III–V Materials (Warsaw)* ed M Godlewski (Singapore: World Scientific, 1994).

[35] I. Grzegory, J. Jun, M. Bockowski, S.T. Krukowski, M. Wroblewski, B. Lucznik and S. Porowski J. Phys. Chem. Solids **56,** 639 (1995).

[36] J.O. Dimmock, *II–VI Semiconducting Compounds,* ed D.G. Thomas (New York: Benjamin, 1967) p. 277.

[37] W. J. Meng, in Group III nitrides, edit. J. H. Edgar, INSPEC, London UK, pp. 22-29. (1994).

[38] I. Akasaki and H. Amano, in Group III nitrides, edit. J. H. Edgar, INSPEC, London UK, pp.30-34. (1994).

[39] T. L. Tansley, *in Group III nitrides*, edit. J. H. Edgar, INSPEC, London UK, 1994, pp.35-42.

[40] O. Brandt, H. Yang, B. Jenichen, Y. Suzuki, L. Daï weritz, and K.H. Ploog, Phys. Rev. B **52**, R2253 (1995).

[41] D. Schikora, M. Hankeln, D.J. As, K. Lischka, T. Litz, A. Waag, T. Buhrow, and F. Henneberger, Phys. Rev. B **54**, R8381 (1996).

[42] M.J. Paisley, Z. Sitar, J.B. Posthill, and R.F. Davis, J. Vac. Sci. Technol. **A7**, 701 (1989).

[43] H. Okumura, H. Hamaguchi, T. Koizumi, K. Balakrishnan, Y. Ishida, M. Arita, S. Chichibu, H. Nakanish, T. Nagatomo and S. Yoshida, J. Cryst. Growth **189/190,** 390 (1998).

[44] T. Chassagne, G. Ferro, D. Chaussande, F. Cauwet, Y. Monteil, and J. Bouix, Thin Solid Films **402**, 83 (2002).

[45] E. Martinez-Guerrero, E. Bellet-Almaric, L. Martinet, G. Feuillet, B. Daudin, H. Mariette, P. Holliger, C. Dubois, C. Bru-Chevallier, T. Chassagne, G. Ferro, and Y. Monteil, J. Appl. Phys. **91**, 4983 (2002).

[46] Z.H. Feng, H. Yang, X.H. Zheng, Y. Fu, Y.P. Sun, X.M. Shen, Y.T. Wang, Appl. Phys. Lett. **82**, 206 (2003).

[47] T. Sasaki and T. Matsuoka, Analysis of two-step-growth conditions for GaN on AlN buffer layer, J. Appl. Phys. **77**, 192 (1995).

[48] R. Madar, G. Jacob, J. Hallais, and F. Fruchart, High Pressure Solution Growth of GaN, J. Cryst. Growth, **31**, 197 (1975).

[49] J. Karpinski, J. Jun, and S. Porowski, J. Crystal Growth, **66**, 1 (1984)

[50] Landolt and Börnstein, Numerical Data and Fundamental Relationships in Science and Technology, v. 17, Semiconductors, (Springer, Berlin, 1984).

[51] T.B. Massalski, Binary Alloys, Phase Diagrams, Second Edition (ASM International, USA, 1990) p. 176.

[52] J.D. latwa, Metal. Progr. **82**, 139 (1962).

[53] E. Wayne, Ceramics, **15**, 48 (1964).

[54] J. A. Van Vechten, Phys. Rev. **B 7**, 1479 (1973).

[55] W. H. Moon and H. J. Hwang, Phys. Lett. A **315**, 319 (2003).

[56] S. Goumri-Said, M.B. Kanoun, A.E. Merad, G. Merad and H. Aourag, Chemical Physics 302, 135 (2004).

[57] J. Y. Duboz, *C. R. Acad. Sci. Paris, t. 1, Série IV*, 2000, p71–80.

[58] S. Nakamura, *Group III nitride semiconductor compounds – physics and applications*, (B. Gil, Publication Oxford Science, 1998), p391-416.

[59] E. Munoz, E. Monroy, J.L. Pau, F. Calle, F. Ommès and P. Gibart, *J. Phys. Condens. Matter*, **13**, 7115-7137 (2001).

[60] G.M. Smith, *Properties, processing and applications of gallium nitride and related semiconductors*, 1998, J. Edger, S. Strite, I. Akasaki, H Amano and C. Wetzel, Publication INSPEC, Datareview series n°23, p634-639.

Chapter II

Diluted Magnetic Semiconductors

- DMS -

Abstract :

In this chapter, we are going to present the position and the interest of a new branch of the electronic fields namely spin-electronics. Furthermore we give a historical overview on the advent of magnetic semiconductors and their interest for application in the technological area. Finally, we present the motivation of our choice of materials and their novelty as compared to other.

II. 1. Spintronics

Spin electronics (spintronics) is a young interdisciplinary field of nanoscience. Its rapid development, like that of competing new branches of electronics – molecular electronics, bioelectronics, and electronics of polymers, …etc, has its roots in the conviction that the progress that is being achieved by miniaturization of active elements (transistors and memory cells) cannot continue forever. Therefore, the invention of future information technologies must involve new ideas concerning the design of both devices and system architecture.

The main goal of spintronics is to gain knowledge on spin-dependent phenomena, and to exploit them for new functionalities. Hopes associated with spintronics stem from the well known fact that the magnetic fields present in the ambient world are significantly weaker than the electric fields. For this reason magnetic memories are non-volatile, while memories based on the accumulated electric charge (Dynamic Random Access Memory - DRAM) require a frequent refreshing. At present, one can already specify a set of problems to be solved by spin electronics. One of them is a construction of efficient microsensors of the magnetic field, which would replace devices employing magnetic coils. It is obvious that the increase in spatial resolution requires a reduction in size of the sensor. In the case of the coil, however, this is accompanied by a decrease in the sensitivity. Intensive research and development work carried out over last fifteen years or so, resulted in the developing of the appropriate device. The new generation sensors are exploiting a giant magnetoresistance effect (GMR) of multiple layer structures made of alternating ferromagnetic, antiferromagnetic, and paramagnetic metals [1,2]. The GMR results from the increase of electrical conductivity in the presence of the magnetic field that aligns the direction of magnetization vectors in neighboring layers. In contrast to the traditional sensors containing the Hall probe, the operation of the GMR sensor depends on the electron spin, and not on the charge, *i.e.,* the Lorenz force.

The most recent research on the field sensors focuses on spin-dependent electron tunneling between ferromagnetic layers through an isolator, typically thin aluminum oxide. It is expected that the tunneling effect will lead to a significant increase of magnetoresistance [3-5]. A side issue concerns the phenomenon of the Coulomb blockade that plays an important role whenever a tunnel junction becomes small [5]. One can expect that the parameters of tunneling magnetoresistance (TMR) sensors will make them suitable not just for reading

devices, but also as position detectors, for instance, in electric and gasoline engines, where Hall-effect sensors dominate today [6].

A much more ambitious spintronic objective is to develop magnetic random access memories (MRAM). These devices would combine the advantages of magnetic memories and those of DRAM. For this purpose, it is necessary to find means of writing and reading the direction of magnetization in given cells without employing any moving parts. An important step would be the elaboration of methods of controlling magnetization isothermally – by light or electric field, like in semiconductor DRAM, in which information writing proceeds *via* voltage biasing of the addressed transistor. In the magnetic memories presently available, the magnetization switching requires rather large power, as it is triggered either by the magnetic field generated by electric currents or by the laser heating above the Curie temperature. Obviously, research in this direction combines materials science, nanotechnology, and strongly correlated systems.

Elaboration of "intelligent" methods enabling magnetization control would also make it possible to fabricate spin transistors [7,8]. This device consists on two ferromagnetic metals separated by a nonmagnetic conductor. Simple considerations demonstrate that if spin polarized carriers injected to the nonmagnetic layer conserve spin orientation, the device resistance will depend on the relative directions of magnetization in the two ferromagnetic layers. Since the switching process does not involve any change in the carrier density, this transistor will be characterized by a favorable value of the product of electric power consumption and switching time, provided that the spin injection would be efficient and no mechanisms of spin relaxation would operate.

Perhaps the most important challenge for spintronics is the development of quantum computation and communication [9]. Particular importance of spin degree of freedom in this context originates from the fact that it can preserve phase coherence for a much longer time than the orbital degrees of freedom. Thus, the electron spin is much more promising than the electron charge for materialization of the present revolutionary ideas on quantum computing, quantum cryptography, data compression and teleportation [9]. Thus, spin quantum devices, such as quantum dots [10,11], may change not only the principles of devices operation, but also the basis of the halfcentury-old computer architecture. Some researchers suggest that the

best candidate to carry quantum information would be nuclear spins of ^{31}P in isotopically pure ^{28}Si, where the spin coherence time reaches several hours [12].

However, it has also been shown experimentally that the spin polarization lifetime in doped semiconductors may be several orders of magnitude longer than the time of momentum relaxation [13]. One has to mention, although, that up to now the research on quantum computation is theoretical. Any experimental achievement, independently of the material used and the experimental method applied will be regarded as a significant breakthrough.

II. 2. Diluted magnetic semiconductors

Modern information technology utilizes the charge degree of freedom of electrons in semiconductors to process the information and the spin degree of freedom in magnetic materials to store the information. Magnetoelectronics is a new fastly developing field, where the two degrees of freedom, the charge and the spin of the carriers, are utilized simultaneously to create new functionalities. In more general terms, this new field is referred to as spin-electronics or spintronics to include those spin-utilizing devices that need neither the magnetic field nor magnetic materials. The magnetoresistance (MR) sensors made of multilayers containing metal ferromagnets, showing giant magnetoresistance (GMR) or tunneling magnetoresistance (TMR), are today's best known successful magnetoelectronics devices based on the interplay between the two degrees of freedom [6,14-18].

In semiconductor devices, the spin of carriers has played a minor role so far because the most-well established semiconductor devices based on Si and GaAs are non-magnetic and show only negligible effects of spin. On the other hand, from the physical points of view, the enhanced spin-related phenomena due to the coexistence of the magnetism and semiconductor properties have been recognized in magnetic semiconductors and diluted magnetic semiconductors (DMS) (or semimagnetic semiconductors; SMSC) since the 60s. The family of magnetic semiconductors encompasses europium and chromium chalcogenides (rock-salt type: EuSe, EuO and spinels: $CdCr_2S_4$, $CdCr_2Se_4$), which show ferromagnetic order at low temperatures with the Curie temperature T_C = 100 K. They have been extensively studied, because of their peculiar properties resulting from the exchange interaction between itinerant electrons and localized magnetic spins (s-f and s-d exchange interactions) [19-21]. Owing to

these interactions, magnetic semiconductors exhibit a rich variety of striking optical and transport phenomena, which are strongly affected by the magnetic field and the magnetic order, particularly near the metal-to-insulator transition (MIT). However, difficulties in material preparation and in fabrication of heterostructures make this family of compounds less attractive from the application point of view. Manganites (perovskite: (La,Sr)MnO_3 and related materials), which show colossal magnetoresistance (CMR), are magnetic semiconductors, whose studies have been particularly active over the recent years. Their ferromagnetic order, beginning at ~350 K, originates from the double-exchange interaction. Properties of manganites and their epitaxial heterostructures are currently studied aggressively [22-24]. Their compatibility to the well-established electronic devices is an open issue because of the differences in both crystal structure and constituting elements.

DMS are based on non-magnetic semiconductors, and are obtained by alloying them with a sizable amount (a few percents or more) of magnetic elements, such as Mn. The studies of DMS and their heterostructures have offered a wide variety of materials and structures, making it possible to explore further the effect of the exchange interaction in semiconductors. Most of the work had been centered around II-VI based materials such as (Cd,Mn)Te, (Zn,Co)S, (Hg,Fe)Se, where the valence of group II cations is identical to that of most magnetic transition metals [25-27]. Although this made them relatively easy to prepare, difficulties in doping of II-VI-based DMS to either p- or n-type as well as relatively weak bonds made these materials less attractive for applications. The magnetic properties of II-VI DMS are dominated by the antiferromagnetic super-exchange interactions among the localized spins, which result in paramagnetic, spinglass or antiferromagnetic behavior depending on the concentration of the magnetic ions and temperature. Recent progress in doping of II-VI materials is gradually changing this situation [28-29], for example, hole mediated ferromagnetism was found in p-type II-VI DMS with $T_C < 10$ K [30-32]. Understanding of the carrier-mediated ferromagnetism in semiconductors was put forward by a study of ferromagnetism in IV-VI DMS such as (Pb,Sn,Mn)Te [33]. However, IV-VI DMS and their heterostructures are again rather difficult to prepare.

An approach compatible with the present-day electronic materials is to make non-magnetic semiconductors magnetic, and even ferromagnetic, by introducing a high

concentration of magnetic ions. III-V compound semiconductors are widely used for high-speed electronic devices as well as for optoelectronic devices. Moreover, heterostructures based on the GaAs/(Al,Ga)As systems have proven to be a convenient test bench for a new physics and device concepts. Introduction of magnetic III-V compounds opens, therefore, up the possibility of using a variety of magnetic and/or spin-dependent phenomena, not present in the conventional non-magnetic III-Vs, in the optical and electrical devices already established (see Figure II.1). The proposal of III-V based magnetic semiconductors with various sets of host materials and transition metals was put forward in 1970s [34], and some experimental studies were then initiated. At that time, however, III-V materials with a sizable concentration of uniformly distributed magnetic elements were not obtained due to the low solubility of transition metals in III-V semiconductors [35]. The application of non-equilibrium methods to grow III-V-based DMS was rewarded by successful molecular beam epitaxy (MBE) of uniform (In,Mn)As films on GaAs substrates [36]. Subsequent discovery of the hole-induced ferromagnetic order in p-type (In,Mn)As [37] encouraged researchers to investigate GaAs-based system [38] and led to the successful growth of ferromagnetic (Ga,Mn)As [39]. Currently, a number of groups is working on the MBE growth of (Ga,Mn)As and related heterostructures to advance the understanding of this new class of materials [40-49].

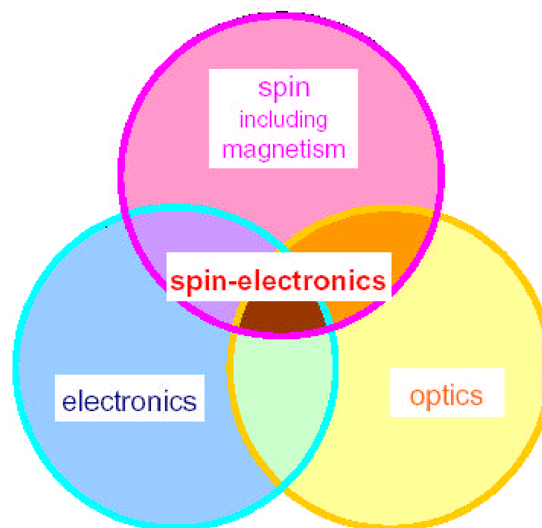

Figure II.1: Concept of spin-electronics (spintronics). In semiconductor spin-electronics spin properties as well as electronic and optical properties are utilized at the same time.

II. 3. Ferromagnetic semiconductors

Today's research on spin electronics involves virtually all material families, the most mature being studies on magnetic metal multilayers, in which spin-dependent scattering and tunnelling are being successfully applied, as already mentioned in reading heads of high density hard-discs and in magnetic random access memories (MRAM). However, in the context of spin electronics particularly interesting are ferromagnetic semiconductors, which combine complementary functionalities of ferromagnetic and semiconductor material systems. One of the relevant questions is to what extend the powerful methods developed to control the carrier concentration and spin polarization in semiconductor quantum structures could serve to tailor the magnitude and orientation of magnetization produced by the spins localized on the magnetic ions.

Another important issue concerns the elaboration of methods of injecting and transporting spin currents. In addition of consisting the important ingredient of field sensors and magnetic transistors, spin injection can serve as a tool for fast modulation of light polarization in semiconductors lasers [27].

Since the fabrication of quantum structures is most mature in the case of III-V semiconducting compounds, the milestone discovery was the detection of the carrier induced ferromagnetism in $In_{1-x}Mn_xAs$ and $Ga_{1-x}Mn_xAs$ by Ohno and Munekata at IBM [37] and Tohoku University [50] groups, respectively. While the divalent Mn introduces both spins and holes in the III-V materials, the magnetic ion and carrier concentrations can be varied independently in II-VI materials, like in the case of IV-VI materials in which the hole-controlled ferromagnetism was put into the evidence in Warsaw University [51].

A systematic experimental and theoretical study of the carrier-induced ferromagnetism in II-VI semimagnetic semiconductors has been undertaken by the Grenoble-Warsaw collaboration [52]. In agreement with the theoretical model proposed by the team for various dimensionality II-VI semimagnetic semiconductors [52], the ferromagnetic order has been observed above 1 K in two dimensional modulation-doped p-type $Cd_{1-x}Mn_xTe/Cd_{1-y-z}Mg_yZn_zTe:N$ heterostructures [53,54]. The obtained results lead to suggest [53] that it will be possible to control magnetic properties by methods elaborated earlier to tune the carrier concentration in quantum structures, such as voltage biasing and light illumination. More

recently, epitaxial layers of $Zn_{1-x}Mn_xTe:N$ with the hole concentration above 10^{20} cm^{-3} have been obtained. By means of transport and magnetic measurements, the ferromagnetism was found in this three dimensional system [31,55], corroborated the theoretical predictions mentioned above [55]. Ferromagnetic correlation has been detected also in $Be_{1-x}Mn_xTe:N$ [56] as well as in bulk crystal of $Zn_{1-x}Mn_xTe:P$ [55,56]. At the same time, in agreement with the theoretical expectations [52], no ferromagnetism has been detected above 1 K in n-type films of $Zn_{1-x}Mn_xO:Al$ [55]. The stronger ferromagnetism in p-type materials comparing n-type compounds stems from a large magnitude of the hole density of states and a strong spin-dependent hybridization between the valence band p-like states and the Mn d orbitals. These two effects conspire to make the hole-mediated ferromagnetic interactions strong enough to overcome the antiforromagnétic super-exchange, specific to intrisic DMS.

Theoretical studies undertaken simultaneously lead to the elaboration of a theoretical model of thermodynamic, magneotoelastic and optical properties of III-V and II-VI ferromagnetic semiconductors [3157,58]. The model takes into account the *k.p* and spin-orbit interactions, biaxial strain and confinement; it applies for both zincblende and wurzite compounds. It has been demonstrated that this model describes, with no adjustable parameters, the Curie temperature, the dependence of magnetization on temperature and the magnetic field, and the magnetic anisotropy energies in p-$Ga_{1-x}Mn_xAs$ [56,57] as well as the magnetic circular dichroism [58,59]. The theoretical and numerical analysis [31,52-54,58,59] made it possible to describe quantitatively the dominant mechanism accounting for the ferromagnetism of the studied systems as well as for the demonstration of the role played by the space dimensionality, spin-orbit interaction, and interband polarization as well as for the identification of main differences between properties of III-V and II-VI compounds. Furthermore, theory of magnetic domains in III-V materials has been developed providing, among other things, the width of domains walls as well as the critical film size corresponding to the transition to a single domain structure [60]. Theoretical studies [57,58,60] have demonstrated that the spin-orbit coupling in the valence band, not at the magnetic ion, accounts for the magnetoelastic properties and magnetic anisotropy in the systems in question.

One has to emphasize that the results described above have been obtained for magnetic semiconductors in which the highest value of Curie temperature does not exceed 110 K [50]. For this reason, the theoretical work has been undertaken [57] aiming at evaluation the magnitudes of expected Curie temperatures in various III-V and II-VI compounds as well as in elemental group IV semiconductors [57,58]. The results shown in Figure II.2 demonstrate that in semiconductors consisting of light elements, the critical point may exceed the room temperature [57,58]. These predictions have encouraged many groups to synthesize such materials as GaN and ZnO containing Mn or other transition metals as well as to search of ferromagnetic elemental semiconductors. Before presenting promising experimental results we have to caution the readers that in some cases the observed ferromagnetism might have been resulted from ferromagnetic or ferrimagnetic inclusions or precipitates.

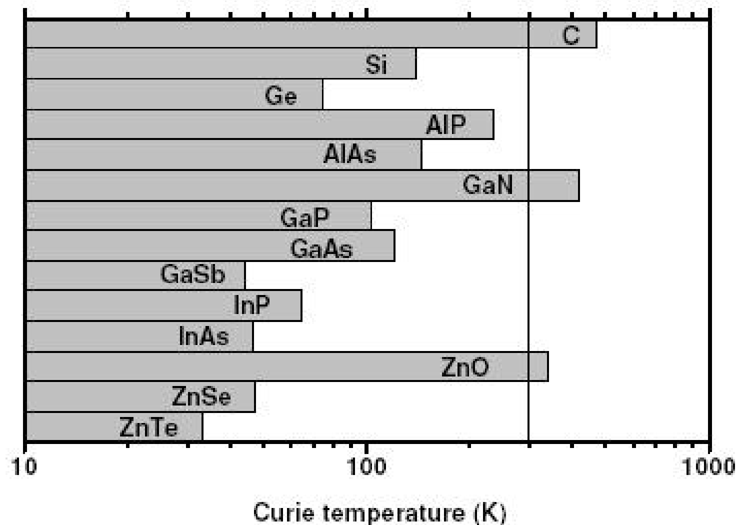

Figure II.2. Computed values of the Curie temperature T_C for various p-type semiconductors containing 5% of Mn per cation (2.5% per atom) and 3.5×10^{20} holes per cm^3. (after [61,62]).

II. 4. III-Nitrides based diluted magnetic semiconductors

From the standpoint of technology, superdoping (here doping beyond 1%) is relatively easy only in the case of ''soft'' semiconductors like GaAs, InAs, or CdTe. This is not the case with ''hard'' semiconductors like GaN or AlN. These materials need relatively high growth temperatures to obtain good crystalline quality. At such high temperatures superdoped transition-metal impurities cause segregation or form a compound with the host semiconductor elements. In order to obtain an extremely heavy doping of Mn, a highly nonequilibrium growth process is necessary. That is why less attention was paid to magnetically doped GaN: ($3d$ -transition-metal) systems, although this class of DMS has been predicted to be ferromagnetic at room temperature [57].

GaN-based DMS's are quite promising for various spin controlled and photonic devices because of the wide gap corresponding to visible light. Another attractive property of GaN:Mn is its half-metallic ferromagnetism, that is, a 100% spin polarization of carriers at the Fermi energy. This provides an opportunity to overcome the intrinsic difficulty of injecting spins into a nonmagnetic semiconductor. Recently, a similar injection and evidence of spin-polarized current in III-V semiconductor has been demonstrated and a large signal from half-metallic DMS's was predicted [61]. The growth of superdoped GaN:Mn using an ultrahigh-vacuum chemical vapor description system was reported [62]. In that study superconducting quantum interference device (SQUID) magnetization measurements showed the magnetic hysteresis at room temperature, i.e., the existence of room temperature ferromagnetism in granular GaN:Mn [63]. Moreover Curie temperatures for the epitaxial wurtzite GaN:Mn films were also recently reported as high as 940 K (Ref. 62 (deduced from extrapolating SQUID measurements) and around room temperature [63] (from the anomal Hall effect). These experimental results give a strong impetus to band structure studies of superdoped GaN:Mn. A quantitative understanding of the properties of a material, especially the electronic states induced by a transition-metal dopant, is a clue to the material design of a class of magnetic semiconductors.

[1] K.-M. H. Lenssen, A.E.T. Kuiper, F. Roozenboom, J. Appl. Phys. **85,** 5531 (1999).
[2] I.K. Schuller, S. Kim, C. Leighton, J. Magn. Magn. Mater. **200**, 571 (1999).
[3] J.S. Moodera, L.R. Kinder, T.M. Wong, R. Meservey, Phys. Rev. Lett. **74**, 3273 (1995);
[4] J.S. Moodera, G. Mathon, J. Magn. Magn. Mater. **200**, 248 (1999).
[5] A.Fert, J. Barnaœ, Phys. Rev. Lett. **80**, 1058 (1998).
[6] G.A. Prinz, Science **282**, 1660 (1998); J. Magn. Magn. Mater. **200**, 57 (1999).
[7] J.-G. Zhu, Y. Zheng, G.A. Prinz, J. Appl.Phys. **87**, 6668 (2000).
[8] P.S. Anil Kumar, R. Jansen, O.M.J. Van Erve, R. Vlutters, P. de Haan, J.C. Lodder, J. Magn. Magn. Mater. **214**, L1 (2000).
[9] A.Stean, Rep. Prog. Phys. **6**, 117 (1998); C.H. Benett, D.P. Di Vincenzo, Nature **404**, 247 (2000).
[10] G. Burkard, D. Loss, D. Di Vincenzo, Phys. Rev. B **59**, 2070 (1999).
[11] D.P. DiVincenzo, J. Appl. Phys. **85**, 4785 (1999).
[12] B.E. Kane, Nature **393**, 133 (1998). J.M. Kikkawa, D.D. Awschalom, Nature **397**, 141 (1999).
[13] J.M. Kikkawa, D.D. Awschalom, Nature **397**, 141 (1999).
[14] J. De Boeck, and G. Borghs, Phys. World, No **4**, 27 (1999).
[15] S.A. Wolf, J. Supeconductivity **13**, 195 (2000).
[16] P. Ball, Nature **404**, 918 (2000).
[17] M. Ziese, and M. J. Thornton, *Spin Electronics* (eds. Springer, 2001).
[18] S. Wolf, D. D. Awshalom, R. A. Buhrman, J. M. Daughton, S. von Molnár, M. L. Roukes, A. Y. Chtchelkanova and D. M. Treger, Science **294**, 1488 (2001).
[19] T. Kasuya, and A. Yanase, Rev. Mod. Phys. **40,** 684 (1968).
[20] S. Methfessel and D. C. Mattis, in: H. P. J. Wijn ed. Encyclopedia of Physics Vol. XVIII/1 *Magnetism, Magnetic Semiconductors* (Springer-Verlag, Berlin, 1968) pp.389-562.
[21] A. Mauger and C. Gotard, Phys. Rep. **141**, 51 (1986).
[22] J.M.D.Coey, M. Viret and S. von Molnár, Adv. Phys. **48**, 167 (1999).
[23] Y. Tokura and Y. Tomioka, J. Magn. Magn. Matter. **200**, 1 (1999).
[24] Y. Tokura, in: *Clossal Magnetoresistive Oxides*, ed. Y. Tokura (Gordon & Breach Science Publishers, London, 2000).
[25] J. Furdyna and J. Kossut, *Semiconductor and Semimetals*, Vol. 25, (eds. Academic, New York 1988).
[26] J. Kossut and W. Dobrowolski, in: Buschow, K. H. J. (Ed.), Handbook of Magnetic Materials, Vol. 7 North-Hoalland, Amsterdam 1993.

[27] T. Dietl, (*Diluted) Magnetic Semiconductors*, in: T. S. Moss (Ed.), Handbook of Semiconductors, Vol. 3B, North-Hoalland, Amsterdam 1994.

[28] N. Shibata, A. Ohki and A. Katsui, J. Cryst. Growth **93**, 703 (1988).

[29] T. Baron, S. Tatarenko, K. Saminadayer, N. Magnea, and J. Fontenille, Appl. Phys. Lett. **65**, 1284 (1994).

[30] D. Ferrand, J. Cibert, A. Wasiela, C. Bourgognon, S. Tatarenko, G. Fishman, S. Koleœnik, J. Jaroszyñski, T. Dietl, B. Barabara and D. Dufeu, J. Appl. Phys. **87**, 6451 (200).

[31] D. Ferrand, J. Cibert, A. Wasiela, C. Bpurgognon, S. Tatarenko, G. Fishman, T. Andrearczyk, J. Jaroszyñski, S. Koleœnik, T. Dietl, B. Barbara and D. Dufeu, Phys. Rev. B **63**, 085201 (2001).

[32] L. Hansen, D. Ferrand, G. Richter, M. Thierley, V. Hock, N. Schwarz, G. Reuscher, G. Scmidt, A. Waag and L. W. Molenkamp, Appl. Phys. Lett. **79**, 3125 (2001).

[33] T. Story, R. R. Ga³azka, R. B. Frankel and P. A. Wolf, Phys. Rev. Lett. **56**, 777 (1986).

[34] R.R. Ga³ zka, Postêpy Fyzyki **28**, 601 (1977).

[35] M.I. Aliyev, I.S. Dadashev and G.I. Safaraliyev, Phys. Met. Metallogr. **49**, 166 (1980).

[36] H. Munekata, H. Ohno, S. von Molnár, A. Segmüller, L. L. Chang and L. Esaki, Phys, Rev. Lett. **56**, 777 (1989).

[37] H. Ohno, H, Munekata, T. Penny, S. von Molnár and L. L. Chang, Phys. Rev. Lett. **68**, 2664 (1992).

[38] J. De Boeck, R. Oesterholt, A. Van Esch, H. Bender, C. Bruynseraede, C. Van Hoof and G. Borghs, Appl. Phys. Lett. **68**, 2744 (1996).

[39] H. Ohno, A. Shen, F. Matsukura, A. Oiwa, A. Endo, S. Katsumoto and Y. Iye, Appl. Phys. Lett. **69**, 363 (1996).

[40] H. Ohno, F. Matsukura, A. Shen, Y. Sugawara, A. Oiwa, A. Endo, S. Katsumoto and Y. Iye, in: M. Scheffler and R. Zimmermann (Eds.), Proceedings of the 23rd International Conference on Physics of Semiconductors, World Scientific, Singapore (1996), pp. 405-408.

[41] Y. Ohno, D. K. Young, B. Beshoten, F. Matsukura, H. Ohno and D. D. Awschalom, Nature **402**, 790 (1999).

[42] T. Hayashi, M. Tanaka, T. Nishinaga, H. Shimada, H. Tsuchiya and Y. Ohtsuka, J. Cryst. Growth **175/176**, 1063 (1997).

[43] Y. Nishikawa, Y. Satoh and J. Yoshino, Second Symposium on Physics and Application of Spin Related Phenomena in Semiconductors, 27-28 Jan 1997, Sendai, Japan, p. 122.

[44] A. Van Esch, L. Van Bockstal, J. De Boeck, G. Verbanck, A. S. van Sternbergen, P. J. Wellman, B. Grietens, R. Begaerts, F. Herlach and G. Borghs, Phys. Rev. B **56**, 13103 (1997).

[45] J. Sadowski, J. Domagala, J. Bak-Misiuk, K Sqiatek, J. Kanski, L. Ilver and H. Oscarsson, Acta Physica Polonica A **94**, 509 (1998).

[46] R.K. Kawakami, E. Hohnston-Halperin, L. F. Chen, M. Hanson, N. Guébels, J. S. Speck, A. C. Gossard, and D. D. Awshalom, Appl. Phys. Lett. **77**, 2379 (2000).

[47] S. J. Potashnik, K. C. Ku, S. H. Chun, J. J. Berry, N. Samarth and P. Schiffer, Appl. Phys. Lett. **79**, 1495 (2001).

[48] G.M. Schott, W. Faschinger and L. W. Molenkamp, Appl. Phys. Lett. **79**, 1807 (2001).

[49] X. Liu, Y. Sasaki and J. K. Furdyna, Appl. Phys. Lett. **79**, 2414 (2001).

[50] H. Ohno, Science **281**, 951 (1998).

[51] T. Story, R.R. Gazka, R.B. Frankel, P.A. Wolff, Phys. Rev. Lett. **56**, 777 (1986).

[52] T. Dietl, A. Haury, Y. Merle d'Aubigné, Phys. Rev. B **55**, R3347 (1997).

[53] A. Haury, A. Wasiela, A. Arnoult, J. Cibert, S. Tatarenko, T. Dietl, Y. Merle d'Aubigné, Phys. Rev. Lett. **79**, 511 (1997).

[54] P. Kossacki, D. Ferrand, A. Arnoult, J. Cibert, Y. Merle d'Aubidné, A. Wasiela, S. Tateranko, J.-L. Staehl, T. Dietl, in: Optical Properties of Semiconductor Nanostructures, eds. M.L. Sadowski, M. Potemski, M. Grynberg (Kluwer, Dordrecht, 2000) p. 225; P. Kossacki, D. Ferrand, A. Arnoult, J. Cibert, S. Tatarenko, A. Wasiela, Y. Merle d'Aubigné, J.-L. Staehli, J.-D. Ganiere, W. Bardyszewski, K. Œwi¹tek, M. Sawicki, J. Wróbel, T. Dietl, Physica E **6**, 709 (2000).

[55] T. Andrearczyk, J. Jaroszyñski, M. Sawicki, Le Van Khoi, T. Dietl, D. Ferrand, C. Bourgognon, J. Cibert, S. Tatarenko, T. Fukumura, Z. Jin, H. Koinuma, M. Kawasaki, in: Proceedings 25th Intl. Conf. on Physics of Semiconductors, Osaka, Japan, 2000, eds. N. Miura, T. Ando (Springer, Berlin, 2001) p. 235.

[56] M. Sawicki, L. Hansen, D. Ferrand, L.W. Molenkamp, A. Waag, Le Van Khoi and T. Dietl, Phys. Status Solidi B **229,** 717 (2002).

[57] T. Dietl, H. Ohno, F. Matsukura, J. Cibert, D. Ferrand, Science **287**, 1019 (2000).

[58] T. Dietl, H. Ohno, F. Matsukura, Phys. Rev. B **63**, 195205 (2001).

[59] J. Szczytko, W. Mac, A. Twardowski, F. Matsukura, H. Ohno, Phys. Rev. B **59**, 12935 (1999); J. Szczytko, W. Bardyszewski, A. Twardowski, Phys. Rev. B **64**, 075306 (2001).

[60] T. Dietl, J. König, A.H. MacDonald, Phys. Rev. B **64**, 241201(R) (2001).

[61] H. Nakayama and E. Kulatov, invited lecture in *Proceedings of the Sixth International Symposium on Advanced Physical Fields (APF-6)*: *Growth of Well-Defined Nanostructures*, edited by N. Koguchi (Tsukuba, Japan, 2001), p. 28.

[62] S. Sonoda, S. Shimizu, T. Sasaki, Y. Yamamoto, and H. Hori, http://xxx.lanl.gov/abs/cond-mat/0108159 (unpublished).

[63] M. L. Reed, N. A. El-Masry, H. H. Stadelmaier, M. K. Ritums, M. J. Reed, C. A. Parker,J. C. Roberts, and S. M. Bedair, Appl. Phys. Lett. **79**, 3473 (2001).

Chapter III

Density Functional Theory

- DFT -

Abstract :

In solids one often starts with an ideal crystal that is studied on the atomic scale at zero temperature. The unit cell may contain several atoms (at certain positions) and is repeated with periodic boundary conditions. Quantum mechanics governs the electronic structure that is responsible for properties such as relative stability, chemical bonding, relaxation of the atoms, phase transitions, electrical, mechanical, optical or magnetic behavior, etc. Corresponding first principles calculations are mainly done within density functional theory (DFT) which is mapped to a series of one-electron equations, the so-called Kohn–Sham (KS) equations.

This chapter is devoted to deal with the current advances in the theoretical modeling of DFT. The basic principles of this method are more detailed. The exchange-correlation part of this functional is discussed, including both the local density approximation and generalized gradient approximation.

III. 1. Introduction :

The predominant theoretical picture of solid-state and/or molecular systems involves the inhomogeneous electron gas: a set of interacting point electrons moving quantum mechanically in the potential field of a set of atomic nuclei, which are considered to be static (the Born-Oppenheimer approximation). Solution of such models generally requires the use of approximation schemes (the independent electron approximation, the Hartree theory, and Hartree-Fock theory). However, there is another approach (density functional theory (DFT) [1-5]) which over the last 30 years or so has become increasingly the method of choice for the solution of such problems (see Figure III.1). This method has the double advantage of being able to treat many problems to a sufficiently high accuracy, as well as being computationally simple (simpler than even the Hartree scheme).

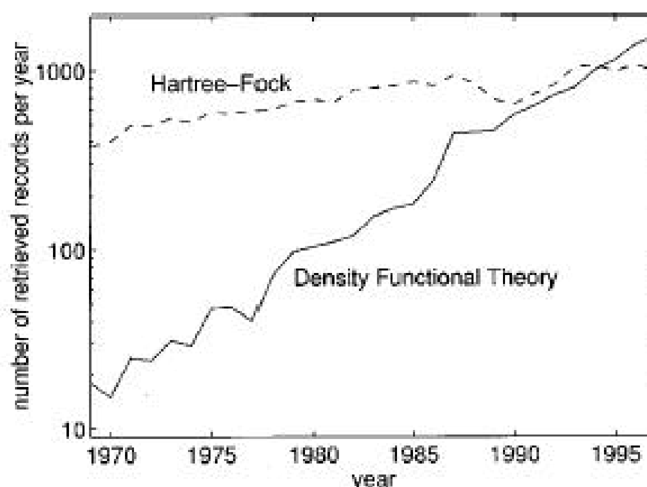

Figure III.1. One indicator of the increasing use of DFT is the number of records retrieved from the INSPEC databases by searching for the keywords ‘‘density,’’ ‘‘functional,’’ and ‘‘theory.’’ This is compared here with a similar search for keywords ‘‘Hartree’’ and ‘‘Fock,’’ which parallels the overall growth of the INSPEC databases for any given year, approximately 0.3% of the records have the Hartree–Fock keywords [6].

Condensed matter physics and materials science are basically related to the understanding and exploiting the properties of systems of interacting electrons and atomic nuclei. In principle, all the properties of materials can be addressed given suitable computational tools for solving this quantum mechanics problem. In fact, through the knowledge of the electronic properties it is possible to obtain information on structural, mechanical, electrical, vibrational, thermal and optical properties. However, the electrons and nuclei that compose materials constitute a strongly interacting many body systems and unfortunately this makes the direct solution of the Schrödinger's equation an impractical proposition. As stated by Dirac in the far 1929 [7], progress depends mostly on the elaboration of sufficiently accurate and approximate techniques.

The development of density functional theory and the demonstration of the tractability and accuracy of the local density approximation (LDA) represents an important milestone in condensed matter physics. First principles quantum mechanical calculations based on the LDA have become one of the most frequently used theoretical tools in materials science. Nonetheless, the great contribution of the local density approximation calculations remained limited until the late 1970's when several works have demonstrated the accuracy of the approach in determining properties of solids [8-11]. Even though it has been a great deal to state why the LDA should or should not be adequate for calculating properties of materials, there is however no doubt that the most convincing arguments have been derived from the direct comparison of calculations with experiments.

In particular, despite its simplicity the local density approximation has been very successful in describing materials properties during the last decades. However, it is worth to note that there are also situations where the above approach does not lead to sufficiently accurate results. This can be the case when the differences in the total energy, which are usually relevant in calculating structural properties and binding, are to be estimated very accurately. As a matter of fact, small inaccuracies may have here dramatic effects.

In general, LDA suffers from more or less well-known failures and therefore there have during the last decade been several attempts to go beyond this local approximation by including effects depending on the variation of the electron density. Nowadays, improved theoretical schemes and the rapid growth in computing facilities have caused many types of systems and properties to be studied successfully with density functional methods. In the next following Sections we briefly resume the fundamental concepts, which are at the base of this important and fascinating theory.

III. 2. The basic principles of the method :

The well-established scheme to calculate electronic properties of solids is based on the DFT, for which Walter Kohn has received the Nobel Prize in chemistry in 1998. DFT is a universal approach to the quantum mechanical many-body problem, where the system of interacting electrons is mapped in a unique manner onto an effective non-interacting system that has the same total density. Hohenberg and Kohn [5] have shown that the ground state electron density $\boldsymbol{r}$ (in atoms, molecules or solids) uniquely defines the total energy E, must be a functional of the density.

$$E = E(\boldsymbol{r}) \qquad \text{(III-1)}$$

They further showed that the true ground state density is the density that minimises $E(\boldsymbol{r})$ and that the other ground state properties are also functionals of the ground state density. The extension to spin-polarised systems is also possible where E and the other ground state properties become functionals of both the up and down spin densities:

$$E = E(\boldsymbol{r}_{\uparrow}, \boldsymbol{r}_{\downarrow}) \qquad \text{(III-2)}$$

Thus one does not need to know the many-body wave function. The non-interacting particles of this auxiliary system move in an effective local one-particle potential, which consists of a classical mean-field (Hartree) part and an exchange-correlation part V_{xc} (due to quantum mechanics) that, in principle, incorporates all correlation effects exactly.

In order to do this, the unknown functional $E\ (\rho)$ is rewritten as the Hartree total energy plus another smaller unknown functional called exchange-correlation (xc) functional, $E_{xc}\ (\rho)$.

$$E(\rho) = T_s(\rho) + E_C(\rho) + E_H(\rho) + E_{ii}(\rho) + E_{xc}(\rho) \tag{III-3}$$

In equation III-3, $T_s\ [\rho]$ represents the single particle kinetic energy while $E_C\ [\rho]$ denotes the Coulomb interaction energy between the electrons and the nuclei. The term $E_{ii}\ [\rho]$ arises from the interaction of the nuclei with each other and $E_H\ [\rho]$ is the Hartree component of the electron-electron energy.

$$E_H(\rho) = \frac{e^2}{2}\int d^3r\, d^3r' \frac{\rho(\vec{r})\rho(\vec{r}')}{|\vec{r}-\vec{r}'|} \tag{III-4}$$

According to the variational principle a set of effective one-particle Schrödinger equations, the so-called Kohn–Sham (KS) equations [12], must be solved. Its form is

$$[T_s + V_C(\vec{r}) + V_H[\rho(\vec{r})] + V_{xc}[\rho(\vec{r})]]\Phi_i(\vec{r}) = \varepsilon_i \Phi_i(\vec{r}) \tag{III-.5}$$

when written in Rydberg atomic units for an atom with the obvious generalization to molecules and solids. The four terms represent the kinetic energy operator, V_H is the Hartree potential, the Coulomb-, and exchange-correlation potential, V_C and V_{xc}: The KS equations must be solved iteratively until self-consistency is reached. The iteration cycles are needed because of the interdependence between orbitals and potential.

$$\rho(\vec{r}) = \sum_i^{occ} [\phi_i(\vec{r})]^2 \tag{III-6}$$

From the electron density the V_C and V_{xc} potentials for the next iteration can be calculated, which define the KS orbitals. This closes the self-consistent loop. The exact functional form of the potential V_{xc} is not known and thus one needs to make approximations.

Early applications were done by using results from quantum Monte Carlo calculations for the homogeneous electron gas, for which the problem of exchange and correlation can be solved exactly, leading to the original local density approximation (LDA). LDA works reasonably well but has some shortcomings mostly due to the tendency of overbinding, which cause e.g., too small lattice constants.

Modern versions of DFT, especially those using the generalized gradient approximation (GGA), improved the LDA by adding gradient terms of the electron density and reached (almost) chemical accuracy, as for example the version by Perdew, Burke, Ernzerhof (PBE) [13].

III. 3. The local -(spin-) density approximation (LDA, LSDA):

In the effective potential of the Kohn-Sham equation, the only term that cannot be determined exactly is the exchange-correlation energy E_{xc}. The most commonly used technique for calculating E_{xc} is the local-spin-density approximation (LSDA) or simply local-density approximation (LDA) [14]. We summarize the essence of the LDA bellow:

- The inhomogeneous system is divided into a certain set of small regions containing a homogeneous interacting electron gas. Such a gas is completely characterized by the density $\rho_\sigma(r)$, where $\sigma = \uparrow or \downarrow$.
- In each region, the exchange-correlation energy per particle of the homogeneous gas,

$\varepsilon_{xc}(\rho_\uparrow, \rho_\downarrow) \equiv \varepsilon_x(\rho_\uparrow, \rho_\downarrow) + \varepsilon_c(\rho_\uparrow, \rho_\downarrow)$, can be calculated. The analytic expression for the exchange energy $\varepsilon_x(\rho_\uparrow, \rho_\downarrow)$ can be obtained from the Hartree-Foch approximation [15-17]. For the correlation energy $\varepsilon_c(\rho_\uparrow, \rho_\downarrow)$, we use an analytical expression of Volso, Wilk and Nusair (VWN) [18], which is based on the quantum Monte-Carlo result of the ground-state energy for the homogenous electron gas [19].

- The total exchange-correlation energy is the sum of the contribution of all regions :

$$E_{xc}^{LDA}(\rho_\uparrow,\rho_\downarrow)=\int \varepsilon_{xc}(\rho_\uparrow(\vec{r}),\rho_\downarrow(\vec{r}))\rho(\vec{r})d^3r \qquad \text{(III-7)}$$

where $\rho(\vec{r})\equiv\rho_\uparrow(\vec{r})+\rho_\downarrow(\vec{r})$. The exchange-correlation potential is calculated from

$$V_{xc}^{LDA}(x)=\frac{\delta E_{xc}}{\delta\rho_\sigma(\vec{r})}=\varepsilon_{xc}(\rho_\uparrow,\rho_\downarrow)+\frac{\delta\varepsilon_{xc}(\rho_\uparrow,\rho_\downarrow)}{\delta\rho_\sigma(\vec{r})}\rho(\vec{r}) \qquad \text{(III-8)}$$

The derivation of $V_{xc}^{LDA}(x)$ with the VWN expression is given by Painter [20].

III. 4. Generalized gradient approximation (GGA):

In the generalized gradient approximation, the exchange-correlation energy E_{xc} is a functional of the local electron spin densities ρ_σ(r) and their gradients :

$$E_{xc}^{GGA}(\rho_\uparrow,\rho_\downarrow)=\int \varepsilon_{xc}(\rho_\uparrow(\vec{r}),\rho_\downarrow(\vec{r}))\rho(\vec{r})\nabla\rho(\vec{r})d^3r \qquad \text{(III-9)}$$

From incorporating the additional information contained in the local gradient a better description of the system is expected [21-23]. Several different parameterisations of the GGA functional have been proposed [23] and tested on a wide variety of materials. The GGA improve significantly the ground state properties of light atoms, molecules and solids and generally tends to produce larger equilibrium lattice parameters with respect to the LDA.

III. 5. Single particle Kohn-Sham equation:

Depending on the representations that are used for density, potential and KS orbitals, different DFT based electronic structure methods can be classified. Many different choices are made in order to minimise the computational and human costs of calculations, while maintaining sufficient accuracy. A brief summary of the many possibilities to solve the Schrödinger's equation is given in Figure III.2. In this Thesis calculations have been mostly concerned with the Linearized / Augmented Plane Wave plus Local Obitals (L/APW+lo).

However, this computational approache is usually reliable only when applied to crystalline materials with high symmetry and large compactness.

The explicit use of a basis can be avoided in constructing the KS orbitals by numerically solving the differential equations on grids. However, it is important to note that nearly all approaches that have been proposed for solids, including the L/APW+lo methods, do rely on a basis set expansion for the KS orbitals. Because of this, the discussion is here confined to methods that do use a basis in which the KS orbitals are:

$$\boldsymbol{j}(\vec{r}) = \sum C_{i\boldsymbol{a}} \boldsymbol{f}_{\boldsymbol{a}}(\vec{r}) \qquad \text{(III-10)}$$

where the $\boldsymbol{j}(\boldsymbol{r})$ are the basis functions and the $C_{i\boldsymbol{a}}$ are the expansion coefficients. Given a choice of basis, the coefficients are the only variables in the problem, since the density depends only on the KS orbitals.

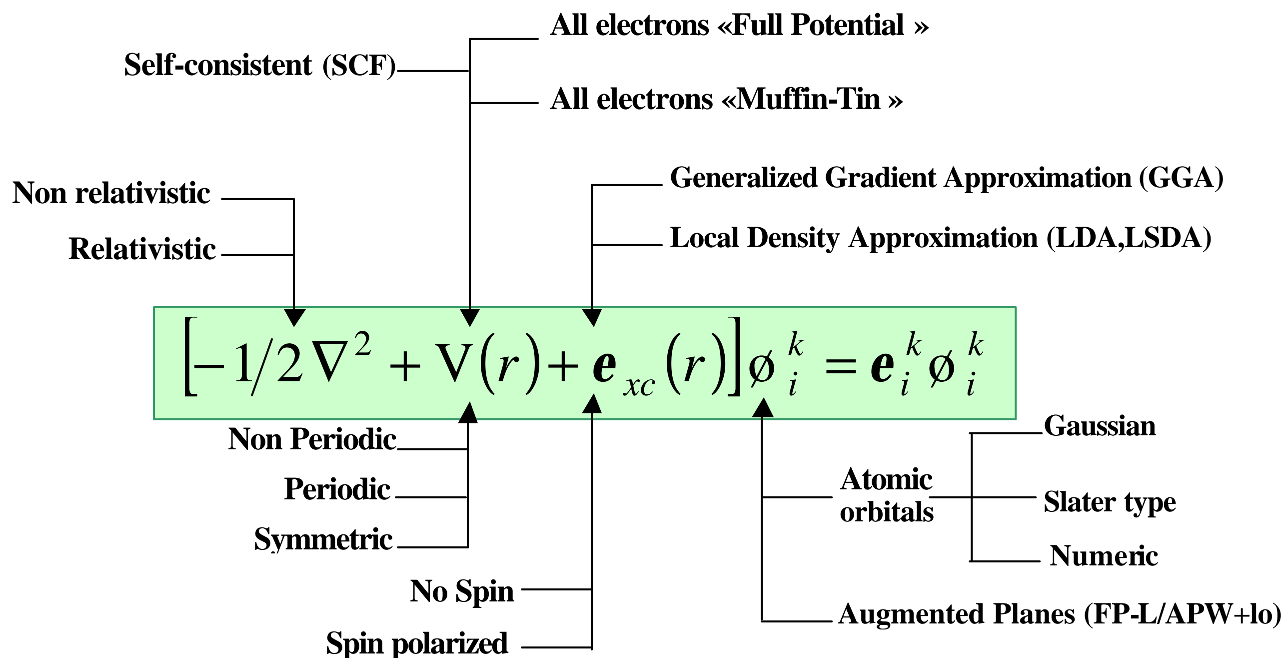

Figure III.2: Schematic representation of various DFT-based methods of calculation.

Since the total energy in DFT is variational, the solution of the self-consistent KS equations permits to determine the $C_{i\mathbf{a}}$ for the occupied orbitals that minimise the total energy. In order to eliminate the unknown functional $T_s[\mathbf{r}]$ the total energy can be rewritten using the single particle eigenvalues:

$$E(\mathbf{r}) = E_{ii}(\mathbf{r}) + \sum_{occ} \boldsymbol{e}_i + E_{xc}(\mathbf{r}) - \int d^3 r \mathbf{r}(\vec{r})\left(V_{xc}(\vec{r}) + \frac{1}{2} V_H(\vec{r})\right) \quad \text{(III.11)}$$

where the sum is over the occupied orbitals and $\mathbf{r}$; V_H and V_{xc} are given by Eqs. III-4, III-6 and III-8, respectively.

Density functional calculations require the optimisation of the $C_{i\mathbf{a}}$ and the determination of the charge density (see Figure III.3). This procedure is usually performed separately and hierarchically. Using standard matrix techniques it is possible to repeatedly determine the $C_{i\mathbf{a}}$ that solve the single Eq. III-5 for a fixed charge density. Hence, given the basis, the Hamiltonian and the overlap matrices, H and S, can be constructed and the following matrix eigenvalue equation,

$$(H - \boldsymbol{e}_i S)C_i = 0 \quad \text{(III-12)}$$

The equation (III-12) is solved at each k-point in the irreducible wedge of the Brillouin zone. The optimised $C_{i\mathbf{a}}$ will yield the exact self-consistent solution only if the true occupied KS orbitals can be expressed as a linear combination of the basis functions. In the case where they cannot be expressed exactly in term of the basis, an approximate optimal solution (i.e the one that gives the lowest possible total energy for the basis) will be found. Therefore, the quality of a basis set can be measured by comparing how much the total energy evaluated with the orbitals of Eq. III-10 differs from the true KS energy.

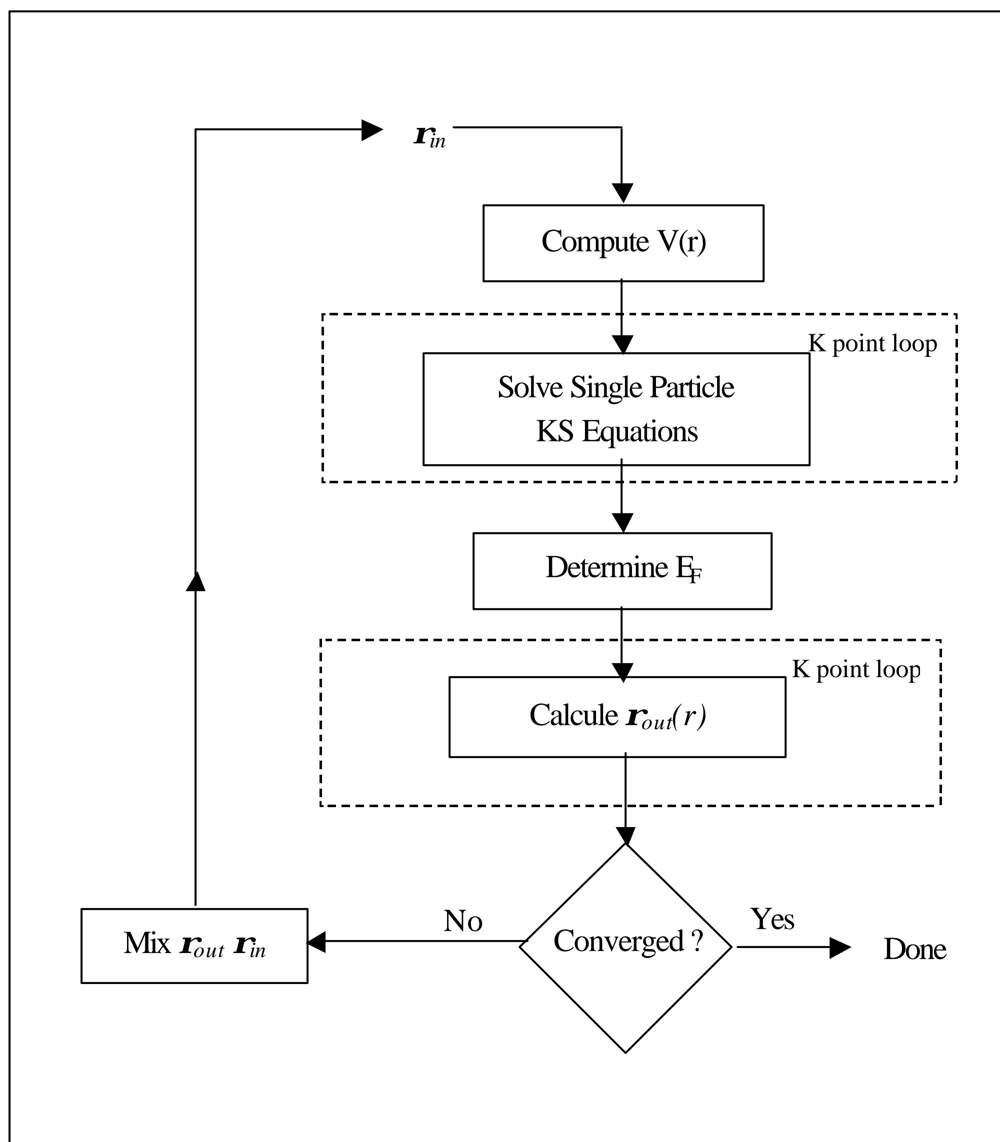

Figure III.3: Flow-chart for self-consistent density functional calculations.

III. 6. The basis sets

With the general term efficiency we usually refer to the number of basis functions needed to achieve a given level of convergence, whereas with the bias we describe whether or not a basis could favour certain regions of space over the others like, for example, being more flexible near the nuclei than the interstitial regions. By looking at the difficulty in estimating the matrix elements, the simplicity of the basis is also defined. The basis completeness indicates whether the basis can be improved by increasing the number of the functions. Plane wave sets are known to be inefficient in the above sense for a large part of solids. However, this is not necessary a defect since it only reflects the fact that they are unbiased. Moreover, plane waves form a simple and complete basis. Accuracy can be reached by increasing the number of plane waves in the basis and the convergence of a calculation can be monitored by changing the plane wave cut-off.

Furthermore, due to the simplicity of this basis the implementation of the plane wave codes is relatively easy and the matrix elements of many operators can be rapidly estimated. Many operators can be made diagonal since the plane waves expanded wave functions can be transformed efficiently from reciprocal space, i.e. coefficients of the plane wave expansion, to real space using Fast Fouries Transforms (FFT). In particular, it is important to note that the kinetic energy and momentum operators are diagonal in reciprocal space and the operation of the local potentials is diagonal in real space. Looking at the Eq. III-10 it is evident that the most efficient basis set consists of the KS orbitals themselves and an exact calculation is thus achieved using a basis set size equal to the number of occupied orbitals. However, despite this possibility the KS orbitals are, in general, unknown at the beginning of the calculation.

III. 7. The Self Consistent Field in DFT

As shown by the theorem of Hohenberg-Kohn the total energy is variational and this means that the true ground state density is that which minimises the energy. When the LDA approximation is introduced to the $E_{xc}\ [\boldsymbol{r}]$ the true variational principle does not exists anymore and there is no guarantee that the energy obtained by minimising the energy functional will be higher than the exact ground state energy. Consequently, the true ground

state charge density will in general not minimise the approximate energy functional. However, the calculations can be done by knowing that minimising a good approximation to the energy functional, a good energy and density should be obtained. The procedure is thus exact only for the true energy functional. Since we do not know the form of the single particle kinetic energy, $T_s [\rho]$, in Eq. III-3, the minimisation proceeds through the KS equations, where the variation is with respect to the orbitals, or in a basis set expansion to the coefficients $C_{i\alpha}$. With a fixed basis these are the only parameters that can be varied. The problem is to find the coefficients that minimise the energy functional (Eq. III-11) paying attention on keeping the orbitals orthonormal to each other. The direct minimisation of the total energy with respect to the $C_{i\alpha}$ was proposed by Bendt and Zunger in 1982 [24] and is the core of the Car-Parrinello (CP) method [25].

In spite of the computational advantages, this approach has not yet become popular for methods that use non-plane wave basis sets. This is due to the complexity of the optimisation problem where typically hundreds or thousands of parameters are present even for small problems. Therefore, it is because of this complication that historically the standard self-consistency cycle shown in Figure III.2 has been used to refine iteratively the density by alternately solving the Eqs. III-5 and III-6. For a given charge density the Eq. III-12 is diagonalised (ensuring the orthonormal orbitals) and an output charge density is constructed from the eigenvectors using Eq. III-6. This charge density is then mixed with the input to yield a refined input for the next iteration. The simplest mixing scheme is represented by the straight mixing:

$$\rho_{in}^{i+1} = (1-\alpha)\rho_{in}^{i} + \alpha\rho_{out}^{i} \qquad \text{(III-13)}$$

The superscript refers to the iteration number and α is the mixing parameter. In order to avoid the decreasing of the radius of convergence with the increasing, for example, of the unit cell volume a more sophisticated mixing procedure which takes into account the information from previous iterations is used. The convergence is normally accelerated by using the Broyden's method [26].

[1] R. G. Parr and W. Yang, *Density Functional Theory of Atoms and Molecules, (*Oxford University Press, Oxford, 1989).

[2] R. M. Dreizler and E. K. U. Gross, *Density Functional Theory: An Approach to the Quantum Many-Body Problems* (Springer, Berlin, 1990).

[3] W. Kohn and P. Vashishta, ''General density functional theory,'' in *Theory of the nhomogeneous Electron Gas*, edited by S. Lundqvist and N.H. March (Plenum, New York, 1983), pp. 79–147.

[4] W. Kohn, A. D. Becke, and R. G. Parr, ''*Density functional theory of electronic structure*,'' J. Phys. Chem. **100**, 12974–12980 (1996).

[5] H. Hohenberg and W. Kohn, Phys. Rev. B **136**, 864 (1964).

[6] N. Argaman, G. Makov, Am. J. Phys. **68** , 69 (2000).

[7] P.A.M. Dirac, Proc. Roy. Soc. (London), **123**, 714 (1929).

[8] V.L. Moruzzi, J.F. Janak and A.R. Williams, *Calculated Electronic Properties of Metals*, (Pergamon, New York, 1978).

[9] A. Zunger and A.J. Freeman, Phys. Rev. B **15**, 5049 (1977).

[10] A. Zunger and A.J. Freeman, Phys. Rev. B **16**, 906 (1977).

[11] A. Zunger and A.J. Freeman, Phys. Rev. B **16**, 2901 (1977).

[12] W. Kohn and L.S. Sham, Phys. Rev. **140**, A1133 (1965).

[13] J.P. Perdew, K. Burke and M. Ernzerhof, Phys. Rev. Lett. **77**, 3865 (1996).

[14] O. Gunnarsson, and B.I. Lundqvist, Phys. Rev. B. **13**, 4274 (1976)

[15] U. Von Barth and L. Hedin, J. Phys. C **5**, 1629 (1972).

[16] J.C. Slater, Phys. Rev. **81**, 385 (1951).

[17] J.C. Slater, *The Self-Consistent Field for Molecules and Solids*, (McGraw-Hill, New York, 1974).

[18] S. H. Vosko, L. Wilk and M. Nusair, Can. J. Phys. **58**, 1200 (1980).

[19] D.M. Ceperley and B.J. Alder, Phys. Rev. Lett. **45**, 566 (1980).

[20] G.S. Painter, Phys. Rev. B **24**, 4264 (1981).

[21] D.C. Langreth and M.J. Mehl, Phys. Rev. B **28**, 1809 (1983).

[22] A.D. Becke, Phys. Rev. A **38**, 3098 (1988).

[23] J.P. Perdew, J.A. Chevary, S.H. Vosko, K.A. Jackson, M.R. Pederson, D.J. Singh and C. Fiolhais, Phys. Rev. B **46**, 6671 (1992).

[24] P. Bendt and A. Zunger, Phys. Rev. B **26**, 3114 (1982).

[25] R. Car and M. Parrinello, Phys. Rev. Lett. **55**, 2471 (1985).

[26] G. Broyden, Math. Comp. **19**, 577 (1965).

Chapter IV

Full Potential Linearized / Augmented Plane Wave plus Local Orbitals - FP-L/APW+lo -

Abstract :

In this chapter, we attempt to present the fundamental concepts of the linearized / augmented plane wave plus local orbitals (L/APW+lo). We show also the differents versions of (L/APW+lo) and thier main developing steps in terms of linearization, full potential, local orbitals and mixed basis sets.

Once the DFT equations are defined in terms of the functional, there are several techniques to solve them. A natural basis for calculating the one-electron wave functions in periodic solids are plane waves (PWs) corresponding to Bloch functions labeled by the k-vector of the first Brillouin zone (BZ). PWs are, however, a very inefficient basis set for describing the rapidly varying wave functions close to the nuclei. In order to overcome this difficulty one can either eliminate these oscillations, due to the presence of the core electrons, as done in pseudopotential calculations or one can augment the PW basis set. One example of the latter approach has led to the linearized /augmented plane wave plus local orbitals (L/APW+lo) method that is now established to be one of the most accurate schemes and thus will be the focus of the present chapter.

IV. 1. The augmented plane wave method (APW):

In 1937 Slater [1,2] introduced augmented plane waves (APW) as basis functions for solving the one-electron equations, which now correspond to the Kohn–Sham equations within DFT. In the APW scheme the unit cell is partitioned into two types of regions: (i) spheres centered around all constituent atomic sites r_α with a radius R_α, and (ii) the remaining interstitial region, abbreviated as I (see Figure IV.1). In this case the wave functions are expanded into PWs each of which is augmented by atomic solutions in the form of partial waves, i.e. a radial function times spherical harmonics. In particular, radial solutions of Schrödinger's equation are employed inside non overlapping atom centered spheres and plane waves in the remaining interstitial zone.

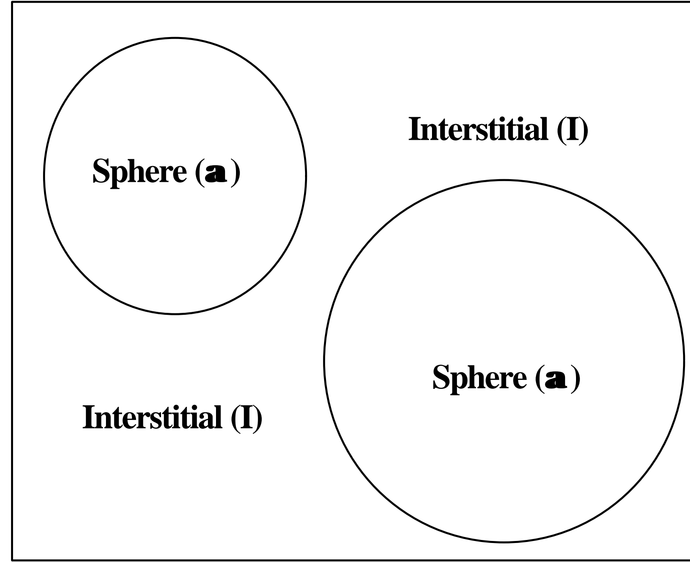

Figure IV.1: Adaptation of the basis set by dividing the unit cell into atomic spheres and interstitial regions.

The introduction of such a basis set is due to the fact that close to the nuclei the potential and wave functions are very similar to those in an atom, while between the atoms then are smoother. The APWs consist of :

$$\boldsymbol{j}(\vec{r}) = \begin{cases} \sum_{lm} a^{a}_{lm} u^{a}_{lm}(r, \boldsymbol{e}) Y_{lm}(\vec{r}), & \mathrm{r} \prec \mathrm{R}_{a} \\ \Omega^{-1/2} \sum_{G} C_G \exp\left(i(\vec{k} + \vec{G}).\vec{r}\right), & \mathrm{r} \in \mathrm{I} \end{cases} \tag{IV-1}$$

In the above relations $\boldsymbol{j}$ is the wave function, $\boldsymbol{W}$ is the unit cell volume, $\vec{r}$ is the position inside sphere $\boldsymbol{a}$ with the polar coordinates $\vec{r}$, $\vec{k}$ is a wave vector in the irreducible Brillouin zone (IBZ) and u_{lm} is the numerical solution to the radial Schrödinger equation at the energy $\boldsymbol{e}$. The KS orbitals $\boldsymbol{y}_i(\vec{r})$ are expressed as a linear combination of APWs $\boldsymbol{j}(\vec{r})$.

Inside the MT sphere a KS orbital can only be accurately described if ε in the APW basis functions is equal to the eigen-energy, ε_i . Therefore, a different energy-dependent set of APW basis functions must be found for each eigenenergy. C_G and a_{lm} are expansion coefficients; E_l is a parameter (set equal to the band energy) and V the spherical component of the potential in the sphere.

$$\left[-\frac{d^2}{dr^2}+\frac{l(l+1)}{r^2}+V(r)-E_l\right]ru_{lm}(r)=0 \tag{IV-2}$$

The use of these functions has been motivated by Slater by noting that plane waves are the solutions of the Schrödinger's equation in a constant potential and radial functions are solutions in a spherical potential. This approximation to the potential is called "muffin-tin" (MT).

Since the continuity on the spheres boundaries needs to be guaranteed on the dual representation defined in Eq. IV-1, constraint must be imposed. In the APW method this is done by defining the u_{lm} in terms of C_G in the spherical harmonic expansion of the plane waves.

$$u_{lm}=\frac{4\pi i^l}{\Omega^{1/2}u_l(R)}\sum_G C_G J_l(|k+g|)Y_{lm}^*(\vec{k}+\vec{G}) \tag{IV-3}$$

The coefficient of each lm is matched at the sphere boundary and the origin is taken at the centre of the sphere (R is the sphere radius). The u_{lm} are determined by the plane wave coefficients (C_G) and the energy parameters E_l, which are the variational coefficients in APW method. The functions labelled G are the augmented plane waves (APWs) and consist of single plane waves in the interstitial zone, which are matched to the radial functions in the spheres.

A more flexible and accurate band structure calculational scheme is the LAPW method where the basis functions and their derivatives are made continuous by matching to a radial function at fixed E_l plus its derivative with respect to E_l.

IV. 2. The linearized augmented plane wave method (LAPW) :

Several improvements to solve the energy dependence of the basis set were tried but the first really successful one was the linearization scheme introduced by Andersen [3] leading to the linearized augmented plane wave method. In LAPW the energy dependence of each radial wave function inside the atomic sphere is linearized by taking a linear combination of a solution u at a fixed linearization energy and its energy derivative $\dot{u}$ computed at the same energy.

$$\boldsymbol{j}(\vec{r}) = \begin{cases} \sum_{lm} \left[a_{lm}^{a} u_{lm}^{a}(r) + b_{lm}^{a} \dot{u}(r)\right] Y_{lm}(\vec{r}), & r \prec R_{a} \\ \Omega^{-1/2} \sum_{G} C_G \exp\left(i(\vec{k}+\vec{G}).\vec{r}\right), & r \in I \end{cases} \qquad \text{(IV-4)}$$

where the b_{lm} are coefficients for the energy derivative analogous to the a_{lm}. The basis functions inside the spheres are linear combinations of a radial functions u_l(r) Y_{lm} (r) and their energy derivatives (u_l(r) Y_{lm} (r) and $\dot{u}_l$(r) Y_{lm} (r) are the augmenting functions). The u_l are defined as in the APW method (Eq. IV-2) and the energy derivative, $\dot{u}_l$(r) Y_{lm} (r), satisfies the following equation:

$$\left[-\frac{d^2}{dr^2} + \frac{l(l+1)}{r^2} + V(r) - E_l\right] r\dot{u}_{lm}(r) = r u_{lm}(r) \qquad \text{(IV-5)}$$

The LAPWs provide a sufficiently flexible basis to properly describe eigenfunctions with eigenenergies near the linearization energy, which can be kept fixed. This scheme allows us to obtain all eigenenergies with a single diagonalization in contrast to APW.

The LAPWs are plane waves in the interstitial zone of the unit cell which match the numerical radial functions inside the spheres with the requirement that the basis functions and their derivatives are continuous at the boundary. In this method no shape approximations are made and consequently such a procedure is often called "full-potential LAPW" (FP-LAPW). The much older muffin-tin approximation corresponds to retain only the $l = 0$ and $m = 0$ component in Eq. IV-5. A spherical average inside the spheres and the volume average in the interstitial region is thus taken.

Inside atomic sphere a linear combination of radial functions times spherical harmonics, Y_{lm}(r), is used. The linear combination of u_l(r) and $\dot{u}_l$(r) constitute the so-called "linearization" of the radial function. u_l(r) and $\dot{u}_l$(r) are obtained by numerical integration of the radial Schrödinger equation on a radial mesh inside the sphere.

The LAPWs have more variational freedom inside the spheres than APWs. This greater exibility is due to the presence of two radial functions instead of one; non-spherical potentials inside spheres can be now treated with no difficulty. There is however, a price to be paid for the additional exibility of the LAPWs: the basis functions must have continuous derivatives and consequently higher plane wave cut-offs are required to achieve a given level of convergence. Further, the asymptote problem (u_{lm}(R) appears in the denominator of expression (Eq IV-3) and if zero leads to a decoupling between planewaves and radial functions. In the vicinity of the asymptote the secular determinant is stronglyvarying) found in the APW method is now overcome by the presence of the non-zero u_{lm}(R) value. The solution of the KS equations are expanded in this combined basis according to the linear variation method:

$$\psi_k = \sum_n c_n \varphi_{kn} \qquad \text{(IV-6)}$$

and the coefficients c_n are determined by the Rayleigh-Ritz variational principle. The convergence of this basis set is controlled by a cut-off parameter $R_{mt} \times K_{max}$, where R_{mt} is the smallest atomic sphere radius in the unit cell and K_{max} is the magnitude of the largest Kn vector in Eq. (IV-6).

IV. 3. The augmented plane wave plus local orbitals method (APW+lo):

Recently, an alternative approach was proposed by Sjöstedt et al. [4], namely the APW+lo (local orbitals) method. Here the augmentation is similar to the original APW scheme but each radial wave function is computed at a fixed linearization energy to avoid the non-linear eigenvalue problem that complicated the APW method. Thus only the condition of continuity can be required and the basis functions may contain a kink at the sphere boundary.

The missing variational freedom of the radial wave functions can be recovered by adding another type of local orbitals containing a u and $\dot{u}$ term.

$$\varphi(\vec{r}) = \begin{cases} \left[a_{lm}^{\alpha,lo} u_{lm}^{\alpha}(r) + b_{lm}^{\alpha,lo} \dot{u}(r)\right] Y_{lm}(\vec{r}), & r \prec R_{\alpha} \\ 0, & r \in I \end{cases} \qquad \text{(IV-7)}$$

The local orbitals are evaluated at the same fixed energy as the corresponding APWs. The two coefficients are determined by the normalization and the condition that the local orbital has zero value at the sphere boundary. In this version, $\dot{u}$ is independent of the PWs, since it is only included for a few local orbitals and not associated with every plane wave. Recently it was demonstrated that this new scheme can reach the same accuracy as LAPW but converges faster in terms of number of PWs [5]. The highest efficiency was found for a mixed basis set in which the “physically important” l-quantum numbers are treated by APW+lo but the higher l by LAPW. It was shown in [5] that quantities such as the total energy, forces converge significantly faster with respect to the number of basis functions than with the pure LAPW procedure but reach the same values. In LAPW the force changes sign and thus the atom would move in the wrong direction for a too small basis set, whereas in the APW+lo scheme the force converges smoothly and much faster. For large systems the matrix size N can be about halved and thus the computational cost can be an order of magnitude less, since the diagonalization scales with N^3.

The new scheme combines the best features of all APW-based methods available. The LAPW converges somewhat more slowly than the APW method as has already been pointed out by Koelling and Arbman [6], since the constraint of having differentiable basis functions makes LAPWs less optimally suited to describe the orbitals inside the sphere. This justifies going back to APW but the energy-independent basis introduced in LAPW is crucial for avoiding the nonlinear eigenvalue problem and thus is kept, too. The local orbitals provide the necessary flexibility [7].

IV. 4. The full potential calculation :

The muffin tin approximation was frequently used in the 1970s and works reasonable well in highly coordinated (metallic) systems such as face centered cubic (fcc) metals. However, for covalently bonded solids, open or layered structures, Muffin tin approximation is a poor approximation and leads to serious discrepancies with experiment. In all these cases a treatment without any shape approximation is essential. Both, the potential and charge density, are expanded into lattice harmonics (inside each atomic sphere) and as a Fourier series (in the interstitial region).

$$V(\vec{r}) = \begin{cases} \sum_{lm} V_{lm} Y_{lm}(\vec{r}) & \text{inside sphere,} \\ \sum_{K} V \exp\left(i\vec{K}\vec{r}\right) & \text{outside sphere.} \end{cases} \tag{IV-8}$$

Thus their form is completely general so that such a scheme is termed full-potential calculation. The choice of sphere radii is not very critical in full potential calculations in contrast to muffin tin approximation, in which one would obtain different radii as optimum choice depending on whether one looks at the potential (maximum between two adjacent atoms) or the charge density (minimum between two adjacent atoms). Therefore in muffin tin approximation one must make a compromise but in full-potential calculations one can efficiently handle this problem.

[1] J.C. Slater, Phys. Rev. **51**, 151 (1937)

[2] J. C. Slater, Advances in Quantum Chemistry, **1**, 35 (1964).

[3] O.K. Andersen, Phys. Rev. **B** 12, 3060 (1975).

[4] E. Sjöstedt, L. Nordström, D.J. Singh, Solid State Comm. **114**, 15 (2000).

[5] G.K.H. Madsen, P. Blaha, K. Schwarz, E. Sjöstedt, L. Nordström, Phys. Rev. B **64**, 195134 (2001).

[6] D.D. Koelling, G.O. Arbman, J. Phys. F **5**, 2041 (1975).

[7] K. Schwarz, J. Solid State Chem. **176**, 3.19 (2003).

Chapter V

Results and Discussions

Abstract :

This chapter is devoted to the principle results of FP-L/APW+lo calculations performed on AlN and GaN compounds and doped with manganese. In part I, we study the structural, elastic and electronic properties of III-N compounds (AlN and GaN) at zero pressure and under hydrostatic pressure. In part II, we concentrate to study the effect of manganese (Mn) on AlN and GaN compounds and we determine the principal characteristics of diluted magnetic semiconductors AlN:Mn and GaN:Mn in their ferromagnetic phase.

V. I. 1. Numerical details

Our calculations are performed using the scalar relativistic full-potential linearized / augmented plane wave plus local orbitals (FP-L/APW+lo) [1] approach based on the density functional theory [2] within the LDA and GGA using the scheme of Perdew, Brouke and Ernzerhof [3]. We adopt the Ceperley-Alder [4] forms for exchange-correlation energy as parametrized by Perdew and Wang [5].

In the present calculations we apply the most recently version of Vienna package WIEN2k_2003 [6,7]. In this new version, the alternative base sets (APW+lo) is used inside the atomic spheres for those chemically important l-orbitals (partial waves) that are difficultly converge (outermost valence p-, d-, or f-states), or for atoms where small atomic spheres must be used [8-10]. For all the other partial waves the LAPW scheme is used.

Moreover, we employ the semirelativistic approximation (no spin orbit effects included) whereas the core levels are treated fully relativistically [11]. In particular, the Ga is considered in such as to include explicitly the semicore d electrons in the valence bands. In the following calculations, we distinguish the Al ($1s^2$ $2s^2$ $2p^6$), Ga ($1s^2$ $2s^2$ $2p^6$ $3s^2$ $3p^6$), and N ($1s^2$) inner-shell electrons from the valence electrons of Al ($3s^2$ $3p^1$), Ga ($3d^{10}$ $4s^2$ $4p^1$) and N ($2s^2$ $2p^3$) shells.

The remaining core states are self-consistently relaxed in a spherical approximation. Inside the non-overlapping spheres of muffin-tin (MT) radius (R_{MT}) around each atom, spherical harmonics expansion is used. We choose the plane wave basis set for the remaining space of the unit cell. For AlN and GaN we adopt as the MT radius, the values of 1.82, 1.8 and 1.6 Bohr for Al, Ga and N respectively. The maximum l value for the wave function expansion inside the atomic spheres was confined to l_{max}= 10. In order to achieve energy eigenvalues convergence, the wave functions in the interstitial region is expanded in plane waves with a cutoff of $R_{MT} * K_{MAX} = 8$ (where K_{MAX} is the maximum modulus for the reciprocal lattice vector, and R_{MT} is the average radius of the MT spheres). The k integration over the Brillouin zone is performed using Monkhorst and Pack [12] mesh, yielding to 10 k points in the irreducible wedge of the Brillouin zone for both zincblende and wurtzite structures. The iteration process is repeated until the calculated total energy of the crystal converges to less than 0.1 mRyd.

The ground-state structures of AlN and GaN are wurtzite, but these compounds have also been reported to stabilize in the zincblende structure (see Ref. [13]). The zincblende and wurtzite structures are schematically depicted in Figure V.I.1. For the zincblende structure, determination of the theoretical equilibrium geometry is straightforward since there is just one lattice constant a with two atoms per unit cell, one at (0, 0, 0) and the other at $(\frac{1}{4},\frac{1}{4},\frac{1}{4})$, with unit vectors $\vec{a}=\left(0,\frac{1}{2},\frac{1}{2}\right)a$, $\vec{b}=\left(\frac{1}{2},0,\frac{1}{2}\right)a$ and $\vec{c}=\left(\frac{1}{2},\frac{1}{2},0\right)a$. For wurtzite there are four atoms per hexagonal unit cell. With the unit vectors $\vec{a}=\left(\frac{1}{2},\frac{\sqrt{3}}{2},0\right)a$, $\vec{b}=\left(\frac{1}{2},-\frac{\sqrt{3}}{2},0\right)a$ and $\vec{c}=\left(0,0,\frac{c}{a}\right)a$, the positions of the atoms, in units of $\vec{a},\vec{b},\vec{c}$ are (0, 0, 0) and $(\frac{2}{3},\frac{1}{3},\frac{1}{2})$ of the first type and (0, 0, u) and $(\frac{2}{3},\frac{1}{3},$ $u+\frac{1}{2})$ for atoms of the second type, where u is the dimensionless internal parameter. The wurtzite phase experimentally observed at low pressure in these and related compounds has $u_0 \approx \frac{3}{8}$ and $c/a \approx 1.633$, which leads within experimental accuracy tetrahedral coordination at the *ideal* values $u_0 = \frac{3}{8}$ and $c/a = \sqrt{\frac{8}{3}}$, all four nearest-neighbor distances are equal and all bond angles are ideal tetrahedral angles (109.5°).

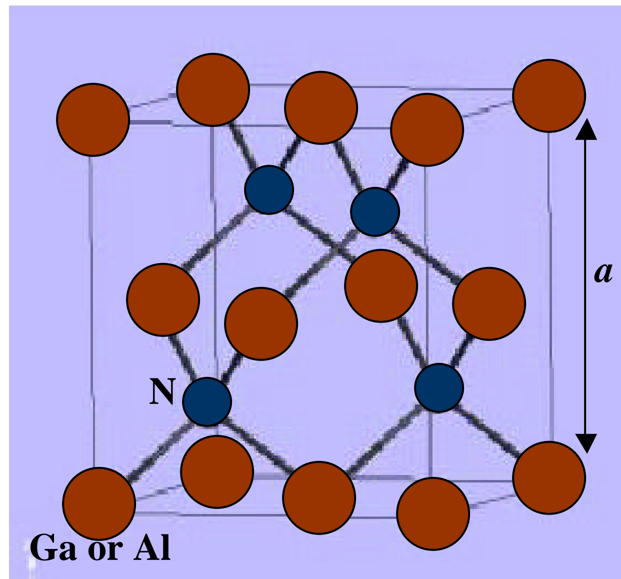

Figure V.I. 1(a). Schematic illustration of the cubic zincblende structure.

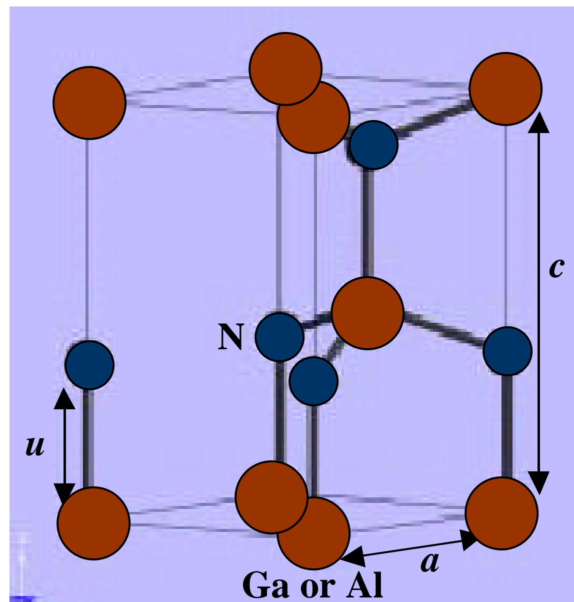

Figure V.I. 1(b). Schematic illustration of the hexagonal wurtzite structure.

V. I. 2. Structural properties

V. I. 2. 1. Zincblende phase

The structural properties in the strain-free case are obtained by a minimization of the total energy depending on the volume for AlN and GaN in the zincblende structure (see Figures V.I.2. We compute the lattice constants, bulk modulus and the pressure derivative of the bulk modulus by fitting the total energy versus volume according to the Murnaghan's equation of state [14]:

$$E(V) = E_0(V) + \frac{BV}{B^{/}(B^{/}-1)}\left[B\left(1-\frac{V_0}{V}\right)+\left(\frac{V_0}{V}\right)^{B^{/}}-1\right] \qquad \text{(V.I-1)}$$

where E_0 and V_0 are the energy and volume at equilibrium. B and $B^{/}$ are the bulk modulus and it's the pressure derivative.

In Table V.I.1 and Table V.I.2, our results of structure optimization for zincblende AlN and GaN within LDA and GGA calculations are summarized and compared with some available experimental data [15,16] and recent published calculations [17-40].

With GGA calculation for GaN, the lattice constant is found 1.4% larger than LDA calculation, whereas for AlN a difference of 2% is observed. Correspondingly, the values of the bulk modulus obtained by GGA are smaller by 8.7% (AlN) and 14% (GaN) than the LDA results. We find that LDA yields a slightly smaller lattice constant than experiment (by 0.48% and 0.6%), while that of GGA is 1% and 1.33% larger for AlN and GaN, respectively. Compared to experiment, the LDA overestimates the bulk modulus, whereas GGA underestimating it. The LDA values are therefore in significantly better agreement with experiment and it appears that GGA does not bring about significant improvement over LDA for AlN and GaN.

The calculated bulk modulus is the same as those found elsewhere [25], mainly with the well-converged pseudopotential calculations. Moreover, it has been shown few years ago [29] that anharmonic corrections due to phonon vibrational energy may considerably reduce the value of the bulk modulus, even at temperature T = 0 K. This confirms the reliability of our obtained value of bulk modulus. One should also notice that the experimental values of the bulk modulus are somehow uncertain due to the difficulty of growing high-quality single crystals of III-V nitrides.

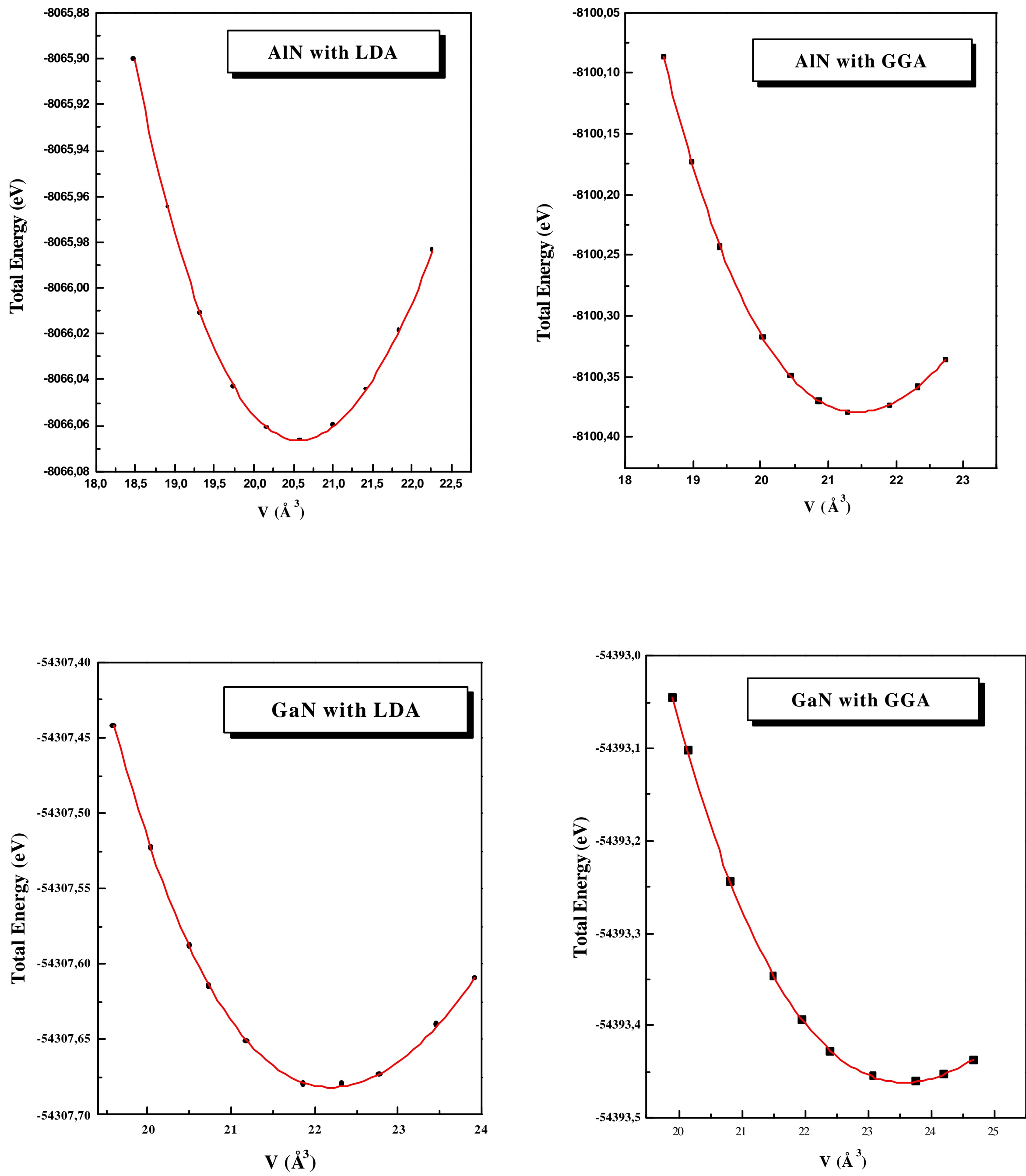

Figures. V.I.2. Total energy as a function of the volume for zincblende AlN and GaN with LDA and GGA calculations.

Table V.I.1. *Lattice constants a, bulk modulus B, and pressure derivations of the bulk modulus B' of zincblende AlN.*

	This work		Calculations		Experiment
	LDA	**GGA**	**LDA**	**GGA**	
a **(Å)**	4.349	4.409	4.31-4.376[a]	4.39-4.42[b]	4.37[c]
B **(GPa)**	211.78	193.3	213-216[a]	191[b]	-
B'	3.90	3.8	3.2-3.86[a]	3.81[b]	-

[a] Refs. [17-40], [b] Refs. [30,33,37], [c] From wurtzite structure Ref. [15]

Table V.I.2. *Lattice constants a, bulk modulus B, and pressure derivations of the bulk modulus B' of zincblende GaN.*

	This work		Calculations		Experiment
	LDA	**GGA**	**LDA**	**GGA**	
a **(Å)**	4.461	4.55	4.446-4.537[a]	4.55-4.59[b]	4.50[c]
B **(GPa)**	202	172.6	191-202[a]	156[b]	185[d]
B'	4.32	4.3	3.9-4.14[a]	4.25[b]	-

[a] Refs. [17-40], [b] Refs. [30,33,37], [c] Ref. [15],

[d] Ref. [16], The Bulk modulus may be derived from the elastic constants as $B = (C_{11} + 2C_{12})/3$, these values are obtained from the experimental hexagonal elastic constants [15].

V. I. 2. 2. Wurtzite phase

Under normal conditions the AlN and GaN compounds crystallize in the wurtzite structure, although it has proved possible to grow a zincblende modification using epitaxial techniques [41,42]. The wurtzite form is a hexagonal structure (with two formula units per unit cell), which can be described by three structure parameters: a, c and an internal parameter u. To determine the equilibrium geometry of the wurtzite phase, we optimize the independent parameters V (volume of the unit cell), c/a ratio and u as follows: In the first step, we assume the ideal wurtzite structure and determine the equilibrium volume by varying the lattice constant a. Then, keeping the equilibrium volume fixed and u, the c/a ratio is varied to find the optimum value. At new c/a ratio we lance again vary the lattice constant a, to determine the new equilibrium volume. Then, having found c/a and V, vary the internal parameter u to minimize the total energy.

In Figures V.I.3 and V.I.4**,** we plot the total energy versus volumes, the c/a ratios and the internal structural parameter. The LDA and GGA values of c/a ratios are identical and equal to 1.6 for AlN and 1.628 for GaN. This value is in an excellent agreement with the experimental data [15] and other theoretical values [17-40,43,44]. The optimal value for $\underline{u}$, u_{eq}, is of 0.38 for AlN and 0.375 for GaN, which is identical to the experimental results of Ref. [15], and it is also V-independent. The calculated structural parameters of wurtzite AlN and GaN are listed in Table V.I.3 and Table V.I.4.

Our lattice constants as obtained using the GGA are about 1.4% and 2% larger than the LDA values for AlN and GaN respectively. With respect to experiment, LDA lattice constants is smaller by 0.58% and 1%, while that of GGA is 0.83% and 1% larger for AlN and GaN, respectively. The bulk modulus are obtained using GGA are smaller about 10.3% and 19% for AlN and GaN compared with experimental values. The LDA values are also in wurtzite structure therefore in significantly better agreement with experiment and it appears that GGA does not bring about significant improvement over LDA for AlN and GaN.

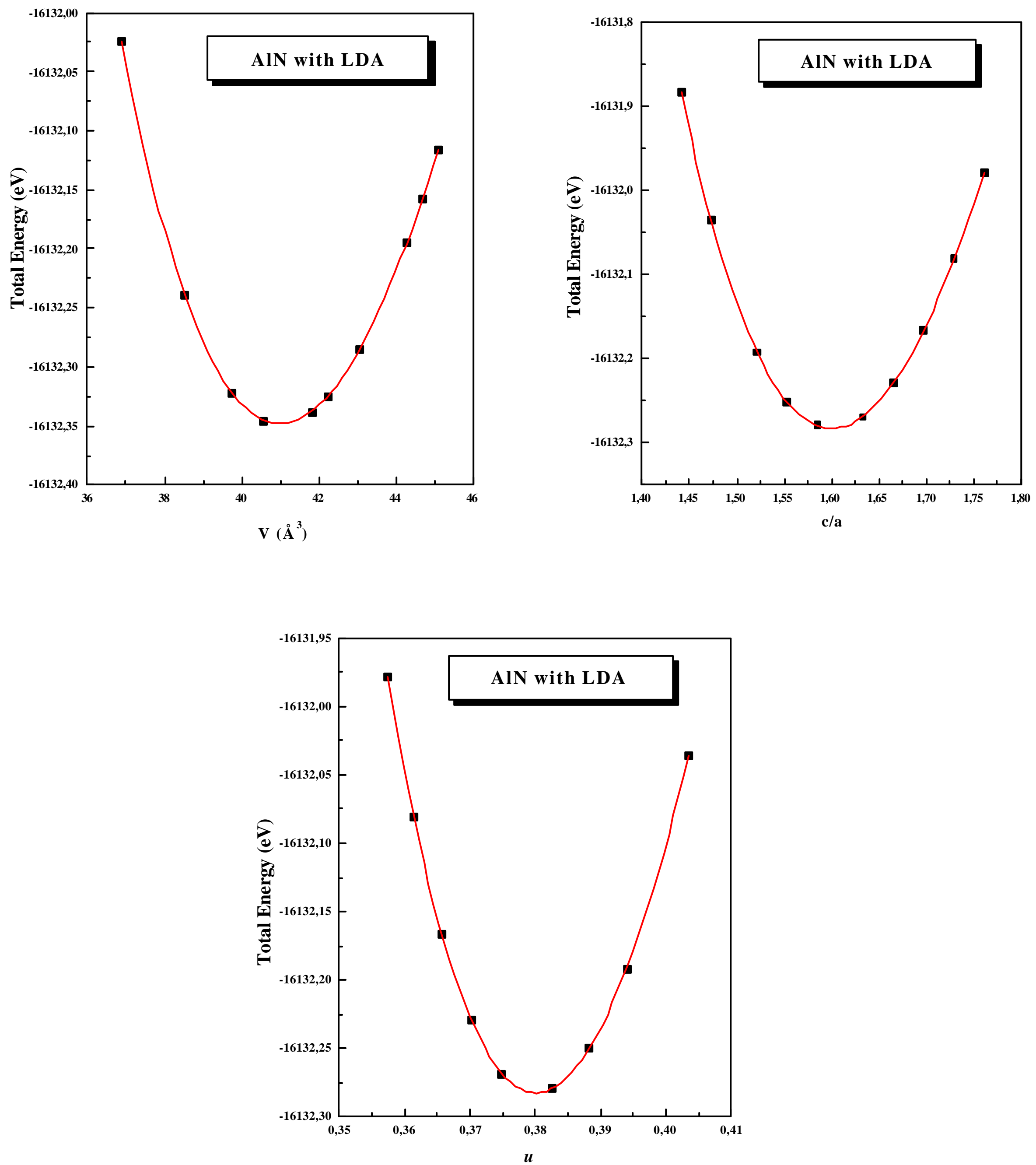

Figure V.I.3(a). Total energy as a function of the volume, c/a ratio and u for wurtzite AlN with LDA calculation.

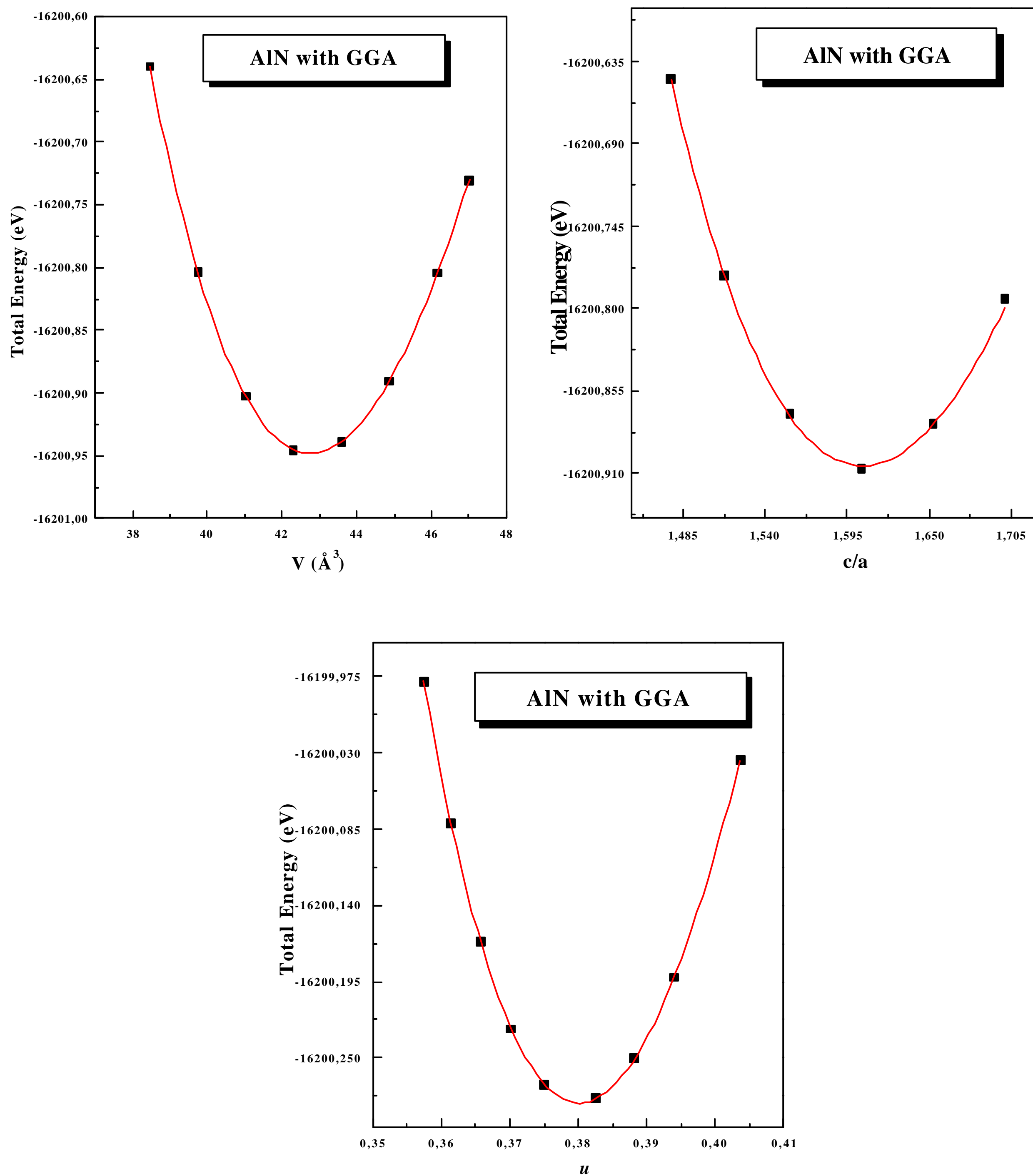

Figure V.I.3(b). Total energy as a function of the volume, c/a ratio and u for wurtzite AlN with GGA calculation.

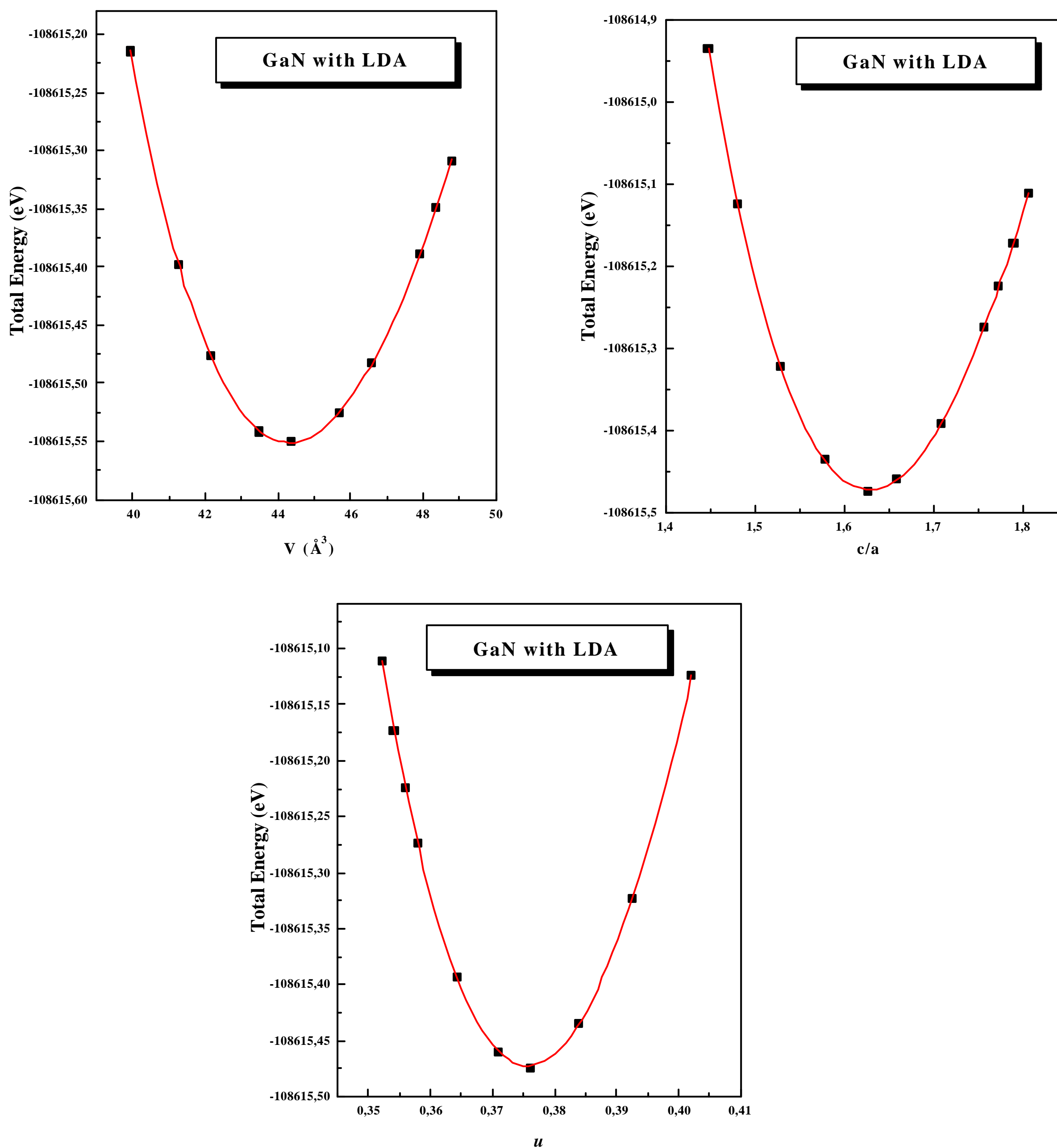

Figure V.I.4(a). Total energy as a function of the volume, c/a ratio and u for wurtzite GaN with LDA calculation.

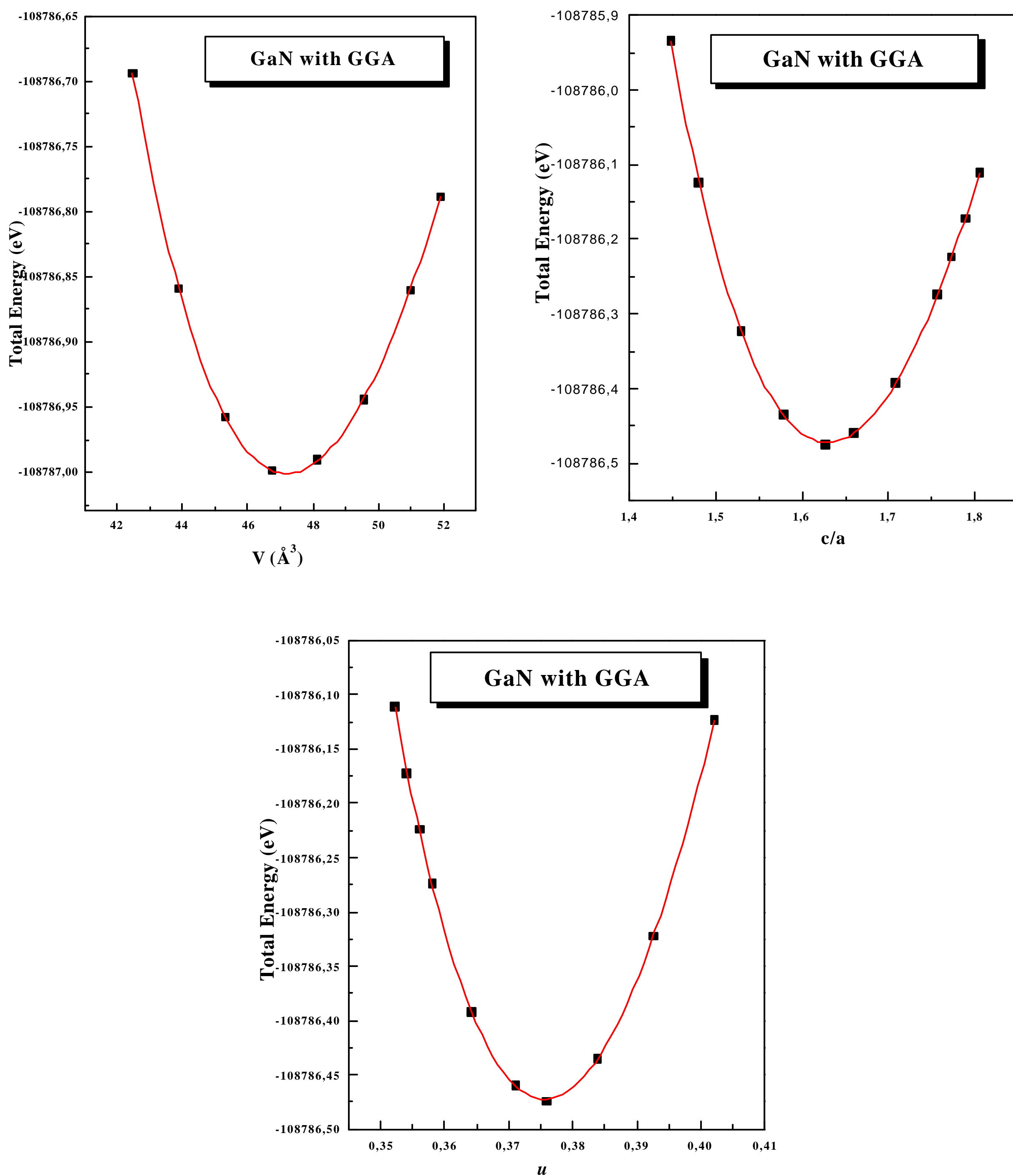

Figure V.I.4(b). Total energy as a function of the volume, c/a ratio and u for wurtzite GaN with GGA calculation.

Table V.I.3. *Lattice constants a and c, c/a, internal parameter u, bulk modulus B, and derivative B' of wurtzite AlN.*

	This work		Calculations		Experiment
	LDA	**GGA**	**LDA**	**GGA**	
a **(Å)**	3.093	3.137	3.057-4.114[a]	3.113-3.135[b]	3.111[c]
c **(Å)**	4.952	5.023	4.943-5.046[a]	5.022-5.041[b]	4.978[c]
c/a	1.601	1.601	1.604-1.619[a]	1.602-1.6193[b]	1.601[c]
u	0.3801	0.3801	0.380-0.383[a]	0.7898-0.381[b]	0.385[c]
B **(GPa)**	212.16	192.35	195-215[a]	192[b]	185-212[d]
B'	3.878	3.757	3.63-3.82[a]	3.96[b]	5.7-6.3[d]

[a] Refs. [21-38,44,49], [b] Refs. [30,33], [c] Refs. [13,15], [d] Refs. [13,46]

Table V.I.4. *Lattice constants a and c, c/a, internal parameter u, bulk modulus B, and derivative B' of wurtzite GaN.*

	This work		Calculations		Experiment
	LDA	**GGA**	**LDA**	**GGA**	
a **(Å)**	3.157	3.224	3.095-3.193[a]	3.245[b]	3.18-3.192[c]
c **(Å)**	5.14	5.25	5.0-5.228[a]	5.296	5.166-5.185[c]
c/a	1.628	1.628	1.622-1.639[a]	1.632	1.624-1.627[c]
u	0.3756	0.3757	0.375-0.378[a]	0.3762	0.375-0.377[c]
B **(GPa)**	203.96	171.2	195-213[a]	172[b]	188-220[d]
B'	4.565	4.5516	4.2-4.5[a]	5.11[b]	3.2-4.3[d]

[a] Refs. [21-38,43,44,49], [b] Refs. [30,33], [c] Refs. [13,15], [d] Refs. [13,48,51,52]

V. I. 2. 3. Rocksalt phase

The structure of the tetrahedral compounds is determined by the competition between the energy gain obtained by formation of sp^3 bonds (as in the zincblende or wurtzite, rocksalt structure) and the gain in Madelung energy due to a larger coordination number. The zincblende (or wurtzite) structure is four-fold coordinated, and the rocksalt is six-fold coordinated. The more ionic compounds will prefer therefore rocksalt to zincblende (or wurtzite) structure, and according to the Phillips-Van Vechten theory [45] a critical ionicity, f_c = 0,785, exists such that compounds with ionicities larger than this crystallize in the six-fold coordinated structure, whereas the others are stable in the tetrahedrally-bonded structures, zincblende or wurtzite.

In our total-energy calculations we have examined the high-pressure rocksalt structure of AlN and GaN compounds. Figures V.I.5 show the fitted total energy versus volume curves of AlN and GaN compounds. In Table V.I.5 and Table V.I.6, the results for the calculated structural parameters within LDA and GGA calculations are given and compared with available experimental data [46-48] and theoretical works [43,49,50]. We find that our lattice constants obtained using GGA are 1.5% and 1.91% larger than those obtained using LDA for AlN and GaN, respectively. The bulk modulus obtained using GGA is about 8.9% smaller for AlN and 15.33 % smaller for GaN. We notice that the structural properties determined with LDA and GGA calculations of rocksalt AlN and GaN exhibit a similar conclusion mentioned in the case of zincblende and wurtzite phase.

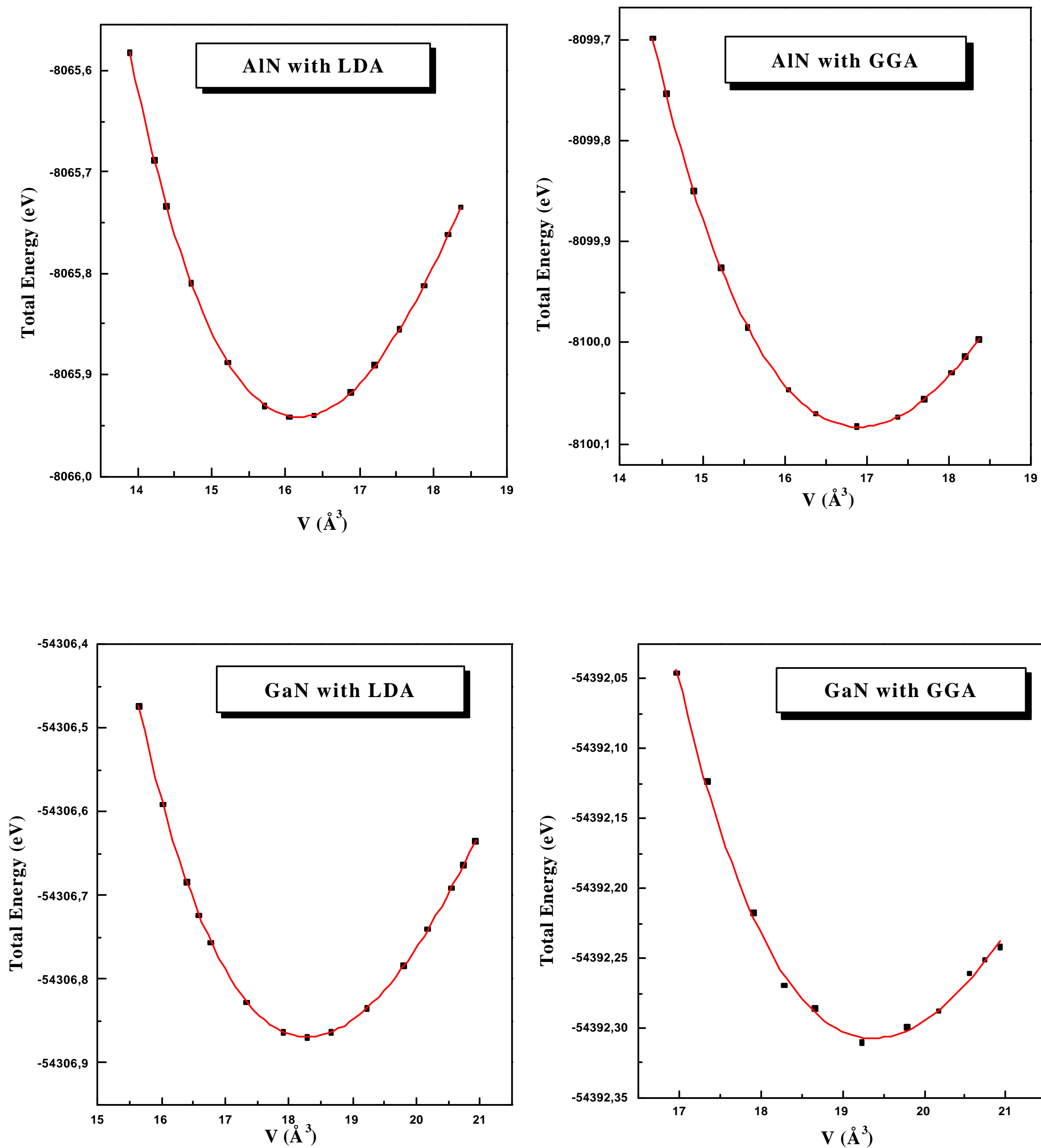

Figures V.I.5. Total energy as a function of the volume for rocksalt AlN and GaN with LDA and GGA calculation.

Table V.I.5. *Lattice constants a, bulk modulus B, and pressure derivations of the bulk modulus B' of rocksalt AlN.*

	This work		Calculations		Experiment
	LDA	**GGA**	**LDA**	**GGA**	
a **(Å)**	4.014	4.074	3.978[a]	-	4.045[b]
B **(GPa)**	276.6	252	272[a]	-	221[c]
B'	3.998	3.901	3.8[a]	-	4.8[c]

[a] Ref. [49], [b] Ref. [55] [c] Ref. [46].

Table V.I.6. *Lattice constants a, bulk modulus B, and pressure derivations of the bulk modulus B' of rocksalt GaN.*

	This work		Calculations		Experiment
	LDA	**GGA**	**LDA**	**GGA**	
a **(Å)**	4.183	4.263	4.185-4.24[b]	4.271[b]	-
B **(GPa)**	249.2	211	235-251[b]	211.6[b]	248[d]
B'	4.436	5.415	3-4.71[b]	4.50[b]	-

[a] Refs. [43,49,52] [b] Ref. [43], Ref. [48],.

V. I. 2. 4. The relative stability and phase transitions:

The wurtzite AlN and GaN are known to transform under high-pressure to the rocksalt (RS) structure. In spite of several experimental and theoretical investigations, the transition pressure, p_t, of the wurtzite to rocksalt transition is still a controversial issue (for a review see Ref. [3]), and so does the compressibility (or bulk modulus (B_{eq})) of WZ -AlN and -GaN. The first evidence of a transition of GaN under high pressure to an unknown crystal structure was provided by the X-ray absorption spectroscopy (XAS) measurements of Perlin et al. [51,52], at about 47 GPa. For AlN, the WZ to RS transition has been reported to occur at 22.9 GPa by Ueno et al [53]. Munoz and Kunc [54] have predicted the

unknown high-pressure structure to be the RS phase, using first-principles pseudopotential planewave (PP-PW) calculations. This prediction of GaN has been confirmed by the X-ray diffraction investigations of H. Xia et al. [48] and Ueno et al. [53], which gave values for p_t of 37 and 52.2 GPa, respectively. For AlN, the prediction values are reported by H. Vollstädt et al [55] and Q. Xia et al. [46], which gave values for p_t of 14-16.6 and 14-20 GPa, respectively. One should note that the above values for p_t were obtained upon pressure increase. The discrepancies between the above experimental results for p_t have been attributed to the sensitivity of the techniques used, as well as to the nature of the samples (powder [48,53] versus single crystal [51,52]. On the other hand, full-potential LMTO calculations [56] gave a value of 38.2 GPa, for GaN the ZB to RS transition, in accord with the experimental result of Refs. [51,52].

Figures V.I.6 show the fitted E_{tot} versus V curves of the three phases of AlN and GaN considered, calculated by using LDA and GGA calculations. The important features to note from those figures are the difference between the equilibrium E_{tot} of the WZ and ZB phases is smaller (the LDA and GGA results are of (0.1077 for AlN and 0.03901eV for GaN) and (0.09464 for AlN and 0.09354eV for GaN), respectively). This is expected, since the ZB and WZ phases have local tetrahedral bonding and they only differ in the second-nearest neighbors. This also explains the epitaxial growth of GaN in the WZ or ZB forms, depending on the substrate [57].

The p_{t} of the WZ to RS and ZB to RS transitions of AlN and GaN are determined from the constraint of equal static lattice enthalpy. The results for p_{t} obtained are listed in Table V.I.7, compared with other available theoretical results and experimental data. The present results agree with the theoretical values and experimental data. Our results is similarity between the WZ and ZB and show that the gradient corrections to the LDA (included via GGA) have very small effects on p_{t} of AlN and GaN

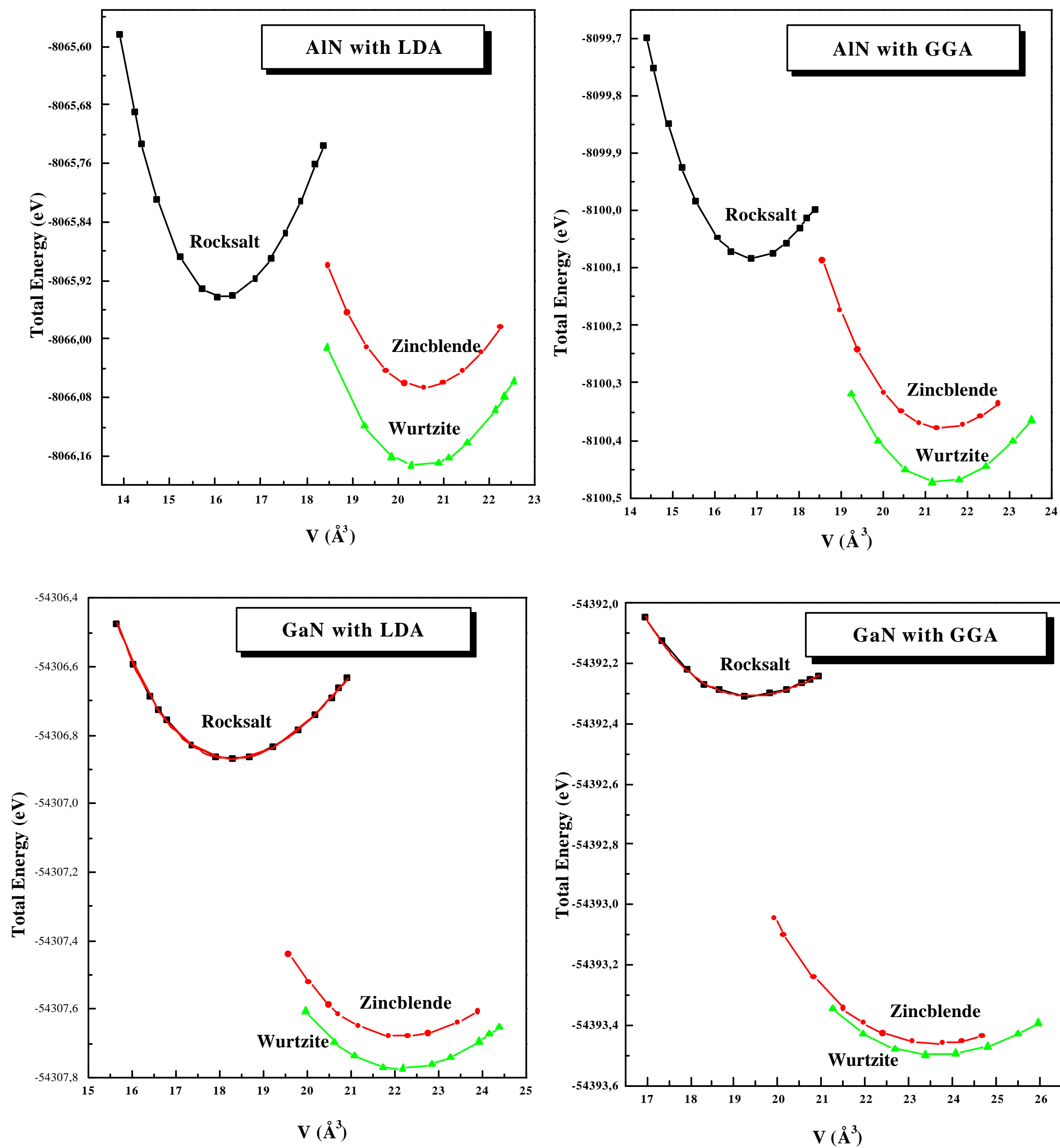

Figure V.I.6. Total energy as a function of the volume for zincblende, wurtzite and rocksalt AlN and GaN with LDA and GGA calculation.

Table V.I.7. *Transition pressures (p_t) for AlN and GaN.*

		This work		Calculations		Experiment
		LDA	**GGA**	**LDA**	**GGA**	
AlN	***ZB®RS***	4.0	5.3	7.1[a]	-	-
	WZ®RS	8.2	9.5	9.1[a], 12.9[b], 16.6[c]	-	14-16.6[f], 22.9[g], 12.9-16[h]
GaN	***ZB®RS***	33.2	35.5	38.15[d], 42.6[d], 53.80[e], 38.21[e], 42.9[a]	40.80[d]	-
	WZ®RS	34.1	36.2	42.9[a], 38.10[d], 51.8[c], 50[e], 55[b], 56[e]	42.30[d]	47-50[i], 37[j], 52[g]

[a] Ref. [49], [b] Ref. [69], [c] Ref. [22], [d] Ref. [43], [e] Ref. [52], [f] Ref. [55], [g] Ref. [53], [h] Ref. [46], [i] Ref. [51,52], [j] Ref. [48]

V. I. 3. Electronic properties

V. I. 3. 1. Band structures

V. I. 3. 1. 1. AlN compound

The electronic band structures of zincblende and wurtzite AlN along symmetry lines are displayed in Figures V.I.7 for LDA and GGA calculations. The calculated band energies at high-symmetry points are given in Table V.I.8. The band structures are calculated at the appropriate theoretical equilibrium lattice constants for LDA and GGA, respectively. Comparing LDA and GGA calculations in the zincblende structure, we see that the band structures are very similar, except that the bandgap at Γ point for the GGA result is about 0.39 eV (~9%) smaller than LDA result. The conduction bands in GGA calculation are shifted down slightly in energy, but this shift is not constant and depends on the *k* point and energy. Slight differences are also seen in valence bands: in this case GGA bands lie higher in energy than those of LDA, leading to slightly reduced bandwidths. The difference observed between LDA and GGA for band structure in zincblende phase (see Figure V.I.7(a)), is primarily due to the larger lattice constant obtained using GGA compared to LDA. If instead, the experimental lattice constant is used, the calculated bandgap for AlN in zincblende structure is the same to within 0.02 eV for LDA and GGA.

The band structure for AlN in the wurtzite phase exhibits a qualitatively similar behavior (see Figure V.I. 7(b)): the direct bandgap for GGA result is found to be 0.49eV (10%) smaller than LDA result.

The zero-energy reference is the valence-band maximum. It occurs at the Γ point, whereas the conduction-band minimum occurs at the X point. Therefore, the bandgap of zincblende AlN is Γ-X indirect and no semicore d bands are involved. Thus, we obtain an indirect bandgap of 3.211 eV and 3.304 eV for LDA and GGA, respectively, in good agreement with other predictions calculations [23,27,28,33,38,58,59] (see Table V.I.8 for comparison).

In wurtzite AlN, the bandgap is 4.3 eV and 3.30 eV for LDA and GGA, respectively, and direct at Γ point; this is in close agreement with the results of Wright and Nelson [27], Vogel *et al* [28], Pugh *et al* [59] and Rubio *et al* [23], who used plane-wave pseudopotential total-energy calculations in the LDA approximation. The value of experimental energy gap of WZ-AlN determine by Berger [60] is found about 6.28 eV.

Thus our LDA and GGA underestimate the bandgap by 1.98 eV (~30%). The total valence bandwidths are 14.8 eV for ZB-AlN and 15.12 eV for WZ-AlN.

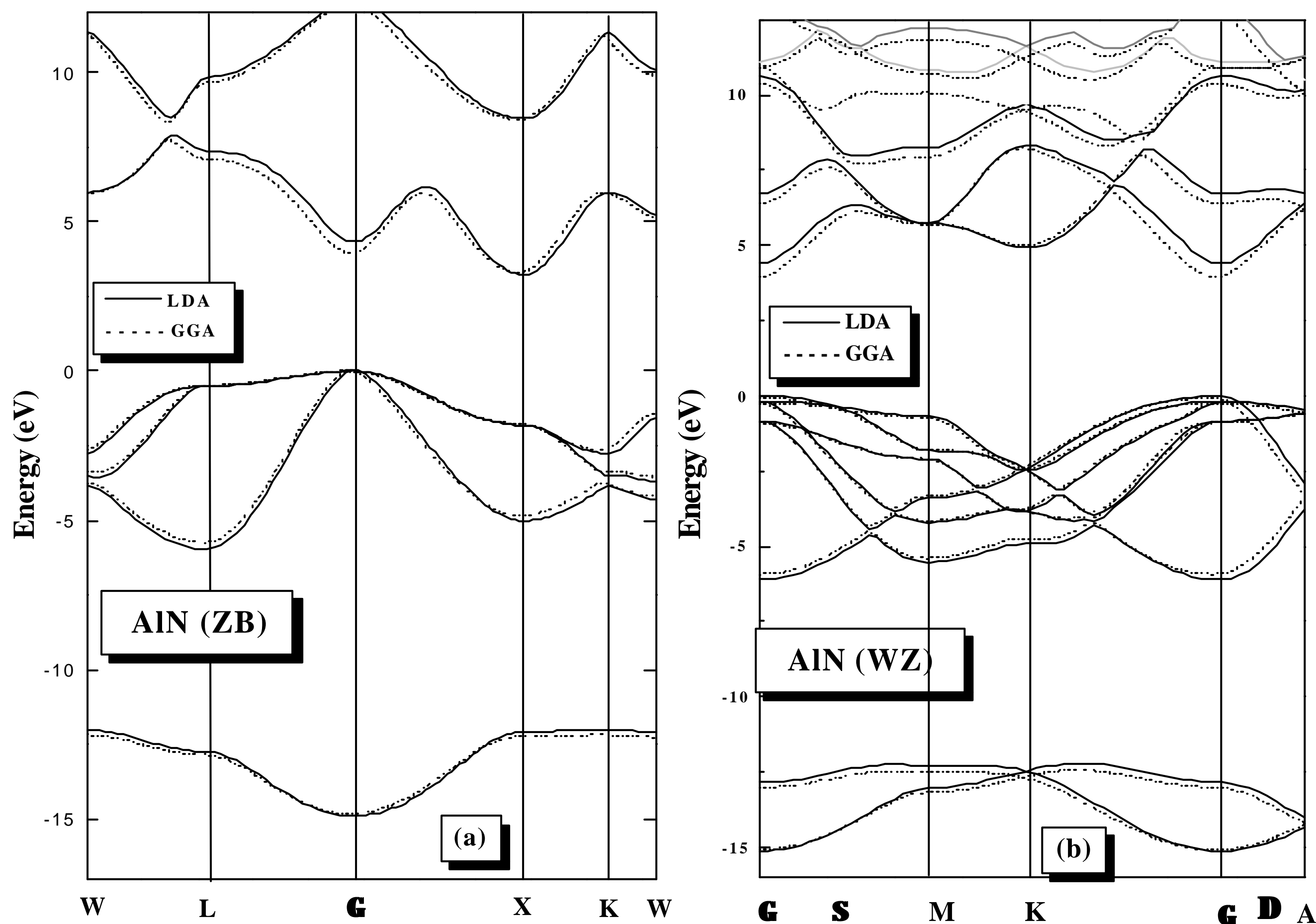

Figure V.I.7. LDA and GGA Band structures of AlN along the principle high-symmetry directions in the brillouin zone in (a) zincblende and (b) wurtzite phases. The energy zero is taken at the valence band maximum.

Table V.I.8. *Calculated bandgaps, antisymmetric gap (E_{asy}) upper-valence bandwidth (UVBW) and total valence bandwidth (TVBW) for wurtzite and zincblende structures of AlN compared to other theoretical calculations and experiments. All energies are in eV.*

	This work		Calculations	Experiment
	LDA	GGA		
Wurtzite				
$E_g(\Gamma_1^v - \Gamma_1^c)$	4.395	4.027	3.9[a], 5.8[a], 4.41[b], 4.2[c], 4.74[d], 4.3[e], 5.47[g]	6.28[h], 6.3[i]
$E_g(\Gamma_1^v - K_1^c)$	4.994	5.072	4.36[j], 5.44[k]	-
$E_g(\Gamma_1^v - M_1^c)$	5.811	5.761	5.22[j], 5.17[k]	-
$E_g(\Gamma_1^v - A_1^c)$	6.651	6.278	4.59[k]	-
E_{asy}	6.75	5.33	7.7[a], (6.74, 6.86)[g]	-
UVBW	6.12	5.866	6.9[a], 6.0[b] (6.28, 5.93)[g]	6.0[h]
TVBW	15.13	15.01	17.40[a], (15.64, 15.32)[g]	16.0[h]
Zincblende				
$E_g(\Gamma_{15}^v - \Gamma_1^c)$	4.325	3.945	4.35[b], 4.3[e], 4.75[c], 4.2[f],	-
$E_g(\Gamma_{15}^v - X_1^c)$	3.211	3.304	3.2[a], 3.2[c], 3.1[e], 4.9[a], 5.2[c]	-
$E_g(\Gamma_{15}^v - L_1^c)$	7.383	7.12	-	-
E_{asy}	7.07	7.42	7.6[a]	-
UVBW	5.98	5.74	5.9[d], 6.0[a]	-
TVBW	14.92	14.824	15.1[a]	-

[a] Ref. [23], [b] Ref. [25], [c] Ref. [28], [d] Ref. [33], [e] Ref. [59], [f] Ref. [58], [g] ref [62], [h] Ref [60], [i] Ref [41], [j] Ref [70], [k] Ref [22]

V. I. 3. 1. 2. GaN compound

The electron energy band structures of zincblende and wurtzite GaN at normal pressure along principal symmetry points in the Brillouin zone are shown in Figures V.I.8 for LDA and GGA calculations. Principle features of the calculated band structure such as bandgaps are given in Table V.I.9. As in the case of AlN, the band structures look rather similar. The bandgap is about 0.40 eV (~21%) smaller for GGA as compared to LDA. Similar results are obtained for the wurtzite structure: GGA yields a bandgap approximately 0.41eV (~19.3%) smaller than LDA. This, as mentioned earlier, can be primarily attributed to the larger GGA lattice constant. However, the upper valence bandwidth is improved by the use of GGA (the LDA and GGA values for WZ-GaN are 7.35 and 6.855 eV, respectively, compared to the experimental result of 7.4 eV [63]).

The most prominent features of the calculated band structures (bandgaps, antisymmetric gap (E_{asy}) and bandwidths) of ZB-GaN and WZ-GaN are listed in Table V.I.9 for LDA and GGA as well as other calculations [23,27,28,33,38,58,59] and available experimental [15] data. In GaN there is a considerable hybridization of the N p orbitals with the Ga 3d orbitals which reduces the gap. The interaction between the N p and the occupied Ga d states results in a level repulsion, moving the valence-band maximum upwards. This p-d coupling tends to reduce the bandgaps as it is known for nitride compounds [18,58,61]. The p-d coupling increases with small p-d energy differences and large overlap between the p-d orbitals. In WZ-GaN, the band gap at Γ is 2.1 and 1.691 eV for LDA and GGA, respectively. This is in close agreement with the results of Rubio et al. [23], Wright et al. [27], Vogel et al. [28], and Pugh et al. [59] who used plane-wave pseudopotential total energy calculations in the LDA approximation (see Table V.I.9 for comparison). The bandgap of GaN is found to be direct at Γ point and equal to 1.93 eV and 1.521 eV for LDA and GGA, respectively, which agree well with *ab initio* calculations [23,27,33,59]. Our bandgaps values are underestimated about 41% compared to experimental one.

The results of other approaches beyond LDA and/or GGA, as Hartree-Fock [62], GW quasiparticle [23] and self-interaction as well as relaxation correction pseudopotential (SIRC-PP) [28] calculations are also listed for comparison. Only GW quasiparticle and SIRC-PP calculation of Rubio *et al* [23] and Vogl *et al* [28], respectively, yield gap

energies in reasonable agreement with experiment. However there is an interesting agreement between LDA and/or GGA and GW results for the valence bandwidths. Furthermore it is widely accepted that the LDA and/or GGA electronic band structures agree qualitatively with experiments work as concerns the ordering of the energy levels and the shape of the bands.

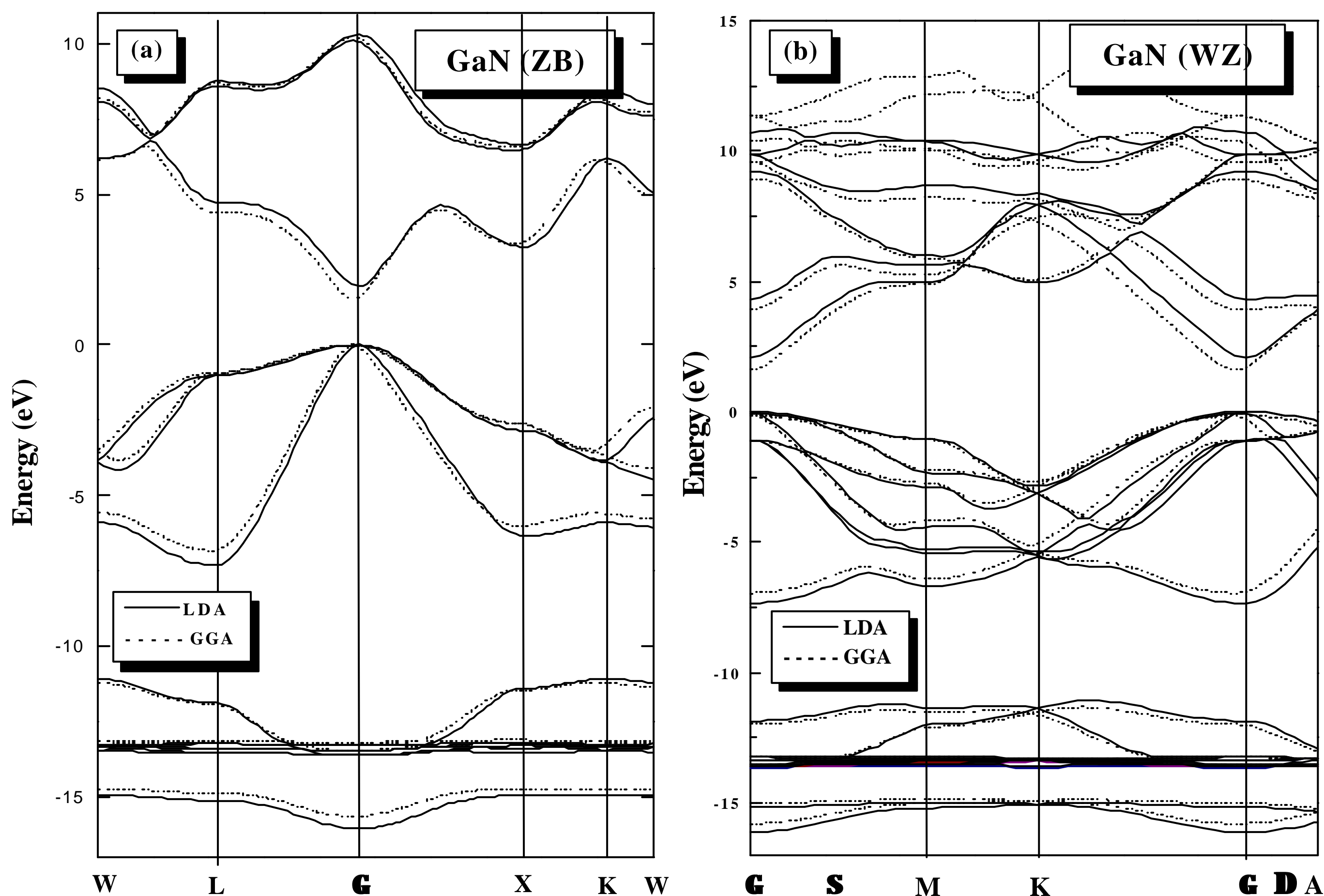

Figures V.I.8. LDA and GGA Band structures of GaN along the principle high-symmetry directions in the brillouin zone in (a) zincblende and (b) wurtzite phases, the Ga 3d treated as valence states. The energy zero is taken at the valence band maximum.

Table V.I.9. *Calculated bandgaps, antisymmetric gap (Easy) upper-valence bandwidth (UVBW) and total valence bandwidth (TVBW) for wurtzite and zincblende of GaN structures compared to other theoretical calculations a nd experiments. All energies are in eV.*

	This work		Calculations	Experiment
	LDA	**GGA**		
Wurtzite				
$E_g(\Gamma^v - \Gamma^c)$	2.10	1.691	2.3[a], 1.9[b], 3.51[b], 1.76[c], 1.7[d], 4.0[d], 2.04[e], 2.75[f]	3.474-3.507[g]
$E_g(\Gamma_1^v - K_1^c)$	4.975	4.871	4.57[k], 5.44[h]	-
$E_g(\Gamma_1^v - M_1^c)$	4.966	5.075	4.63[k], 5.09[h]	-
$E_g(\Gamma_1^v - A_1^c)$	4.363	3.933	4.28[k], 4.59[h]	-
E_{asy}	5.1	5.01	5.4[a]	
UVBW	7.35	6.85	7.4[a], 7.3[b], 7.1[b]	7.4[h]
TVBW	16.11	15.7	16.3[a]	-
Zincblende				
$E_g(\Gamma^v - \Gamma^c)$	1.93	1.521	3.1[a], 1.6[b,c], 1.28[c], 3.8[b], 1.9[d], 1.89[i]	3.3[f], 3.29-3.35[g], 3.2[j]
$E_g(\Gamma^v - X^c)$	3.25	3.411	-	-
$E_g(\Gamma^v - L^c)$	4.73	4.416	-	-
E_{asy}	5.09	5.6	5.6[a]	-
UVBW	7.33	7.062	7.4[a], 7.3[b]	-
TVBW	16.77	13.423	16.3[a], 16.3[b]	-

[a] Ref. [23], [b] Ref. [28], [c] Ref. [33], [d] Ref. [59], [e] ref [24], [f] Ref. [58], [g] Ref [38], [h] Ref [63], [i] Ref. [25], [j] Ref [15], [k]Ref. [70], [j] Ref [22]

V. I. 3. 2. Densities of states:

An essential ingredient in determining the electronic properties of solids is the energy distribution of the valence and conduction bands electrons [64]. For example, analysis of dielectric functions, transport properties, photoemission spectra of solids requires knowledge of the electronic density of states (DOS). Theoretical quantities such as total electronic energy of solid, the position of Fermi level, and tunneling probabilities of electrons call for detailed calculations of electronic density of state.

V. I. 3. 2. 1. AlN compound

In order to check the accuracy of our band structures results; we applied the tetrahedron method [65] to calculate DOS. In this case we present the calculated total and partial DOS of AlN in zincblende and wurtzite structures. The DOS is computed using a mesh of 91 and 140 k points in the IBZ for ZB and WZ structures, respectively.

Figures V.I.9 show the total, partial and the projected DOS integrated over the atoms for both ZB and WZ –AlN. While not much difference is expected between DOSs obtained for the two structures for the occupied states (valence bands), significant discrepancies are obvious for the unoccupied levels (conduction bands). In particular, the total DOS for ZB-AlN has conduction band DOSs that are shifted toward lower energies as compared to that of WZ-AlN. For both ZB-AlN and WZ-AlN, the total DOS presents three regions: the lower part of the valence bands is dominated by N 2*s* states, and the upper part by N 2*p* and Al 3*p* states. The Al 3s states contribute to the lower valence bands. The first conduction band in Γ is predominantly of Al 3*s* character. In Figures V.I.10, we show the angular-momentum decomposition of the atom-projected DOS of both ZB-AlN and WZ-AlN, which are used to analyse the orbital character of different states. The strong hybridization of Al 3s and Al 3p with N 2p-like states can be readily visualized in Figures V.I.10.

From Figures V.I.9, one can see that the 2*s* band of nitrogen between –11.98 and -14.92 eV for ZB-AlN and between -12.11 and –15.12 eV for WZ-AlN is distinct and has very little mixing with other states. In the case of AlN the nitrogen 2s band is wider and lower in energy. The large direct bandgap (Γ^{15v}–Γ^{1c}) in ZB and (Γ^{1v}–Γ^{1c}) in WB structures of AlN is due to the Al 3*s* and N 2*s* orbital interaction, which forms the lower-energy bonding state (Γ^{1v}) and the anti-bonding state (Γ^{1c}). The bonding and anti-bonding states

are lowered and pushed respectively, relative to the N 2s and Al 3s orbital energies, by the same amount of s–s interaction energy in both structures ZB and WZ. The resulting direct bandgap must be the same for both ZB-AlN and WZ-AlN (see Table V.I.8 for comparison).

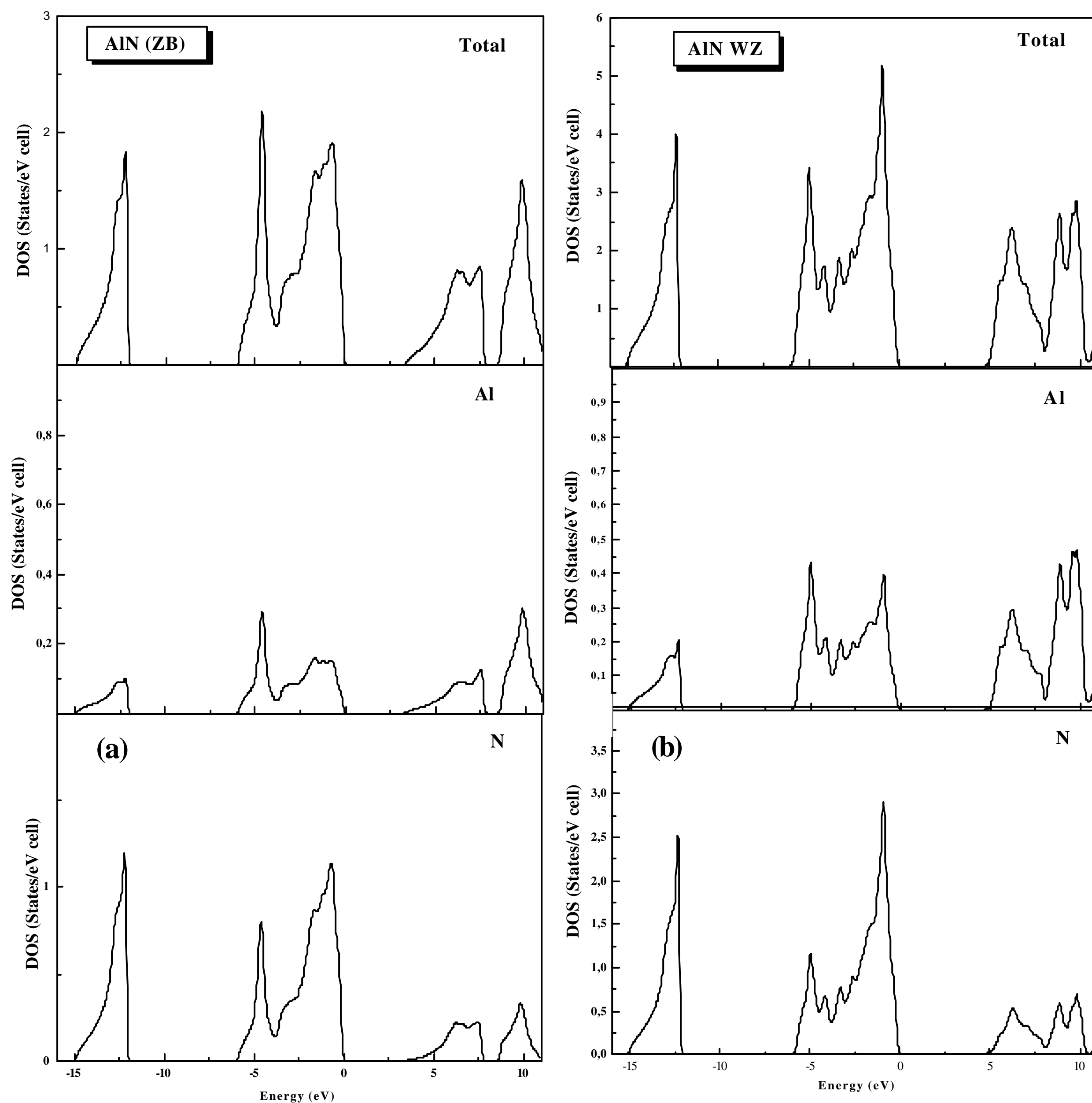

Figure V.I. 9. Calculated total and partial density of states of AlN in (a) zincblende and (b) wurtzite.

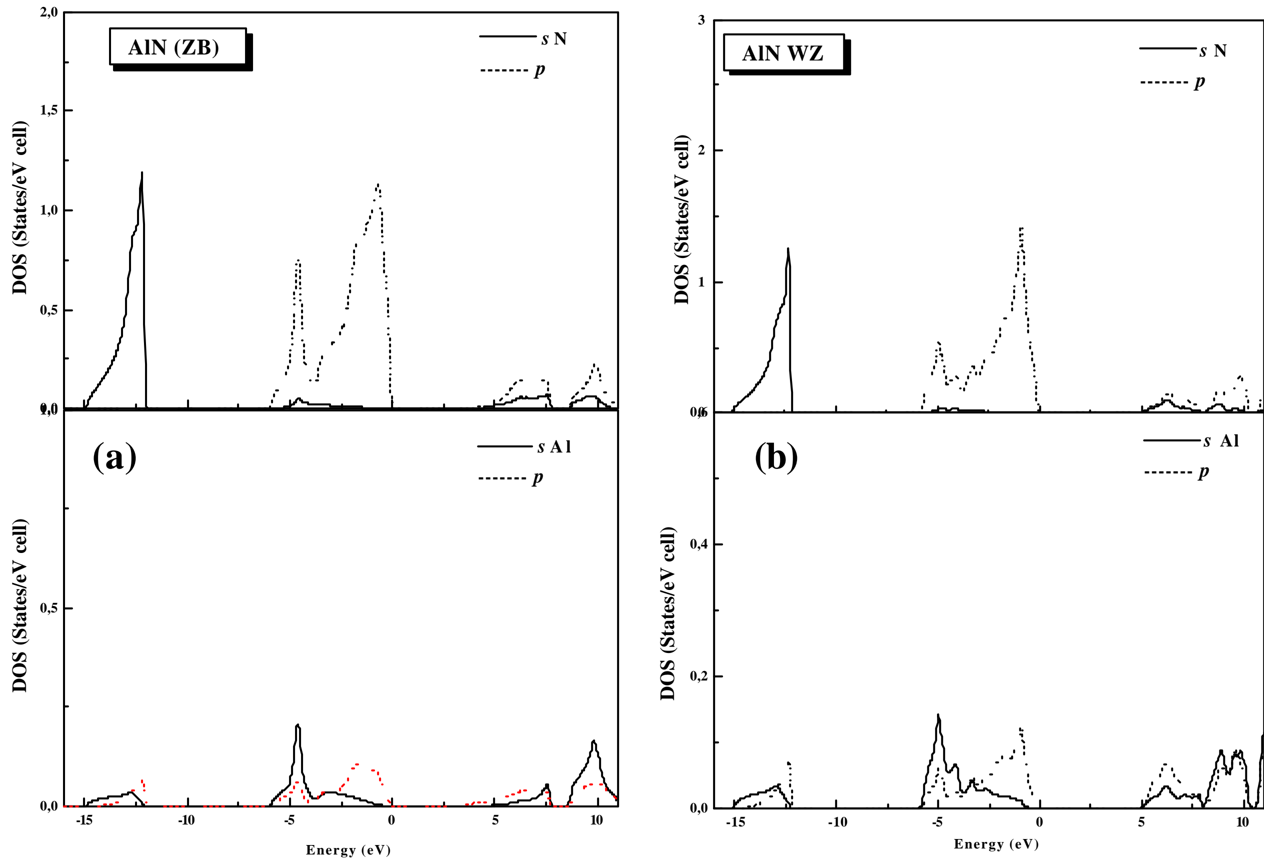

Figure V.I. 10. The angular-momentum decomposition of the atom-projected densities of states in (a) ZB-AlN and (b) WZ-AlN.

V. I. 3. 2. 1. GaN compound

In this section, we present the calculated total and partial DOS of GaN in wurtzite and zincblende structures. Figures V.I.11 show the total, partial and the projected density of states (DOS) integrated over the atoms for both wurtzite and zincblende GaN, respectively. While not much difference is expected between DOS obtained for the two structures, for the occupied states (valence bands), significant discrepancies are obvious for the unoccupied levels (conduction bands). In particular, the total DOS for ZB-GaN, has conduction-band DOS that are shifted towards lower energies as compared to that of WZ-GaN. For both ZB-GaN and WZ-GaN, the total DOS presents three regions, the lower part of the valence bands are dominated by N 2s states, and the upper part by N 2p and Ga 4p states. The Ga 4s states contribute to the lowest valence bands. The first conduction band in Γ is predominantly of Ga 4s character.

The Figures V.I.12 represent the atom-projected DOS of both ZB-GaN and WZ-GaN. We see from those figures, that most of the d character resides on the Ga sites, while that of the s character still comes from N. Furthermore, the 3d electrons in the Ga atom are more resonant with the 2s electrons of N.

The large direct band gap in both ZB and WZ structure of GaN is due to the Ga 4s and N 2s orbitals interaction which forms the lower-energy bonding state (Γ^{1v}) and the antibonding state (Γ^{1c}). The bonding and anti-bonding states are lowered and pushed respectively, relative to the N 2s and Ga 4s orbital energies by the same amount of s–s interaction energy in both structures WZ and ZB. The resulting direct band gap must be the same for both ZB-GaN and WZ-GaN (see Table V.I.9 for comparison).

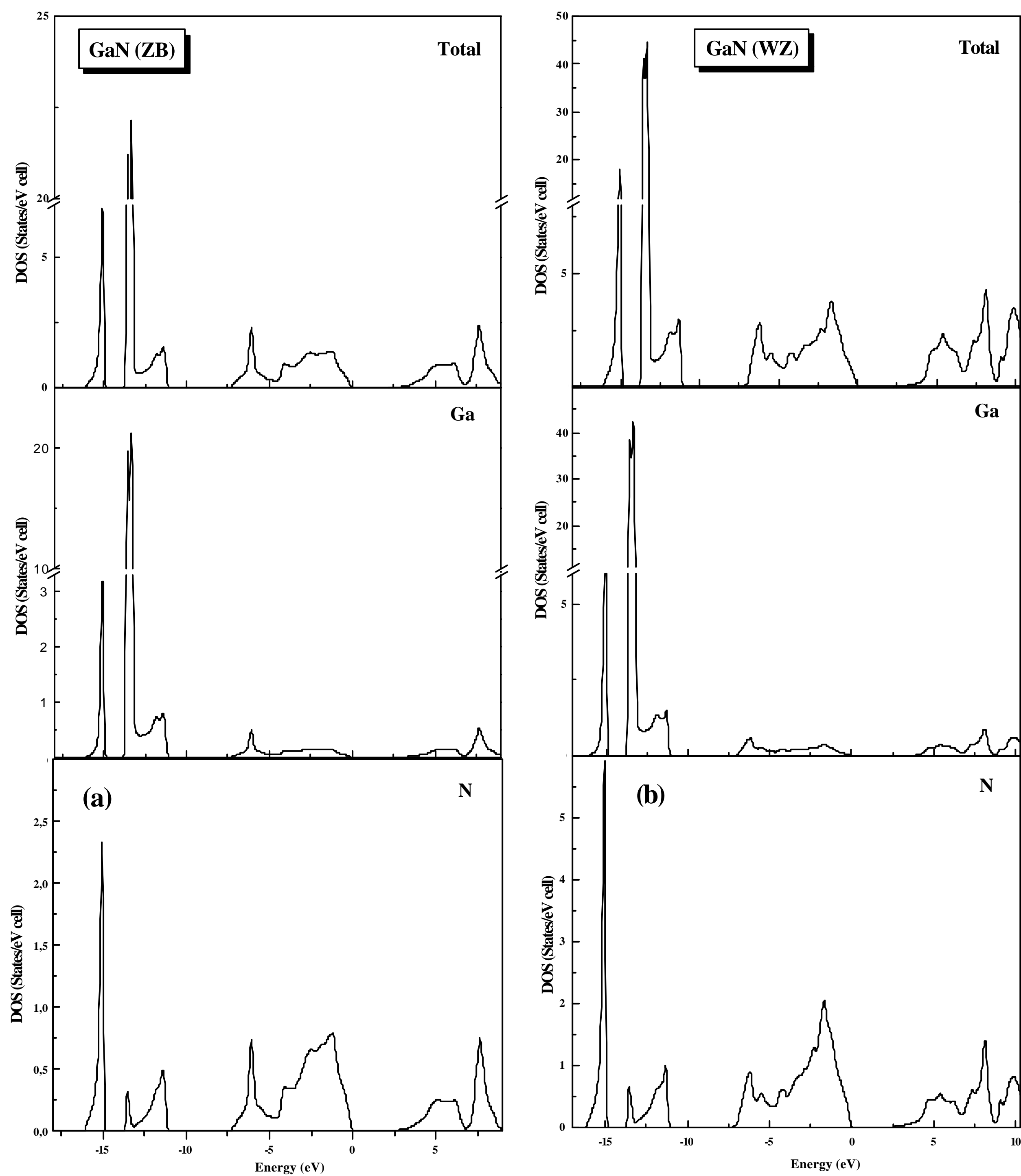

Figure V.I.11. Calculated total and partial density of states in (a) ZB-GaN and (b) WZ-GaN, when Ga 3d are treated as valence states.

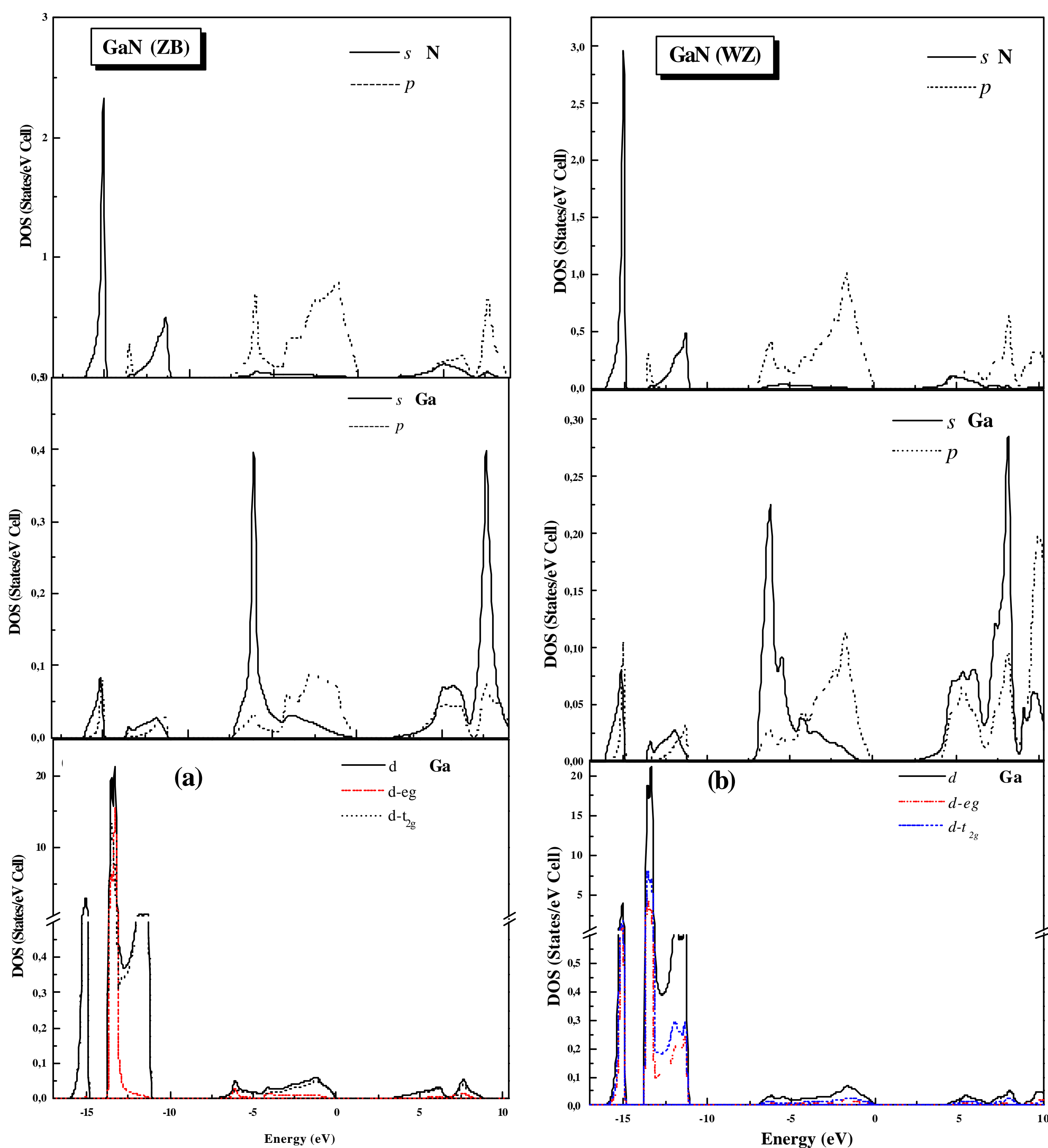

Figures V.I.12. The angular-momentum decomposition of the atom-projected densities of states in (a) ZB-GaN and (b) WZ-GaN, when Ga treated as valence states. The d-e_g and d-t_{2g} are degenerated of the d bands with the e_g is doubly degenerated and the t_{2g} is triply degenerated.

V. I. 3. 3. Electronic charge densities:

The charge density distribution is an important property of solids in the fact that provide a good description of the chemical properties. The investigation of chemical trends in solid-state properties appears as an extremely useful part of new material research. Performing those calculations, we try to gain some information about the III-V Nitrides.

The ionic character of any material can be related to the charge transfer between the cation and anion. For this reason, we have calculated the charge densities for AlN and GaN in zincblende and wurtzite structures. The total valence charge densities for AlN and GaN both zincblende and wurtzite are illustrated along the Al-N and Ga-N bonds (see Figures V.I.13 and V.I.14). In Figures V.I.15 and V.I.16 represent the total valence charge densities for AlN and GaN in the both zincblende and wurtzite in the (110) plane containing Al (Ga) and N atoms. One can see clearly that the bonding charge is displaced strongly from the mid-point between the atoms towards the N atom. Besides, one notices that the situation in the ZB structure is analogous to that of the WZ structure. The displacement of the bonding charge listed above increases as the difference between the electronegativity values of the two atoms increases.

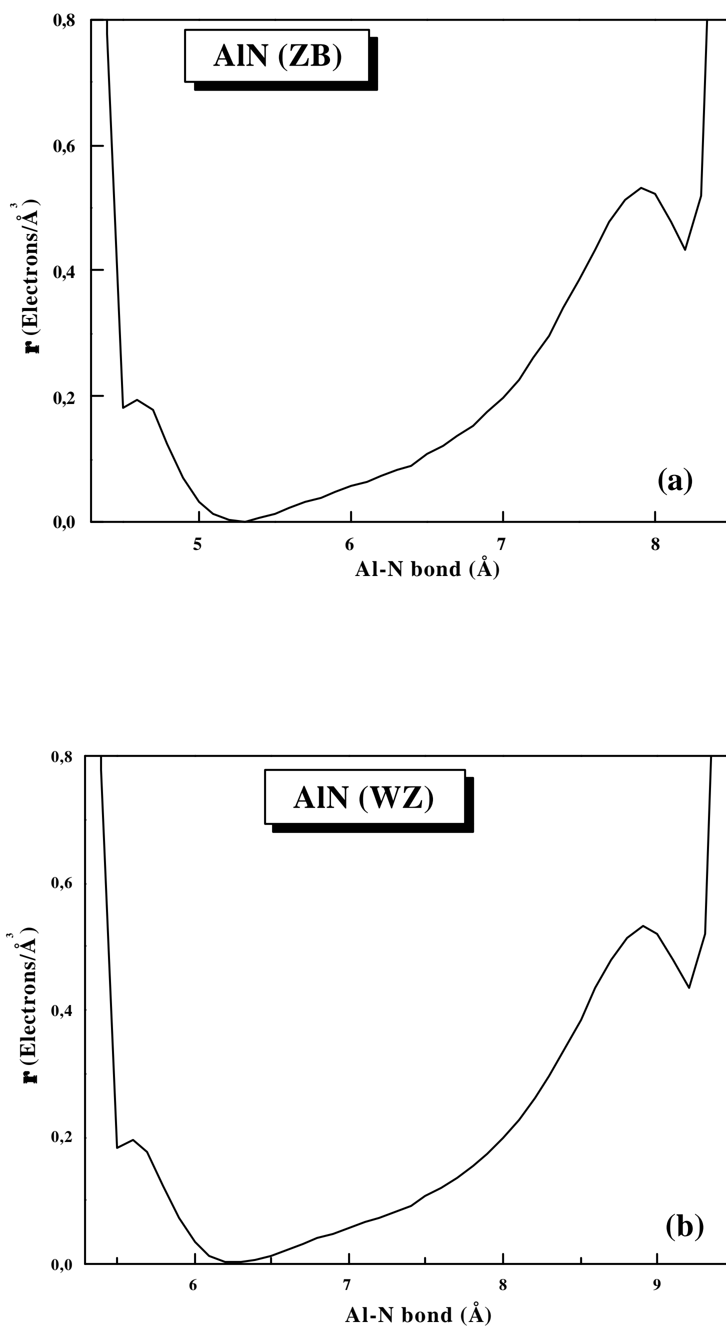

Figure V.I.13. Line plot of the calculated total valence charge densities along the Al-N bond direction for (a) ZB-AlN and (b) WZ-AlN.

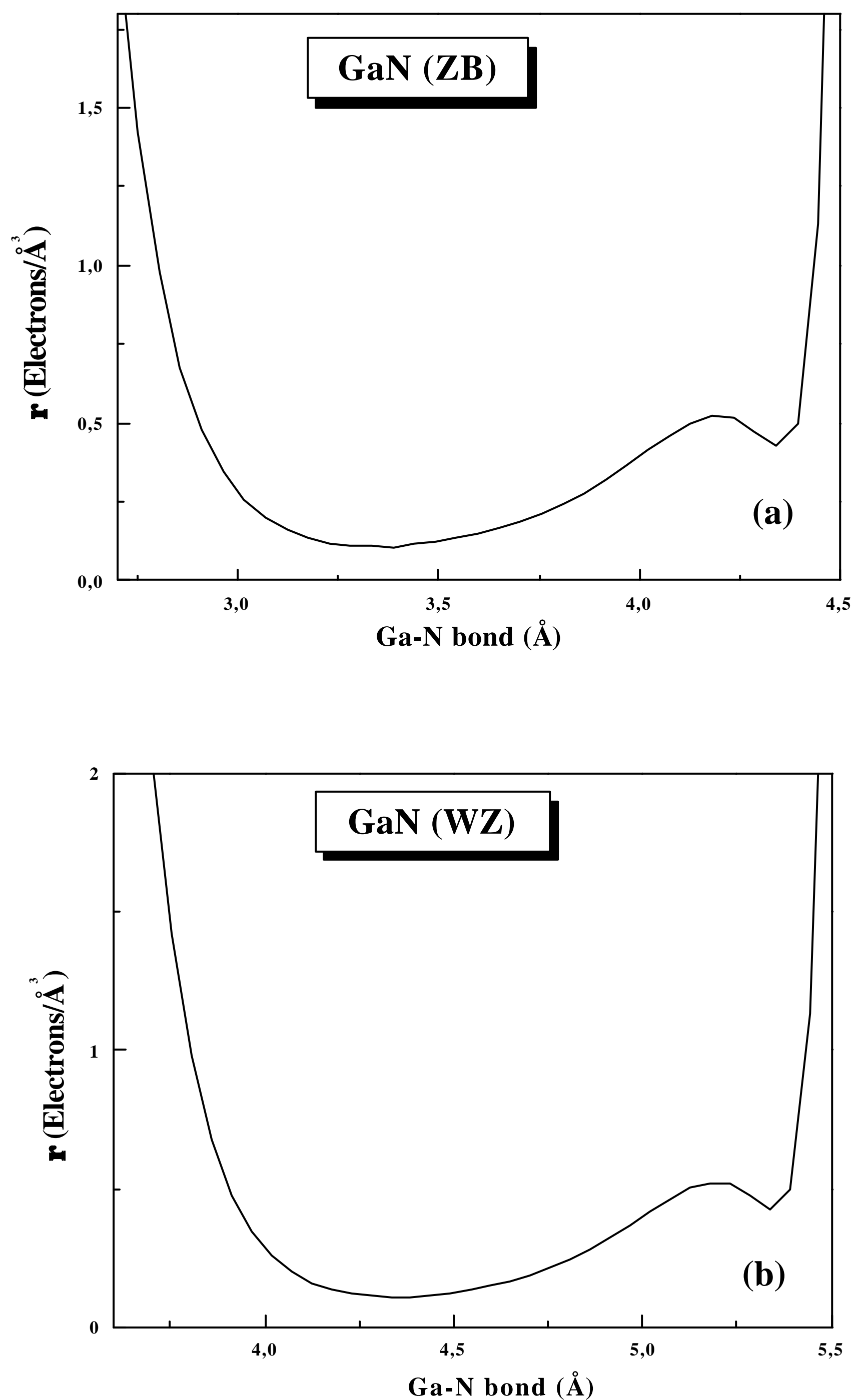

Figure V.I.14. Line plot of the calculated total valence charge densities along the Ga-N bond direction for (a) ZB-GaN and (b) WZ-GaN

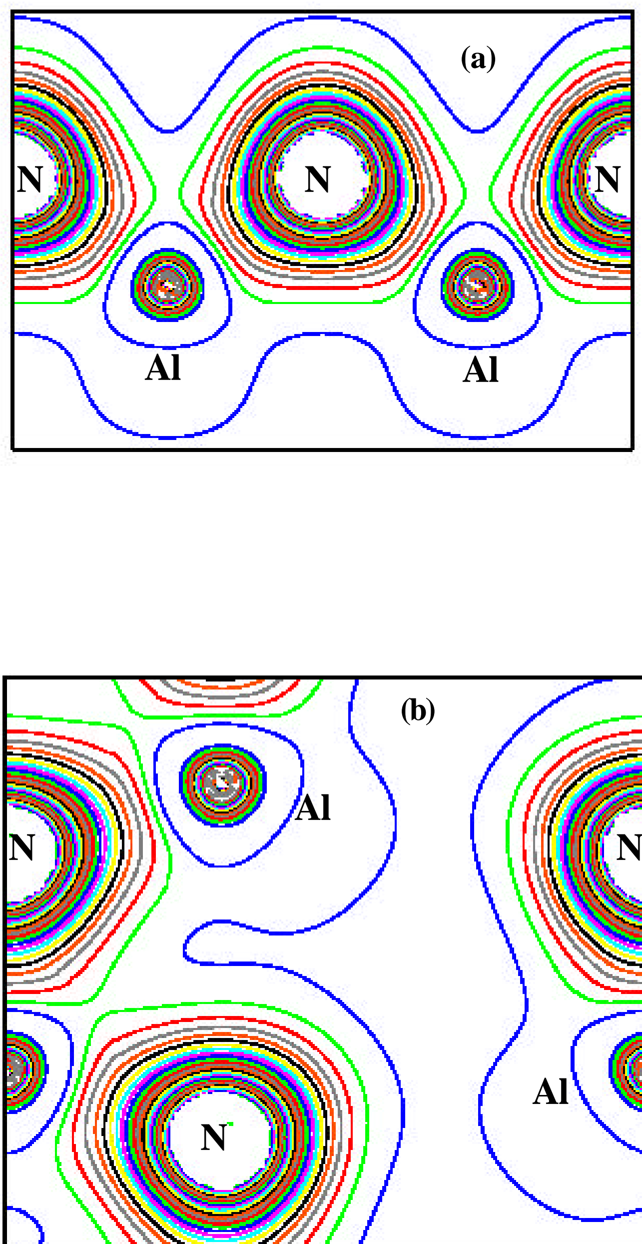

Figure V.I.15. Contour plot of the total valence charge density in the (110) plane of AlN (a) zincblende and (b) wurtzite.

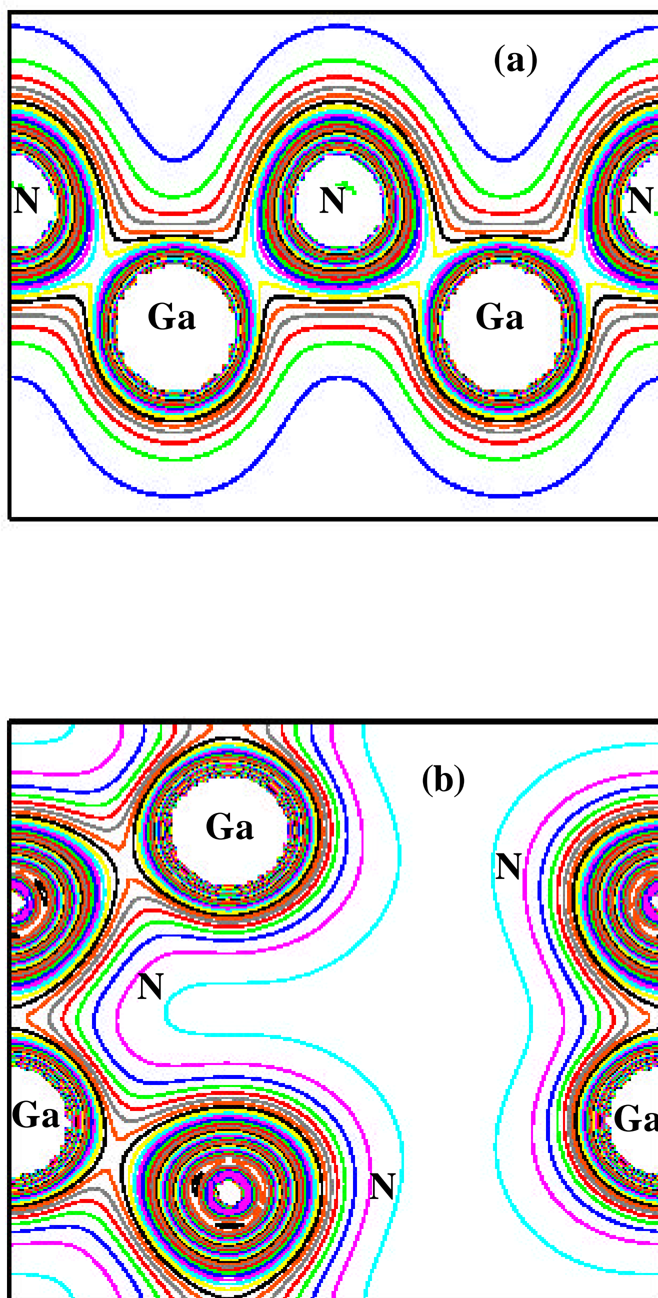

Figure V.I.16. Contour plot of the total valence charge density in the (110) plane of GaN (a) zincblende and (b) wurtzite.

V. I. 3. 4. Ionicity factor :

The ionicity of the bond is one of the standard concepts in solid-states theory. However, the problem in defining ionicity of a bond remains the difficulty of transforming a qualitative concept to quantitative formula.

Several considerations are taken into account when performing calculations for determination of the ionic character they are listed as follows: (i) The ionicity factor can be related to the difference in electronegativities of two atoms i.e. the Pauling Principle definition [66]). (ii) The charge asymmetry of a cation-anion bond is suggested to be a measure of the degree of ionic character. This is the basic idea of the Garcia and Cohen ionicity model [67]. (iii) The antisymmetric (heteropolar) gap (E_{asy}) has been proposed as a direct measure of crystal ionic energy by Phillips [45].

Two different approaches have been used to calculate the ionicity factor for AlN and GaN semiconductors in wurtzite and zincblende structures: the Garcia and Cohen approach based on the valence charge density calculation [67], and the Pauling definition based on the electronegativity values of the elements.

The scaling law introduced by Garcia and Cohen was successful in predicting the f behaviour for a wide variety of semiconductors. Garcia and Cohen [67] suggested using the asymmetry the charge density of a tetrahedral binary compound to measure their ionicity. However, these authors calculated charge densities using the total-energy pseudopotential method, and they deduced that ionicity factors exhibit a large discrepancy with Phillips ionicity scale for all the group III nitrides.

The Garcia and Cohen [67] ionicity factor is defined as :

$$f_i = \sqrt{\frac{S_a}{S_s}} \qquad \text{(V-I-2)}$$

where S_s and S_a are the symmetric and antisymmetric components strength measures of the of the charge density, respectively. They are defined by :

$$S_{s,a} \equiv \left(\frac{1}{V_0}\right) \int_{V_0} \boldsymbol{r}^2_{s,a}(r)\, d^3 r \qquad \text{(V-I-3)}$$

where $\boldsymbol{r}$ is the charge density components.

The estimation of the ionicity factor is obtained by using the Pauling equation:

$$f_i = 1 - \exp\left[-(\chi_A - \chi_B)^2 / 4\right] \qquad \text{(V-I-4)}$$

where χ_A and χ_B are the electronegativities of atoms A and B, respectively.

The calculated ionicity values for AlN and GaN compared with those of Phillips [43], Garcia and Cohen [67], Ferhat *et al* [68] and Tadjer *et al* [69] are summarized in Table V.I.10. Our values f_i for zincblende and wurtzite AlN and GaN are close to those given by Phillips for wurtzite structure and Ferhat *et al* and Tadjer *et al* for cubic structure, but they are different from that found by Garcia and Cohen. The calculated ionicity is consistent with Pauling's [66]. Since both polytypes have the same tetrahedral environment, where the local coordination of the first neighbor atomic positions is the same in the zincblende and the wurtzite structures. To well show the reliability of our calculated ionicity, we have plotted in figure V.I.17 the Phillips ionicity as function of the Garcia and Cohen factor ionicity. Our results of the GaN and AlN are found along the linear curve, which indicate that these values are corrected when compared with the Garcia and Cohen results.

Table V.I.10. *Calculated ionicity factor f of AlN and GaN in both zincblende and wurtzite structures. The differences in electronegativities,* $\chi_N - \chi_{Ga\ ou\ Al}$*; are also listed for comparison.*

	f_i^{WZ}	f_i^{ZB}		Calc. [43]	Calc. [67]	Calc. [68]	Calc. [69]
AlN	0.47	0.481[a]	0.56[b]	0.449	0.794	0.508	0.572
GaN	0.53	0.519[a]	0.58[b]	0.5	0.78	0.519	0.575

[a] Calculated using the Garcia and Cohen approach [67].

[b] Estimated using the Pauling definition [66].

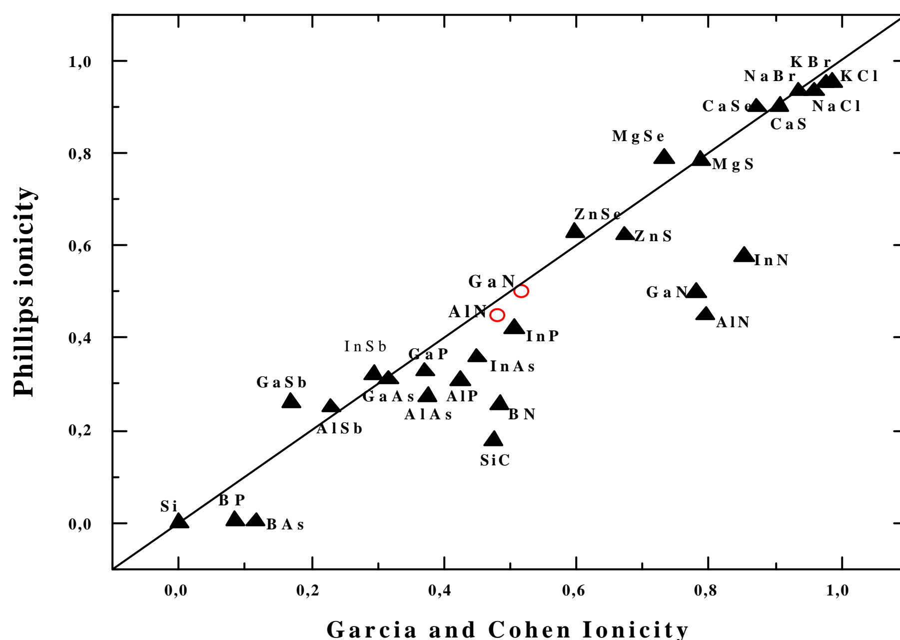

Figure V.I. 17. The Phillips ionicity as function of the Garcia and Cohen factor ionicity [67]. The open circles represent our calculated values.

V. I. 3. 5. Observation of semiconducting aspect at rocksalt phase

The electronic structure of AlN and GaN under high pressure has been a subject of great interest in recent years. Those materials convert to the rocksalt structure from the lower-pressure wurtzite or zincblende structure phases.

The band structures of the rocksalt phase of AlN and GaN, calculated by using LDA and GGA calculation, are shown in Figures V.I.18. For AlN, we show the indirect-bandgap semiconductor between Γ and X point. For GaN, we show also the indirect-bandgap semiconductor but between the valence band maximum at the L-point and the conduction band minimum along the X direction. Similar behavior has been observed in the case of band structures of zincblende and wurtzite, the GGA bandgaps are smaller than those of the LDA by ~20% for AlN and GaN in wurtzite and zinblende structures. The calculated band energies at high-symmetry points for AlN and GaN are given in Table V.I.11 and compared to other theoretical calculations. The RS -GaN is predicted to be an indirect-bandgap semiconductor with a bandgap of about 0.942 eV.

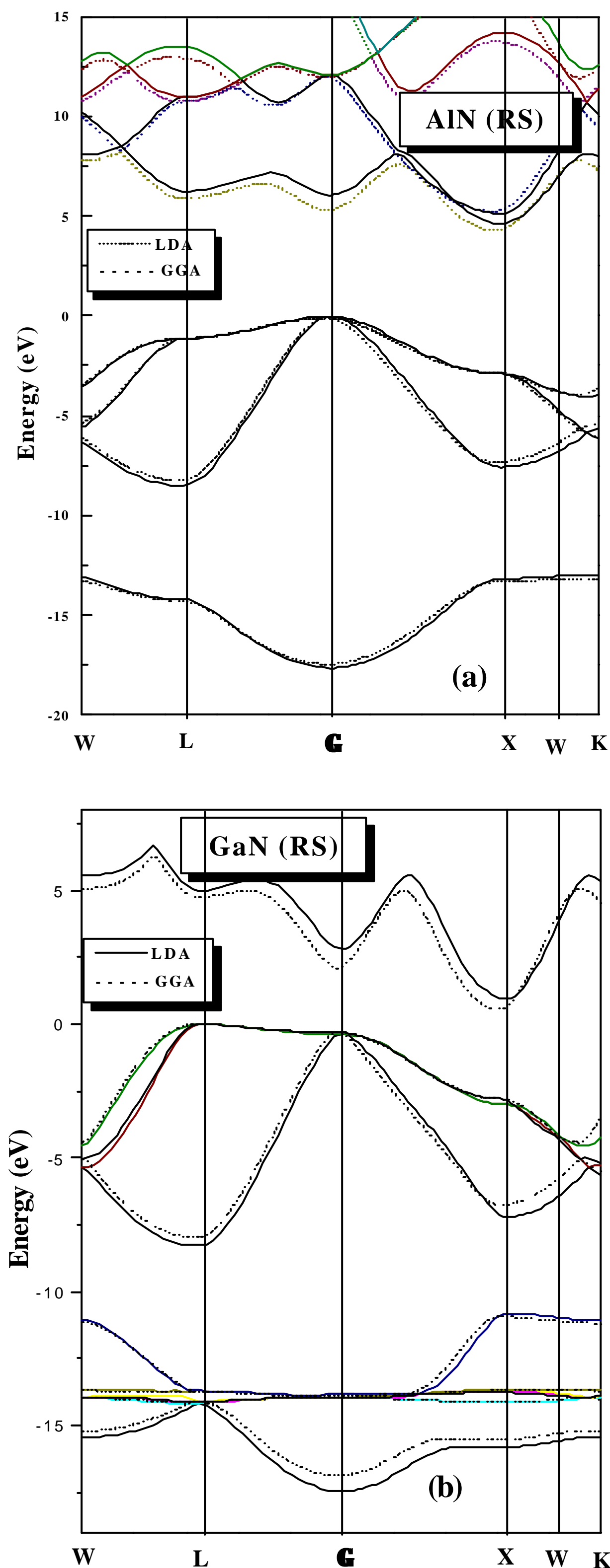

Figure V.I. 18. LDA and GGA Band structure of rocksalt (a) AlN and (b) GaN along the principle high-symmetry directions in the brillouin zone. The energy zero is taken at the valence band maximum.

Table V.I.11. *Calculated bandgaps of AlN and GaN in rocksalt structure to other theoretical calculations. All energies are in eV.*

	This work		Calculations
	LDA	**GGA**	
AlN			
$E_g(\Gamma^v - \Gamma^c)$	6.07	5.371	5.56[a], 4.99[b]
$E_g(\Gamma^v - X^c)$	4.651	4.40	4.65[a], 4.404[b]
$E_g(\Gamma^v - L^c)$	6.26	5.998	6.13[a], 5.52[b]
GaN			
$E_g(\Gamma^v - \Gamma^c)$	3.10	2.424	2.92[a], 3.16[b], 2.5[c]
$E_g(\Gamma^v - X^c)$	1.257	0.876	1.0[a], 1.01[b], 0.5[c]
$E_g(\Gamma^v - L^c)$	5.316	5.076	-
$E_g(L^v - X^c)$	0.942	0.56	-

[a] Ref. [21], [b] Ref. [70], [c] Ref. [54],

V. I. 4. Elastic properties

In the following, we study the AlN and the GaN compounds in their metastable zincblende phase because there are little experimental data and theoretical works under strain and stress effect. Furthermore, the zincblende structure is of technological interest as it can be doped more easily than the wurtzite structure.

V. I. 4. 1. Elastic constants

The shear modulus requires knowledge of the derivative of the energy as a function of a lattice strain [71]. In the case of a cubic lattice, it is possible to choose this strain so that the volume of the unit cell is preserved. The strain can be chosen so that the energy is an even function of the strain, whence an expansion of the energy in powers of the strain contains no odd powers.

We calculate the elastic properties of AlN and GaN by computing the components of the stress tensor ε for small strains, using the method developed recently by Charpin [72,73]. It is well known that a cubic crystal has only three independent elastic constant C_{11}, C_{12} and C_{44}. So a set of three equations is needed to determine all the constants, which means that three types of strain must be applied to the starting crystal.

The first type involves calculating the elastic modulus (C_{11} + $2C_{12}$), which are related to the bulk modulus B :

$$B = \frac{1}{3}\left(C_{11} + 2C_{12}\right) \qquad \text{(V-I-5)}$$

The second type involves performing volume-conservative tetragonal strain tensor. We vary the ratio c/a=(1+e) for several user-supplied values of e leading to the strain tensor ε :

$$\bar{e} = \begin{pmatrix} e_1 & 0 & 0 \\ 0 & e_1 & 0 \\ 0 & 0 & \dfrac{1}{(1+e_1)^2} - 1 \end{pmatrix} \qquad \text{(V-I-6)}$$

Where $e_1 = (1+e)^{-1/3-1}$

Where the application of this strain have an effect on the total energy from its unstrained value as follow:

$$E(e_1) = 6(C_{11} - C_{12})V\, e_1^2 + 0(e_1^3) \quad \text{(V-I-7)}$$

where V is the volume of the unit cell.

Finally for the last type of deformation, we use the volume-conserving rhombohedral strain tensor given by:

$$\bar{e} = \frac{e}{3}\begin{pmatrix} 1 & 1 & 1 \\ 1 & 1 & 1 \\ 1 & 1 & 1 \end{pmatrix} \quad \text{(V-I-8)}$$

Which transforms the total energy to

$$E(e_1) = \frac{1}{3}(C_{11} + 2C_{12} + 2C_{44})V\, e_1^2 + 0(e_1^3) \quad \text{(V-I-9)}$$

For cubic crystal, the shear wave modulus is given by:

$$C_S = \frac{1}{2}(C_{11} - C_{12}) \quad \text{(V-I-10)}$$

The calculated elastic constants are summarized in Table V.I.12 and V.I.13. To our knowledge, because there are not any available experimental results, we compare our main finding of zincblende AlN and GaN with some available *ab initio* calculations works [26,31,32,74]. It is obvious to observe a good agreement between our results and those found recently.

V. I. 4. 2. Internal-strain parameters

The well-known Kleinman parameter z for zincblende describes the relative positions of the cation and anion sublattices under volume by conserving strain distortions in which the positions are not fixed by symmetry. The internal-strain parameter is calculated using the following relation [75,76] :

$$V = \frac{C_{11} + 8C_{12}}{7C_{11} + 2C_{12}} \quad \text{(V-I-11)}$$

The calculated values for this parameter are given in Table V.I.12 and V.I.13 for AlN and GaN in zincblende structure, respectively. It can be noted that our values for AlN and GaN are in reasonably good agreement with the existing data obtained from *ab initio* calculations [26,31,32]. We recall that a low value of internal-strain parameter implies that there is a large resistance against bond-angle distortions while the reverse is true for a high value.

Table V.I.12. *Elastic constants and internal-strain parameter of zincblende AlN*

	This work	Calculations
C_{11} (GPa)	313.24	304[a], 313[b], 294[c]
C_{12} (GPa)	156.47	152[a], 160[b], 168[c]
C_{44} (GPa)	202	199[a], 192[b], 198[c]
C_S (GPa)	78.39	76[a], 76.5[b], 63[c]
z	0.62	0.6[a], 0.56[b], 0.67[c]

[a] Ref. [26], [b] Ref. [31], [c] Ref. [32]

Table V.I.13. *Elastic constants and internal-strain parameter of zincblende GaN*

	This work	Calculations
C_{11} (GPa)	274.2	296[a], 285[b], 293[c], 285[d]
C_{12} (GPa)	166.1	155[a], 159[b], 161[c], 156[d]
C_{44} (GPa)	199	206[a], 155[b], 149[c], 150[d]
C_S (GPa)	54.05	71[a], 67[b], 62[c], 64.5[d]
z	0.71	0.5[a], 0.6[b], 0.67[c]

[a] Ref. [26], [b] Ref. [31], [c] Ref. [32],[d] Ref. [74]

V. I. 5. Piezoelectric properties :

Considered as materials with partially ionic bonds character the group-III nitrides exhibit the piezoelectric effect. In fact the piezoelectric polarization fields are induced from internal displacements of the group-III atoms relative to the nitrogen atoms in an elementary cell. In the zincblende structure this happens only for shear strains [34].

In the absence of external fields, the total macroscopic polarization of a solid is the sum of the strain-induced or piezoelectric polarization P. In the linear regime, the piezoelectric polarization is simply expressed via the piezoelectric coefficient and is related to the strain $\boldsymbol{\varepsilon}$ by the following expression:

$$P_i = \sum_i e_{ij}\, \boldsymbol{\varepsilon}_j \qquad \text{(V-I-12)}$$

This equation defines the components of piezoelectric tensor e_{ij}. $\boldsymbol{\varepsilon}$ is the strain in-plane which is assumed to be isotropic.

Zincblende is the structure with highest symmetry compatible with the existence of piezoelectric polarization under strain [78]. The piezoelectric tensor of zincblende has one nonvanishing independent component (e_{14}). Therefore, the polarization in these materials system will have a one piezoelectric coefficient.

In Harrison [74] approach, the macroscopic piezoelectric tensor coefficients e_{14} is defined by :

$$e_{14} = e_p^* \mathbf{V} \frac{e}{a^2} \qquad \text{(V-I-13)}$$

where e_p^* is the piezoelectric charge given by:

$$e_p^* = 4\boldsymbol{\alpha}_p - \Delta Z - \frac{8}{3}\boldsymbol{\alpha}_p\left(1-\boldsymbol{\alpha}_p^2\right)\left(\frac{1-\mathbf{V}}{\mathbf{V}}\right) \qquad \text{(V-I-14)}$$

where $\boldsymbol{\Delta Z}$ = 1 for III-V compounds.

$\boldsymbol{\alpha}_p$ is the bond polarity depending on f_i (ionicity factor), and is given by :

$$\boldsymbol{\alpha}_p = \sqrt{1-\left(1-f_i\right)^{\frac{2}{3}}} \qquad \text{(V-I-15)}$$

The transverse effective charges are fundamental quantities, which specify the leading coupling between lattice displacements and electrostatic fields in insulators. However for semiconductors compounds of the zincblende structure, which are the focus here, it is easily shown that the effective charges are scalars, and are equal and opposite for cation and anion; it is conventional to use the positive cation effective charge to characterize a given compound. The transverse effective charge is defined as follows :

$$e_T^* = 4\alpha_p - \Delta Z + \frac{8}{3}\alpha_p\left(1-\alpha_p^2\right) \qquad \text{(V-I-16)}$$

In Table V.I.14 and V.I.15, we report the polarity, piezoelectric charge, piezoelectric constant and transverse effective charge for AlN and GaN compounds. Our results for these materials agree well with the available experimental [79] value of e_{14} for GaN and others theoretical works [31,32,75,80,81]. To facilitate further comparison with other III-V and II-VI systems, we collect the piezoelectric constants and transverse effective charge for a number of III-V and II-VI compounds from References [82-87] in Table V.I.16.

It well know that the nitrides follow qualitatively a well-defined III-V trend: the piezoelectric constants increase in magnitude as a function of the anion chemical identity as one moves upwards within period V, i.e., from Sb to N, because the ionic contribution tends to prevail over the electronic clamped-ion term as the anion becomes lighter

From Table V.I.14 and V.I.15, overall the piezoelectric properties of AlN and GaN resemble II-VI compounds, and appear to be very different from conventional III-V semiconductors. The piezoelectric constants have the same sign as in II-VI compounds, and opposite to III-V compounds. While in normal III-V compounds the clamped-ion term is larger in absolute value than the internal-strain ionic contribution, in the nitrides the latter prevails to a larger transverse effective charge. Compared to normal III-V compounds, this sign inversion constitutes a qualitative difference of obvious practical relevance [82]. Consequently the nitrides are an extreme case of this trend, and their piezoelectric response is by far larger than that of all other III-V compounds and of opposite sign. In the zincblende structure the tensor of the transverse effective charges is isotropic. Due to the charge neutrality, the charges of the cation and anion only differ by the sign. Our results agree well with the few theoretical works. The transverse effective charge follows a clear chemical trend within the nitrides series.

Table V.I.14. *Polarity, piezoelectric charge, piezoelectric constants (in units of C/m^2) and transverse effective charge (in units of e) of zincblende AlN.*

	This work	Calculations
α_p	0.60	0.57[a]
e_p^*	0.821	1.03[a]
e_{14}	0.434	0.59[b], 0.67[c]
e_T^*	2.457	2.36[a], 2.55[b], 2.56[c]

[a] Ref. [74], [b] Ref. [31], [c] Ref. [80]

Table V.I.15. *Polarity, piezoelectric charge, piezoelectric constants (in units of C/m^2) and transverse effective charge (in units of e) of zincblende GaN.*

	This work	Calculations	Experiment
α_p	0.621	0.61[a]	-
e_p^*	1.06	1.13[a]	-
e_{14}	0.605	0.50[b], 0.68[c]	0.60[e]
e_T^*	2.50	2.43[a], 2.67[b], 2.65[f]	-

[a] Ref. [74], [b] Ref. [31], [c] Ref. [80], [d] Ref. [79], [e] Ref. [78], [f] Ref. [31]

Table V.I.16. *Piezoelectric constants (in C/m^2) and transverse effective charge (in e) of several zincblende compounds reported in Refs. [82-87].*

Compounds	e_{14}	e_T^*	Compounds	e_{14}	e_T^*
CdTe	0.084	2.367	AlAs	-0.03	2.03
ZnSe	0.10	2.03	GaAs	-0.35	2.16
ZnS	0.15	2.15	InAs	-0.08	2.53
AlP	0.11	2.28	AlSb	-0.13	2.30
GaP	-0.18	2.04	GaSb	-0.40	2.15
InP	0.12	2.55	InSb	-0.20	2.42

V. I. 6. Bandgaps pressure coefficients :

In order to investigate the pressure effects on zincblende AlN and GaN energy gaps, we examine the band energies at the selected symmetry points as a function of the pressure. The results of our calculation for the direct and indirect bandgaps (E_g^{Γ}, E_g^X and E_g^L) versus the pressure are shown in Figures V.I.19. Table V.I.17 and V.I.18 summarize the results of our calculated linear and sub-linear coefficients of bandgaps and E_{asy}, compared to the available theoretical works [22,26,88]. We notice that our results are in good agreement with the other prediction calculations. For zincblende GaN, we can see that when we treat the Ga 3d as valence states, our results for first pressure derivative coefficient (α) of bandgaps agree well with FP-LAPW calculations of Wei and Zunger [88] and FP-LMTO calculations of Kim et al [26] which consider the same treatment of the Ga 3d states. Our results for second pressure derivative coefficient (β) of bandgaps are also in good agreement with the LMTO calculations of Christensen and Gorczyca [22] which treat the Ga 3d electrons as core states. We can established then that the treatment of the Ga 3d states as valence states have a significant effect on first pressure derivative coefficient (α) more than on second pressure derivative coefficient (β) one. Since the linear pressure coefficients of E_g^{Γ}, E_g^X and E_g^L are positive (see Table V.I.17 and V.I.18) these main bandgaps are also increased under pressure. However the increase of E_g^X is less important than that of E_g^{Γ} and E_g^L.

We also study the behavior of the energy bandgaps versus the relative variation of the lattice constant ($\Delta a/a_0$) for AlN and GaN in zincblende structure (see Figures V.I.20). Our results show that the fundamental gap and the other X and L indirect gaps present a non-linear behavior. The calculated linear and sub-linear coefficients are listed for each band in Table V.I.19 and V.I.20 compared with the other calculations. Interestingly, the cubic lattice under hydrostatic pressure shows no change in gap ordering in the studied range of pressures.

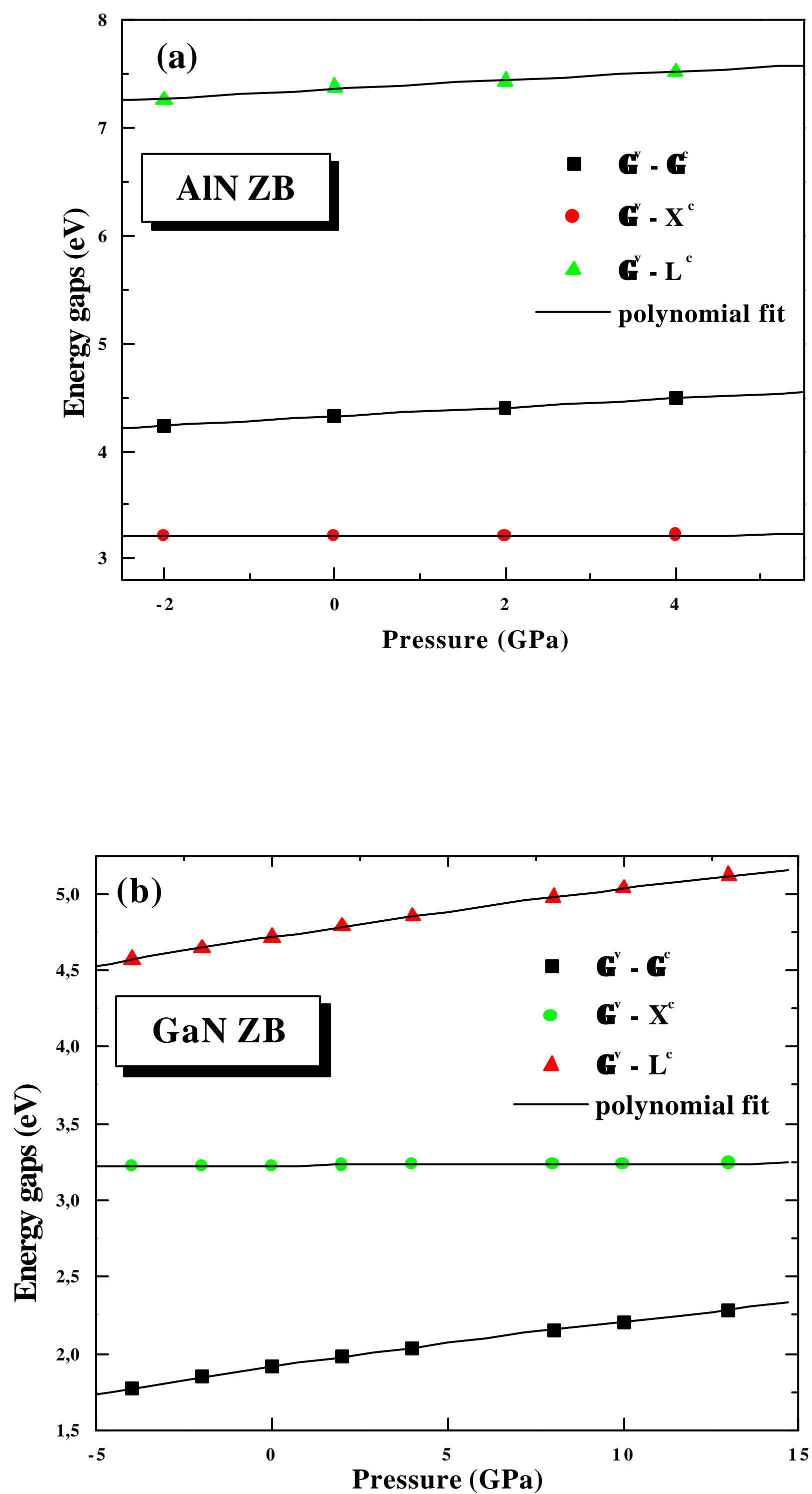

Figure V.I.19. Direct and indirect bandgap energies versus pressure in zincblende (a) AlN and (b) GaN.

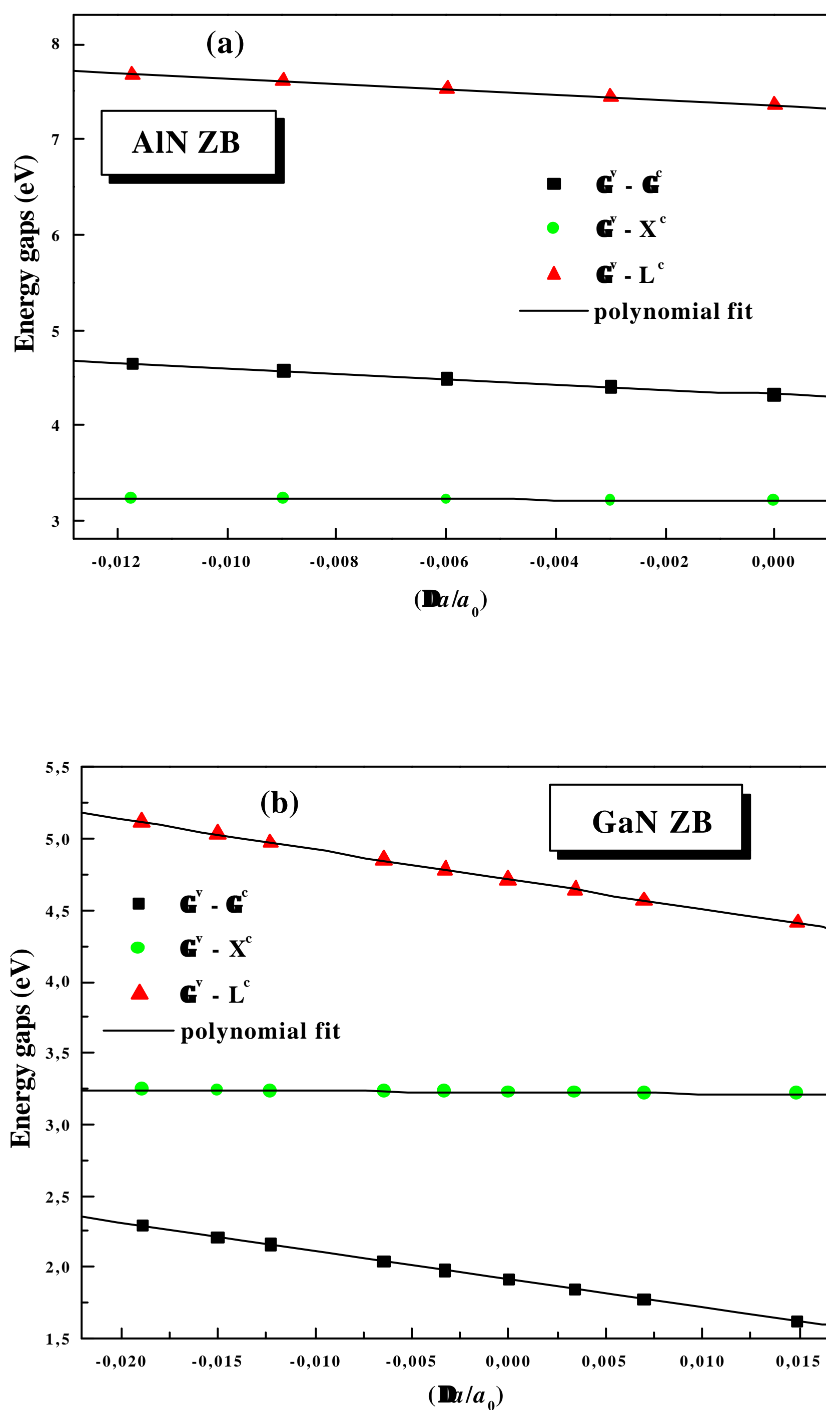

Figure V.I.20. Calculated dependence of the direct and indirect bandgaps in zincblende (a) AlN and (b) GaN on change lattice constant.

Table V.I.17. *Pressure coefficients related to $E_g(P)=E(a_0)+\alpha P+\beta P^2$ of the calculated values of the energy gaps for zincblende AlN and Compared with other calculations.*

	α (meV/GPa)		β (meV/GPa^2)	
	This work	**Calculations**	**This work**	**Calculations**
Γ^v - Γ^c	42.22	31[a], 42[b]	-0.36	-0.34[a]
Γ^v – X^c	2.02	1.70[a], 1.9[b], 1.9[c]	-0.037	-0.03[a]
Γ^v – L^c	42.57	44[a], 41.1[b]	-0.456	-0.38[a]
E_{asy}	-5.41	-	-0.018	-

[a] Ref. [22], [b] Ref. [88], [c] Ref. [26]

Table V.I.18. *Pressure coefficients related to $E_g(P)=E(a_0)+\alpha P+\beta P^2$ of the calculated values of the energy gaps for zincblende GaN and Compared with other calculations.*

	α (meV/GPa)		β (meV/GPa^2)	
	This work	**Calculations**	**This work**	**Calculations**
Γ^v - Γ^c	33.4	40[a], 31[b], 32[c]	-0.366	-0.38[a]
Γ^v – X^c	1.56	0.28[a], 1.7[b]	-0.034	-0.03[a]
Γ^v – L^c	35.5	42[a], 32.1[b]	-0.367	-0.38[a]
E_{asy}	-26.16	-	-0.249	-

[a] Ref. [22], [b] Ref. [88], [c] Ref. [26]

Table V.I.19. *Coefficients obtained from least-squares fits to $E_g(a)=E(a_0)+\gamma(\Delta a/a_0)+\delta(\Delta a/a_0)^2$ of zincblende AlN, where a is the lattice constant (a_0 is the equilibrium value).*

	γ (eV)		δ (eV)	
	This work	**Calc. [22]**	**This work**	**Calc. [22]**
Γ^v - Γ^c	-26.99	-27	38.44	37
Γ^v – X^c	-1.291	-1.10	-9.356	-7.30
Γ^v – L^c	-27.25	-28	40	31
E_{asy}	3.50	-	-22.95	-

Table V.I.20. *Coefficients obtained from least-squares fits to $E_g(a)=E(a_0)+\gamma(\Delta a/a_0)+\delta(\Delta a/a_0)^2$ of zincblende GaN, where a is the lattice constant (a_0 is the equilibrium value).*

	γ (eV)		δ (eV)	
	This work	**Calc. [22]**	**This work**	**Calc. [22]**
Γ^v - Γ^c	-19.81	-22	21.24	22
Γ^v – X^c	-0.90	-0.14	-6.13	-8.0
Γ^v – L^c	-21.07	-23	30	30
E_{asy}	15.19	-	-17.76	-

V. I. 7. Deformation Potential constants

The deformation potentials are important parameters to describe the electronic effects associated with strains originating, for instance, from the lattice mismatch between two layers of different semiconductors in heterostructures. To our knowledge, no experimental data for the hydrostatic deformation potential are presently available for AlN and GaN. The application of hydrostatic pressure, inducing a shift of the conduction-band edge relative to the valence band edge due to a change in the volume, allows a direct estimation of the hydrostatic deformation potential for bandgap of zincblende AlN and GaN. The deformation potentials are obtained by using the following equation:

$$a_g = V\frac{dE_g}{dV} \tag{V-I-17}$$

To determine how much of the band-gap deformation potential comes from conduction bands of AlN and GaN, we calculate the deformation potentials for the energy gaps at the points of high symmetry. The calculated values are summarized in Table V.I.21 and compared with other theoretical calculations. The bandgaps deformation potentials in zincblende structure AlN and GaN agree well with the cited theoretical calculations. We can see from this table that because we are treating of Ga 3d states as valence states, the obtained bandgap deformation potentials of GaN in zincblende structure are in good agreement with FP-LMTO calculations of Kim et al [26] and FP-LAPW calculations of

Wei and Zunger [88] more than with the previous LMTO calculations of Christensen and Gorczyca [22].

Table V.I.21. *Bandgap deformation potential constants for zincblende AlN and GaN.*

	AlN		GaN	
	This work	**Calculations**	**This work**	**Calculations**
$a_g^{\Gamma-\Gamma}$	-9.26	-9.0[a] , -9.04[b]	-6.518	-7.4[a], -6.4[c], -6.4[b]
$a_g^{\Gamma-X}$	-0.436	-0.37 [a], -0.42[b]	-0.2961	-0.05[a], -0.35[b]
$a_g^{\Gamma-L}$	-9.35	-9.40 [a], -9.04[b]	-6.9401	-7.7[a], -6.72[b]

[a] Ref. [22], [b] Ref. [88], [c] Ref. [26]

V. I. 8. Chemical trends in the pressure coefficient:

Our analysis for AlN and GaN compouds indicate that $s-s$, $p-p$ coupling enhance the pressure coefficient a_p^{GG}, whole the $p-d$ coupling reduces the pressure coefficients. The fast reduction of the bulk modulus as bond length increases enhances the pressure coefficients of compounds with large atomic size [88].

The pressure coefficient a_p^{GG} decreases significantly when the cation-atomic number increases. For example, the LDA a_p^{GG} are 42.22 and 33.4 meV/GPa for AlN and GaN, respectively. In this case, the decrease in a_p^{GG} is mainly due to the large decrease in bulk modulus when cation atomic number increases. We find that a_p^{GL} has similar trends as a_p^{GG}, but the variation is smaller. The small variation in a_p^{GL} is due to the more complete cancellation between the reduced level repulsion and the reduced bulk modulus as bond length increases. Finally, we find that a_p^{GX} is usually small and positive. The positive pressure coefficients a_p^{GX} is due to lack of the level repulsion between the X_{6c} state and unoccupied d state with the same principle quantum number as the valence s and p state [89], and also of the large $p-d$ repulsion of occupied states at the valence band maximum.

V. I. 9. Ionicity factor under pressure:

A correlation between the ionic bonding and electronic properties in these compounds exists as predicted by Phillips [45]. An interesting feature linked to the ionicity is the antisymmetric gap from valence bands at X. This gap is related to the cation and anion potentials. The antisymmetric (heteropolar) gap has been proposed as a measure of the crystal ionicity. The decrease of the heteropolar gap is an indication of the increase of the ionicity factor of the material under hydrostatic pressure for the following reason.

We display also in Figures V.I.21, the charge densities of AlN and GaN for small compression of the crystal of value V equal to $0.965V_0$ and $0.977V_0$ corresponding to a pressure of 5.5 and 16 GPa respectively.

In fact we illustrate in Table V.I.19 and V.I.20, the positive linear coefficient of E_{asy} indicating that there is an increase as the lattice constant decreases. This splitting induces an increase of the ionicity with the pressure. Using the Garcia and Cohen [67] model, we display in Figures V.I.22 for instance this variation versus pressure. Our obtained coefficients of this variation are listed in Table V.I.22. Following Figures V.I.20, the increase of the ionic character is due to the increase of the charge density around the Al or Ga atom with respect to N atom as under pressure as it is shown.

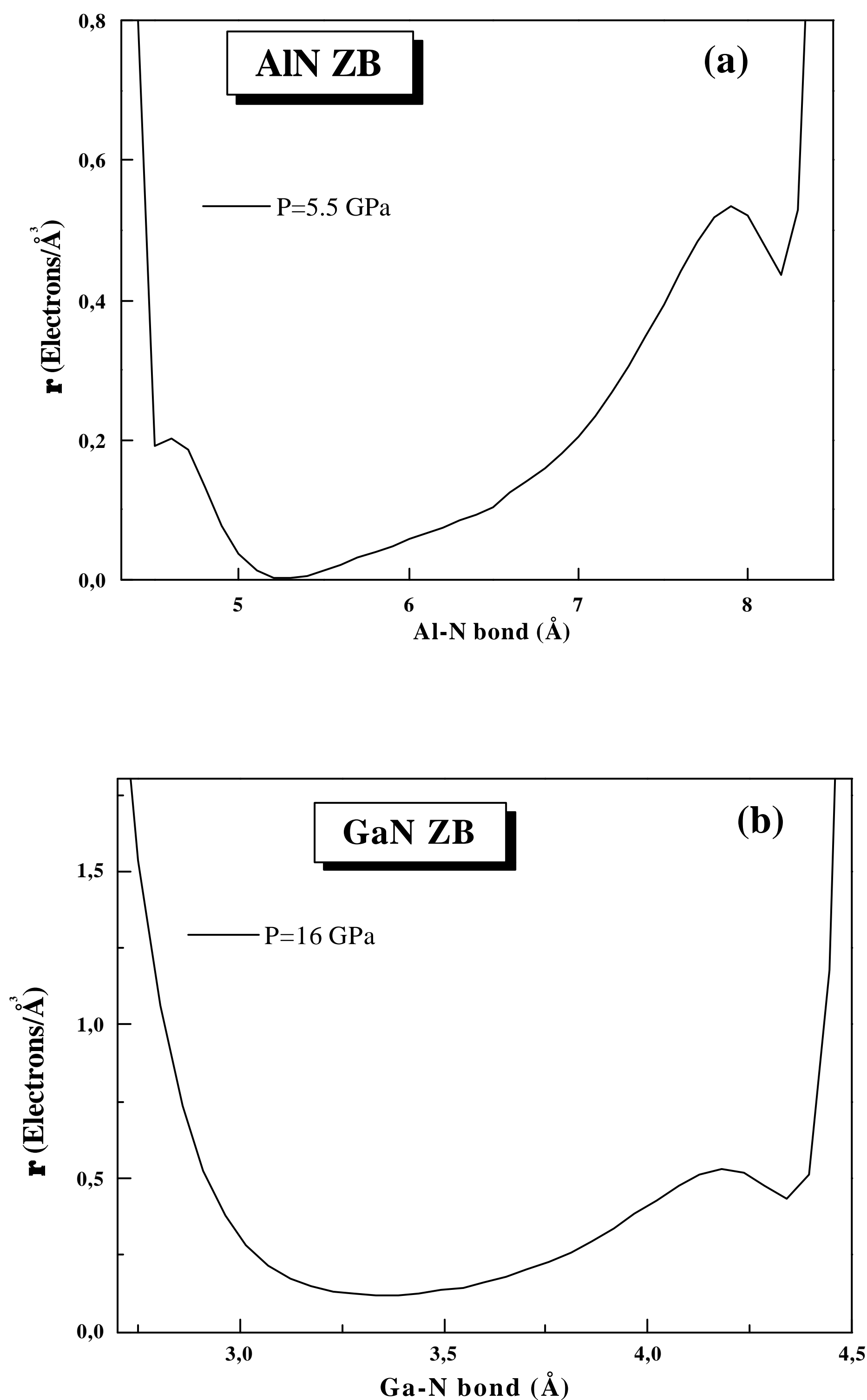

Figure V.I.21. Line plot of calculated total valence charge densities along the (a) Al-N and (b) Ga-N bond direction at normal and under pressure.

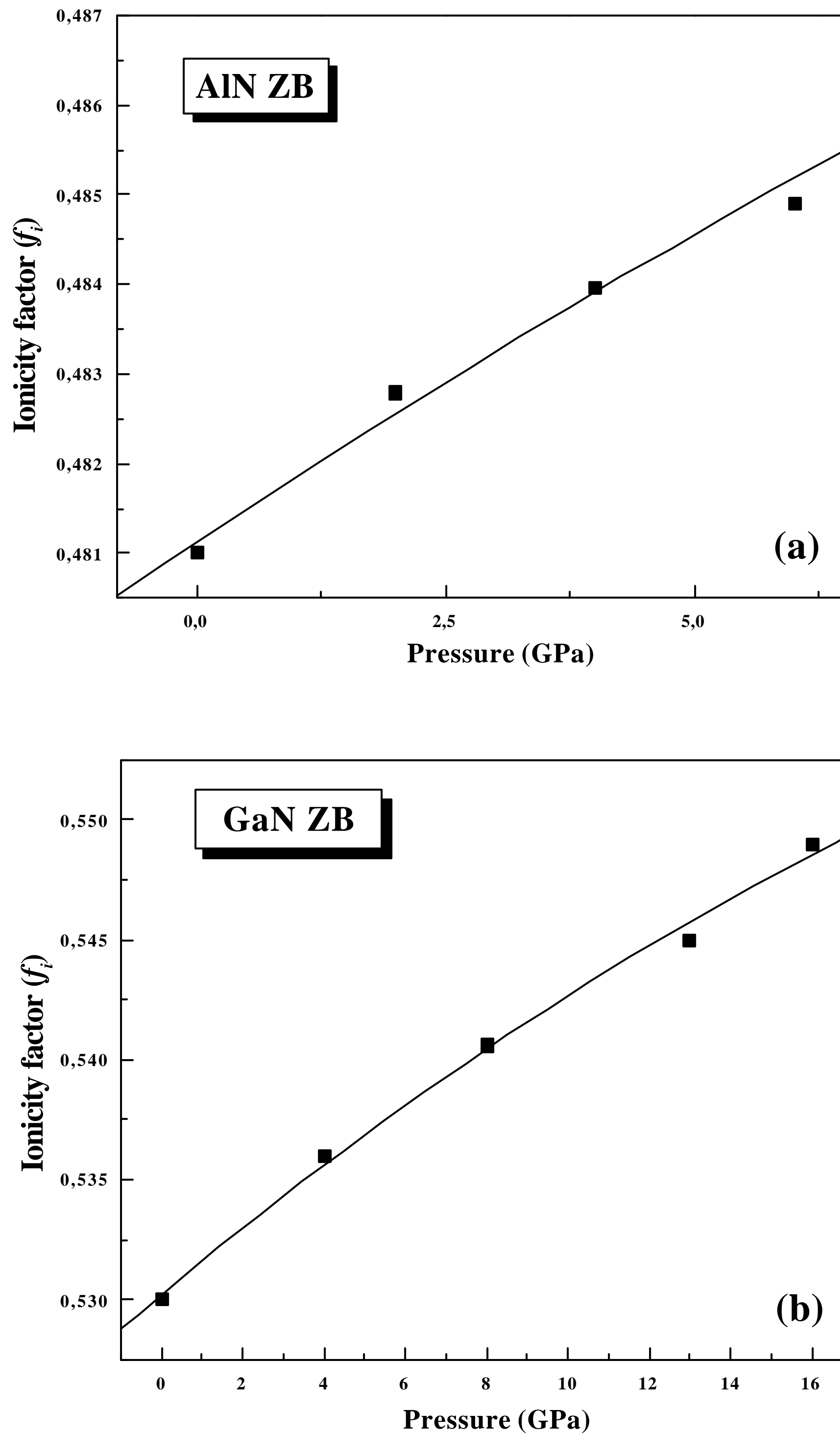

Figure V.I.22. Calculated dependence of the ionicity factor as a function of pressure for zincblende (a) AlN and (b) GaN.

Table V.I.22. *Calculated pressure coefficients related to* $f_i(P)=f_i(P=0)+\lambda P+\mu P^2$ *of the ionicity factor for zincblende AlN and GaN.*

	λ (10^{-3} /GPa)	μ (10^{-4} /GPa^2)
AlN	0.738	-0.1
GaN	1.4	-0.162

V. I. 10. Effect of pressure on elastic properties

The specific role of nitrogen is in the formation of short bonds, which leads to smaller lattice constants (by 20%) than for other III-V semiconductors. Under high pressure the III-nitride compounds undergo a structural phase transformation to a high coordination phase. For AlN the transition from cubic to rocksalt phase occurs in range of 7.1 GPa and for GaN the transition from cubic to high-pressure phase appears at 42.1 GPa [49].

An important motivation for high-pressure investigations stems from the fact that group-III-nitride layers are commonly subjected to large built-in strain since they are often grown on different substrates having considerable lattice mismatch within a difference in the thermal expansion coefficients between epitaxial layer and substrate. In the case of the heterostructures and superlattices, this situation become more complex and mutual influence between different materials layers may appears [90,91].

We are interesting to the study of pressure effect on elastic properties. We show in Figures V.I.23, the variation of elastic constants, internal-strain parameter and bulk modulus of AlN and GaN with respect to the variation of pressure. In all curves, we observe a linear dependence of pressure.

In Table V.I.23, we listed our calculated pressure derivatives dC_{11}/dp, dC_{12}/dp, dC_{44}/dp, dC_S/dp, $d\zeta/dp$ and dB/dp of the considered compounds. It is easy to observe that the elastic constants C_{11} and C_{12}, internal-strain parameter and bulk modulus increase when pressure is enhanced. Moreover the shown shear wave modulus C_S and the shear mode modulus C_{44}, which represent the extrema of the transverse moduli in cubic crystal [92], decrease linearly with the increasing of pressure for AlN and GaN.

Referring to our results and those found in literature [92,93], we have observed that there is a difference between the pressure derivatives of shear wave modulus and the elastic modulus of zincblende III-V semiconductors and zincblende AlN and GaN is observed. We notice that the results in Figures V.I.23 show no evidence that the soft acoustic mode is responsible for the phase transition in the considered range of pressure. These results were reported by different works [92,93,94], which treated III-V semiconductors. Our results may be considered as reliable predictions of the pressure dependence of the elastic properties and internal-strain parameter of zincblende AlN and GaN [95].

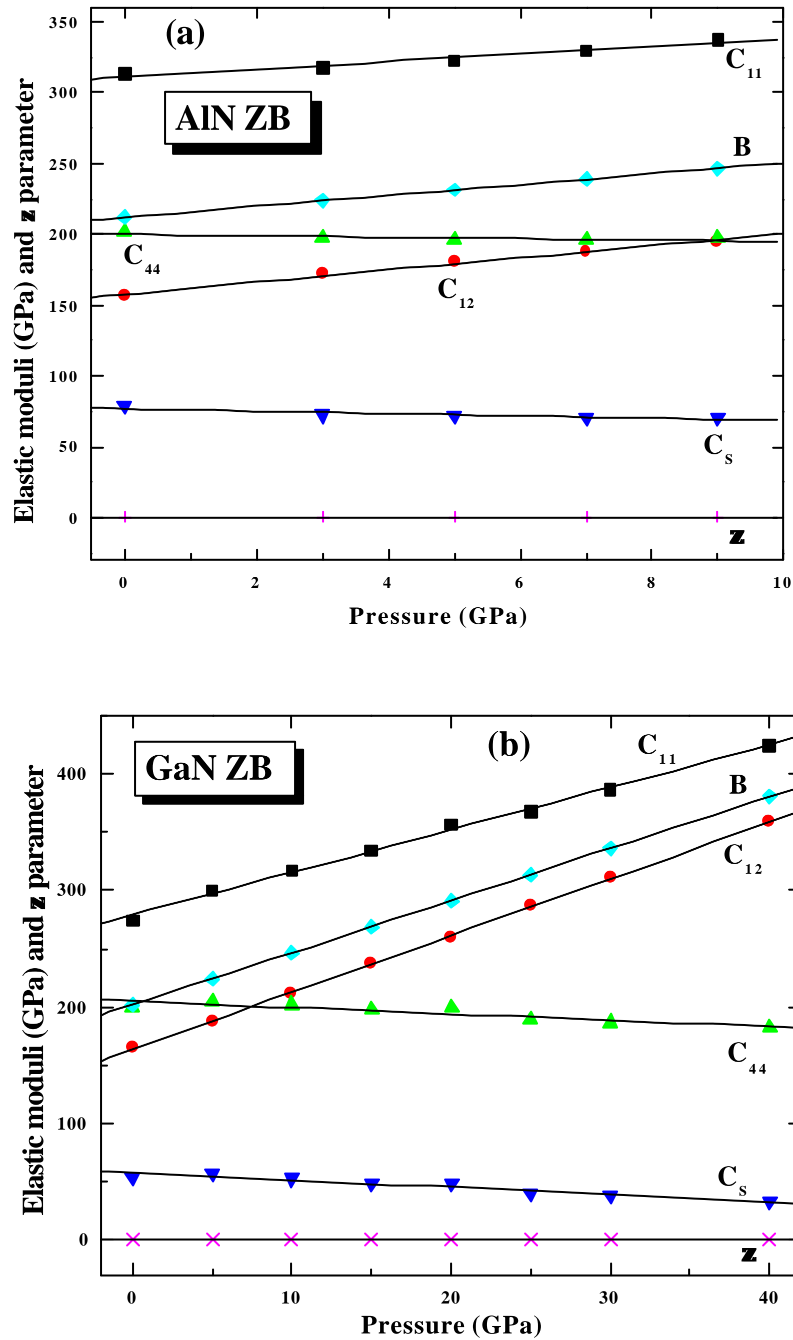

Figure V.I.23. Calculated pressure dependence of C_{ij}, C_S, *B and* **z** for zincblende (a) AlN and (b) GaN.

Table V.I.23. *Calculated pressure derivatives of the elastic modulus and internal-strain parameter for zincblende AlN and GaN.*

	dC_{11}/dp	dC_{12}/dp	dC_{44}/dp	dC_S/dp	dB/dp	$d\zeta/dp$ (10^{-3} GPa^{-1})
AlN	2.701	4.287	-0.511	-0.793	3.89	6.2
GaN	3.642	4.873	-0.55	-0.615	4.32	4.85

V. I. 11. Pressure effect of piezoelectric constants and transverse effective charges :

In Figures V.I.24, we present the variation of piezoelectric constants versus pressure. We observe a non-linear dependence of these curves and increase when pressure is increased. To explain this behavior, we give in Table V.I.24 and V.I.25, our calculated coefficients of piezoelectric constants for zincblende AlN and GaN. We observe that e_{14} exhibits rapidly changes with the hydrostatic pressure [96]. This largest change comes from the ionic contribution through the Kleinman parameter. But it is interesting to observe that there is another contribution which influences the piezoelectric constants, the charge transfer effect. The increase of the e_{14} in AlN and GaN was observed also on II-VI compounds [86], by contrary to results found for other III-V compounds (e.g. GaAs [97]).

The resulting values for transverse effective charges are plotted in Figures V.I.25, as a function of the pressure. In Table V.I. 24 and V.I. 25, we list our results compared with available experimental data [98]. Our results for GaN compared with experimental data [98] are satisfactory. From the literature the only known example of a tetrahedrally co-ordinated semiconductor exhibiting a larger transverse effective charge at reduced volume is SiC. In this case the lack of p electrons in the carbon core allows for a larger penetration of the Si wave functions into the carbon core regions, leading to an increase in ionicity and hence of e_T^* under pressure [99]. This situation is also observed for the nitrides since the nitrogen and carbon atomic cores look alike. Thus under pressure the transverse effective charges of GaN and AlN exhibit a similar but less marked behavior to that of SiC. For other III-V compounds like GaAs decrease with pressure giving rise to a reduction of e_T^* [100].

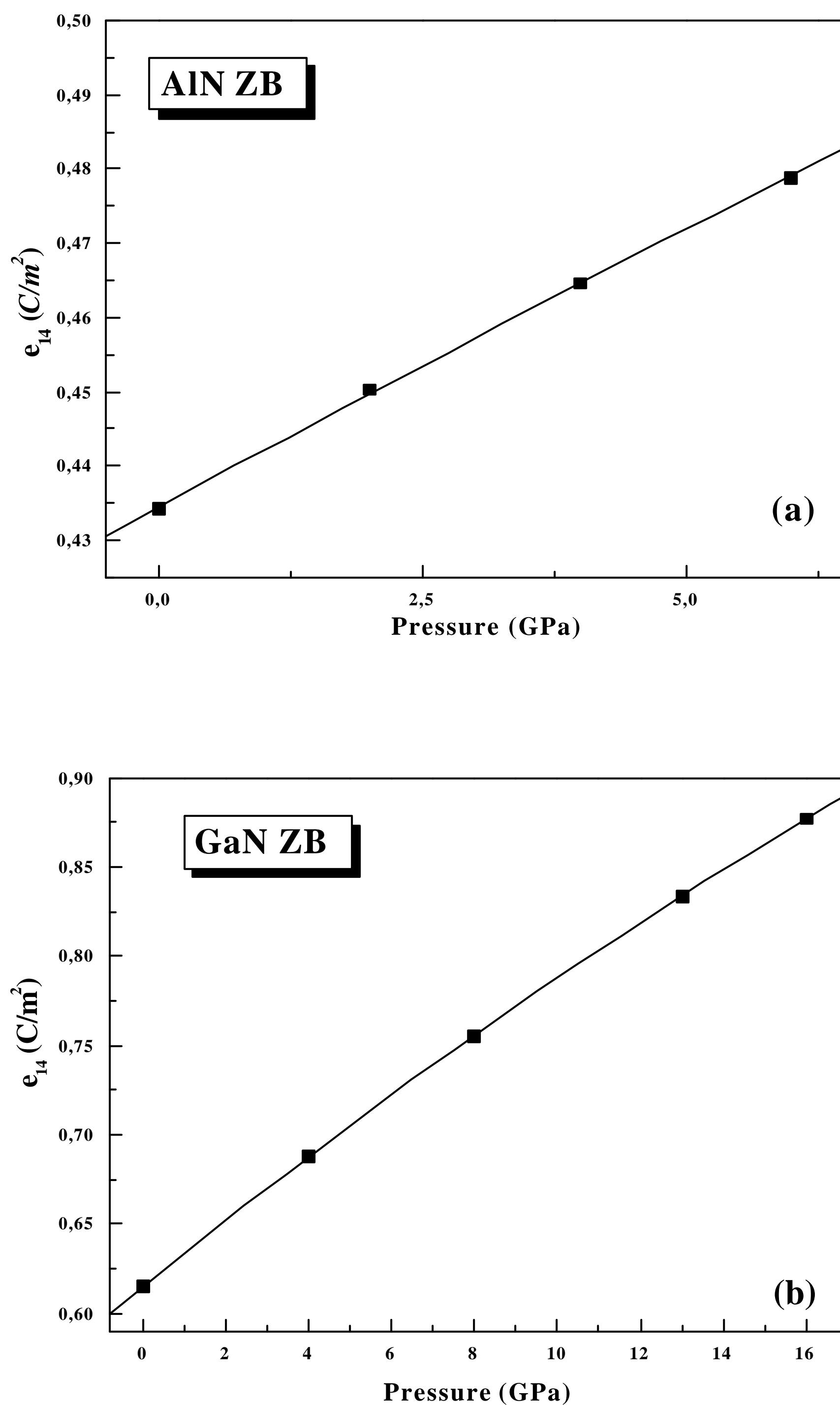

Figure V.I.I 24. Variation of the piezoelectric coefficient versus pressure of zincblende (a) AlN and (b) GaN.

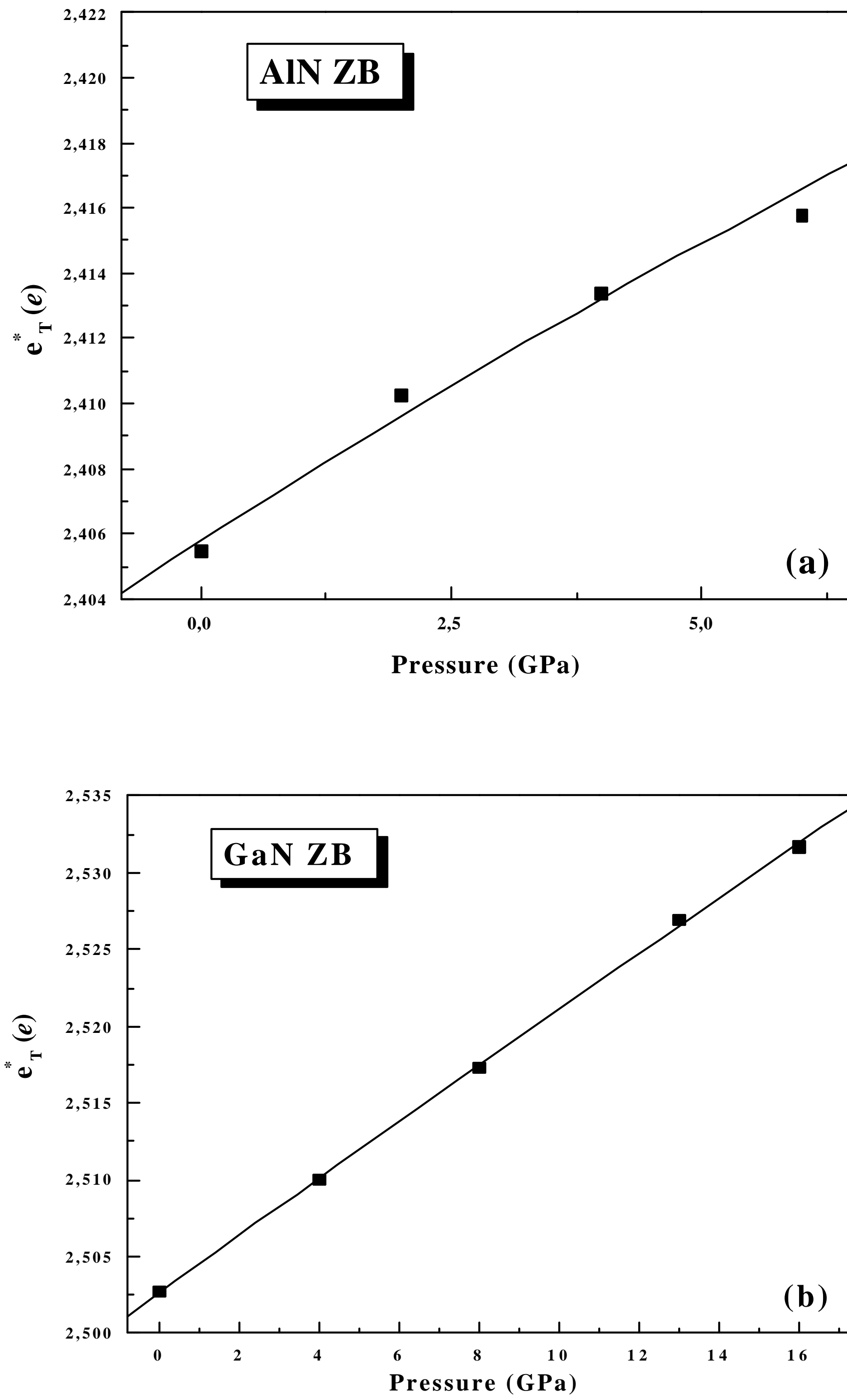

Figure V.I.I 25. Transverse effective charge versus pressure for zincblende (a) AlN and (b) GaN.

Table V.I.24. *Pressure coefficients of the polarity, piezoelectric charge, piezoelectric constants (in C/m^2) and transverse effective charge (in e) for zincblende AlN.*

	l (10^{-3} /GPa)	**m (10^{-4} /GPa^2)**
a_p	0.514	-0.07
e_p^*	8.75	-1.121
e_{14}	7.53	-0.478
e_T^*	1.97	-0.276

Table V.I.25. *Pressure coefficients of the polarity, piezoelectric charge, piezoelectric constants (in C/m^2) and transverse effective charge (in e) for zincblende GaN.*

	l (10^{-3} /GPa)	**m (10^{-4} /GPa^2)**
a_p	0.5261	-0.07
e_p^*	18.81	-2.47
e_{14}	17.0	-1.51
e_T^*	1.88, 0.5[a]	-0.039

[a] Reference from experimental [98].

V. I. 12. Calculation of energy loss near edge structure

Of increasing interest for the electron microscopist working with an energy spectrometer or an imaging energy filter is the interpretation of ionization edges, in particular energy loss near edge structures (ELNES), and low losses and their relation to electronic, optical and mechanical properties of modern materials. Electron energy-loss near-edge structure gives information about the distribution of unoccupied electronic states. ELNES is specific for every element in a given environment and thus acts like a fingerprint that allows identifying a specific environment around a specific atom. Good knowledge of the unoccupied states is also very important because it gives information about the optical and transport properties of the material. The calculations of the energy loss near edge structures have been performed using the FP-L/APW+lo method according to the formalism of M. Nelhiebel et al. [101-103]. In this section, we present spectra due to the gallium L-shell excitation and aluminum and nitrogen K- shell of AlN and GaN compounds.

In order to probe our calculational method, AlN and GaN have also been investigated in the zincblende structure. Their relative N-, Al-K and Ga-$L_{2,3}$ ELNES spectra are depicted in Figures V.I.26 and V.I.27. A seen from the presented figures (Figures V.I.26 and V.I.27), there is a good qualitative agreement between our results and available experimental data [103] for only GaN compound. The positions of the most prominent peaks (labelled I to IV) are listed in Table V.I.26. A reasonable correspondence between our calculations and the experimental results has been found in Table V.I.26.

Table V.I.26. *Positions of the peaks I-IV Figures V.I.26 and V.I.27 values are in units ofeV. The experiment values are compiled in ref.* [104].

	Edge		**I**	**II**	**III**	**IV**
AlN	N *K*	This Work	6.5	12.0	15.5	19.0
	Al *K*	This Work	6.25	12.25	15.5	19.3
GaN	N *K*	This Work	6.2	7.7	10.65	13.5
		Experiment	6.3	8.1	10.9	12.9
	Ga $L_{2,3}$	This Work	5.7	7.7	10.85	15.2
		Experiment	6.25	8.0	11.0	16.1

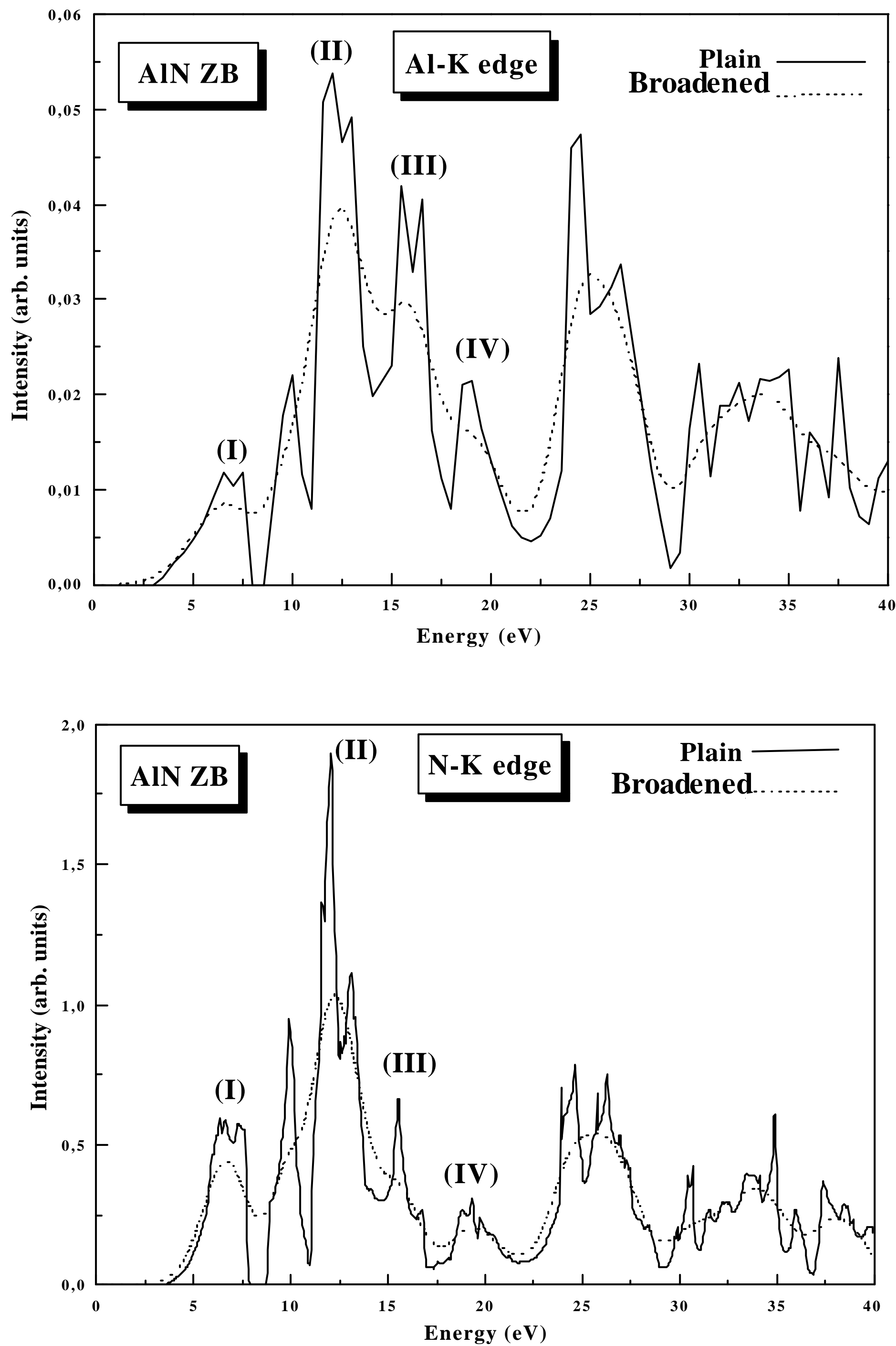

Figure V.I.26: Theoretical Al-K and N-K ELNES of zincblende AlN. The spectra for the inequivalent atoms positions have been calculated separately and weighted in the present Figure.

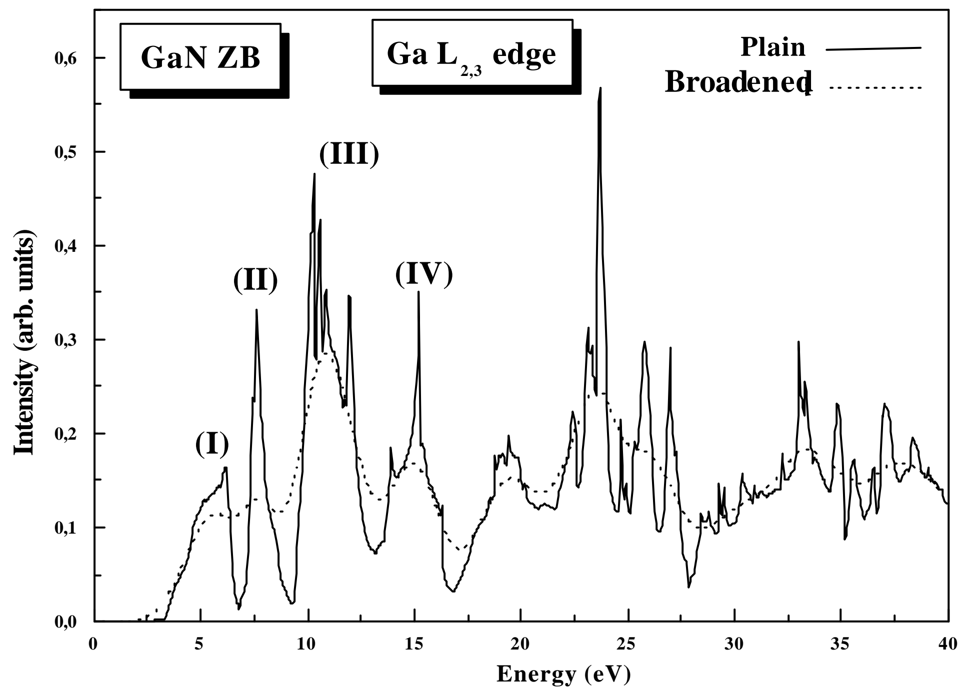

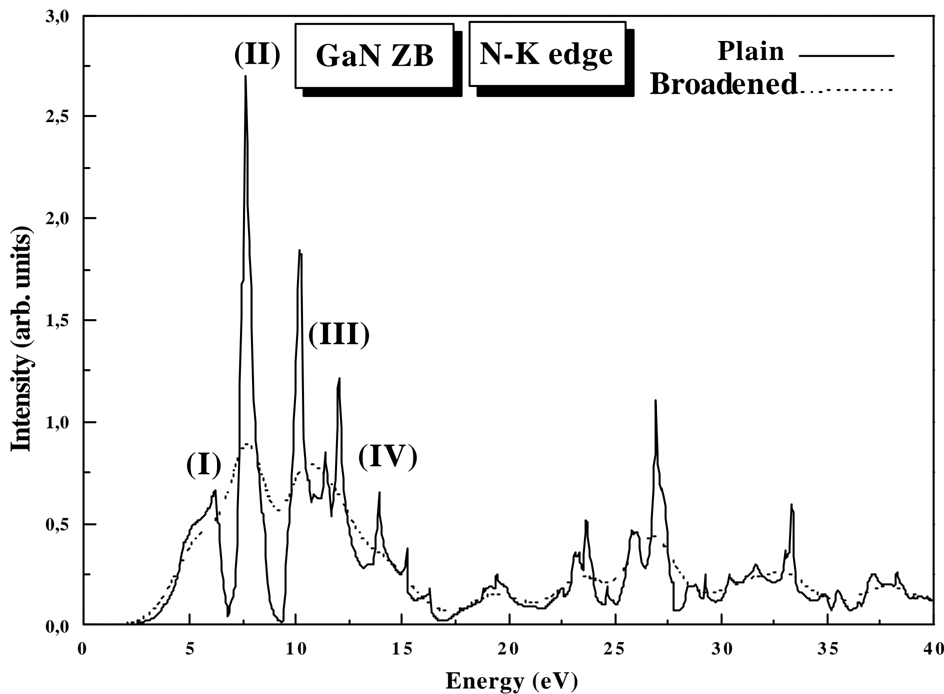

Figure V.I.27: Theoretical Ga-$L_{2,3}$ and N-K ELNES of zincblende GaN. The spectra for the inequivalent atoms positions have been calculated separately and weighted in the present Figure.

V. II. 1. Computational details

All calculations of GaN:Mn and AlN:Mn are performed by using the scalar relativistic full-potential augmented plane wave plus local orbitals (FP-L/APW+lo) [1,6] method within density functional theory (DFT). We employed the local-spin-density approximation (LSDA), implemented using the Perdew-Wang exchange-correlation functional [5]. Also, spin polarized calculations are achieved with two different spin-up and spin down densities and two sets of Kohn-Sham single equations particle equations, for the two spin components, are solved self-consistently. We have carried out all the total energy calculations without spin-orbit coupling. The doping of Mn in GaN and AlN compounds can be modeled by means of a structure with the cubic symmetry, in which the atom of Ga or Al is replaced by Mn atom to simulate an uniformly doped semiconductor with 25% Mn concentration.

Moreover, the core levels are treated fully relativistically. In particular, the Ga is considered in such away to include explicitly the semicore *d* electrons in the valence bands. In the following calculations, the FP-L/APW+lo basis set consisted of 4s, 4p and 3d orbitals of Mn, and 3s and 3p orbitals of Al and 4s, 4p and 3d orbitals of Ga and 2s and 2p orbitals of N. In this approach the wave function, charge density and potential are expanded differently in two regions of the unit cell. Inside the non-overlapping spheres of muffin-tin (MT) radius R_{MT} around each atom, spherical harmonics expansion is used and in the remaining space of the unit cell the plane wave basis set is chosen. The muffin-tin radius is taken to be 1.78 bohr for the gallium, aluminium, manganese and 1.60 bohr for the nitrogen

The maximum l value for the wave function expansion inside the atomic spheres was confined to l_{max}= 10. In order to achieve energy eigenvalues convergence, the wave functions in the interstitial region is expanded in plane waves with a cutoff of $R_{MT} * K_{MAX} = 8$ (where K_{MAX} is the maximum modulus for the reciprocal lattice vector, and R_{MT} is the average radius of the MT spheres). The k integration over the Brillouin zone is performed using Monkhorst and Pack [11] mesh, yielding to 11 k points in the irreducible wedge of the Brillouin zone for cubic structure.

V. II. 2. Structural optimization

The total energy of GaN:Mn and AlN:Mn has been calculated as a function of the global volume for each of the nonmagnetic (*nm*) and ferromagnetic (*fm*) states at 25%. Results are shown in Figures V.II.1. The equilibrium lattice parameters, bulk modulus, and its pressure derivative follow from a fit of the total energy as a function of the volume to the Murnagahan equation of state [14]. The predicted values of the structural parameters and the difference energies ΔE_{fm-nm} between *fm* and *nm* states are listed in Table V.II.1. They are compared with values of the parents compounds AlN and GaN. We observe that those predicted results of AlN and GaN doped with Mn in the same order than the values of AlN and GaN compounds [73,77]. As shown in the Figures V.II.1 the ferromagnetic state has been found to be most stable energetically between the two states because the difference energies ΔE_{fm-nm} is positive. When we compare the lattice constants and bulk modulus in the case of spin polarized and unpolarized states, we observe an enhancement by 0.82% and 0.66% for GaN:Mn and AlN:Mn, respectively.

Table V.II.1. *Lattice constants a, bulk modulus B, and its pressure derivative B' and energy difference between fm and nm magnetic states ΔE_{fm-nm} of GaN:Mn and AlN:Mn at 25%.*

		a **(Å)**	***B*** **(GPa)**	***B'***	ΔE_{fm-nm}
GaN:Mn	*fm*	4.4643	204.7	3.74	0.745
	nm	4.4276	217.94	3.632	-
GaN		4.461	202	4.32	
AlN:Mn	*fm*	4.3726	208.5	3.74	0.966
	nm	4.343	218.41	3.861	-
AlN		4.349	211.78	3.90	

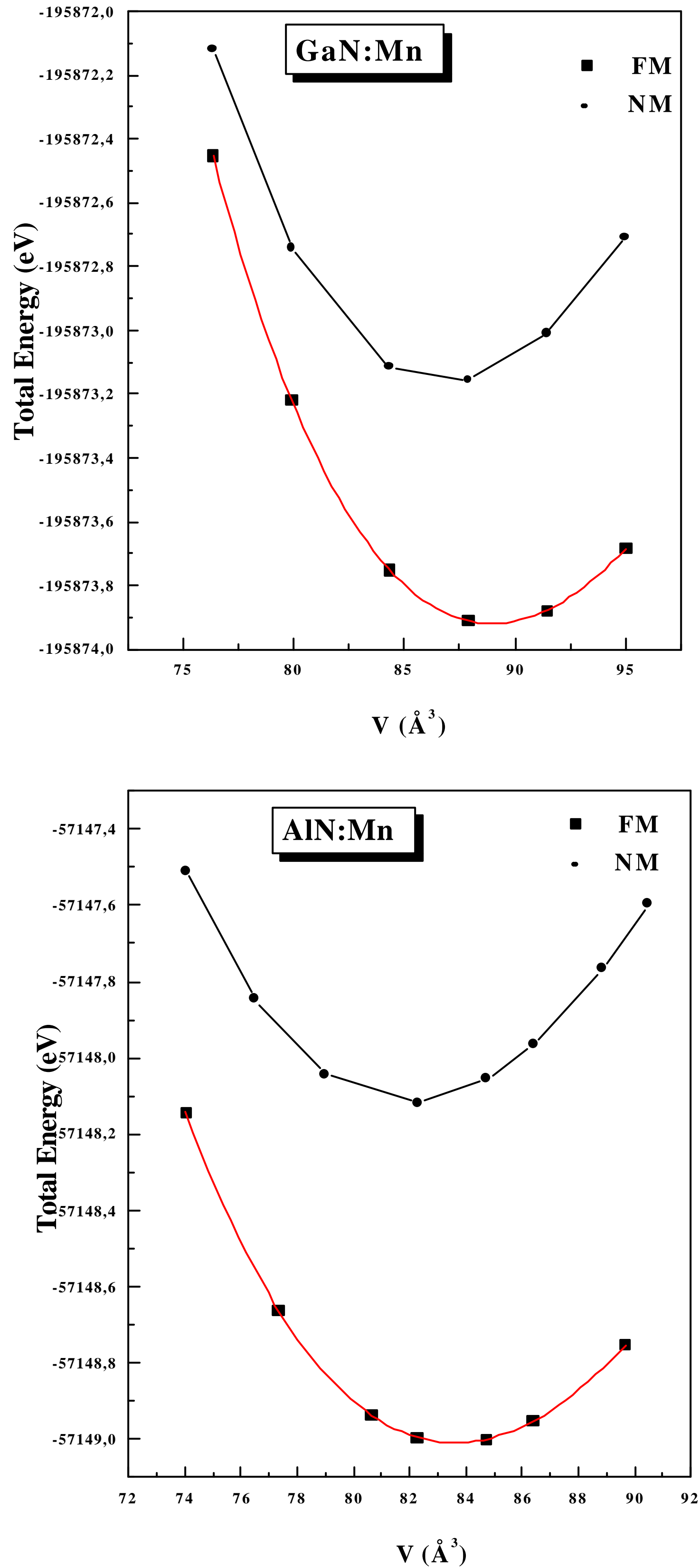

Figure V.II. 1. The variation of total energies with the total volume for nonmagnetic (*nm*) and ferromagnetic (*fm*) states of GaN:Mn and AlN:Mn systems.

V. II. 3. Electronic structures and magnetic properties

For magnetic systems, spin polarized calculations are performed using the concept of spin-up and spin-down electrons separately. The calculated total and partial densities of states (DOS) curves at the predicted equilibrium lattice constants for ferromagnetic GaN:Mn and AlN:Mn are shown in Figures V.II.2 and V.II.3. In comparison with Al and Ga, Mn has extra four valence electrons, which fill spin-up e_g and t_{2g} bands. The doubly degenerated band is fully occupied, while the triply degenerated band (higher in energy) is only two thirds filled so the Fermi level falls just into the latter 100% spin polarized band (see Figures V.II.3).

Furthermore we find the local magnetic moment of the Mn atom is ~3.0$\mathbf{m}_B$, $\mathbf{m}_B$ is the bohr magneton, for both GaN:Mn and AlN:Mn. This value is in good agreement with previous theoretical calculations [105-113]. Due to localization of spin-polarized charge around the Mn atom, this value is smaller than the total magnetic moment, which is ~4 $\mathbf{m}_B$. As a result, the total magnetic moment has an integer value 4$\mathbf{m}_B$. Moreover, our results show that the main part of this magnetic moment is strongly localized on the Mn site (see Table V.II.2). The additional contributions to the total magnetic moment appear to come from N and Ga (Al) atoms to Mn. When we observe more carefully the values of the different magnetic contributions reported in the table, the total magnetic moment is not the summation of magnetic contribution of the interstitial site and those of the individual atoms. This may be interpreted by the fact that the interstitial site is modeled by the average of the plane waves. This later cannot quantify all the interstitial site.

Table V.II. 2. *Total and local magnetic moments in GaN:Mn and AlN:Mn systems with a 25%.*

	GaN:Mn	AlN:Mn
M^{total} ($\mathbf{m}_B$/cell)	4.0	4.0
m^{Mn} ($\mathbf{m}_B$)	3.066	3.0
m^{N}	0.026	0.025
$M^{Gaa\ ou\ All}$	0.030	0.035
$m^{intersitiel}$	0.75	0.8

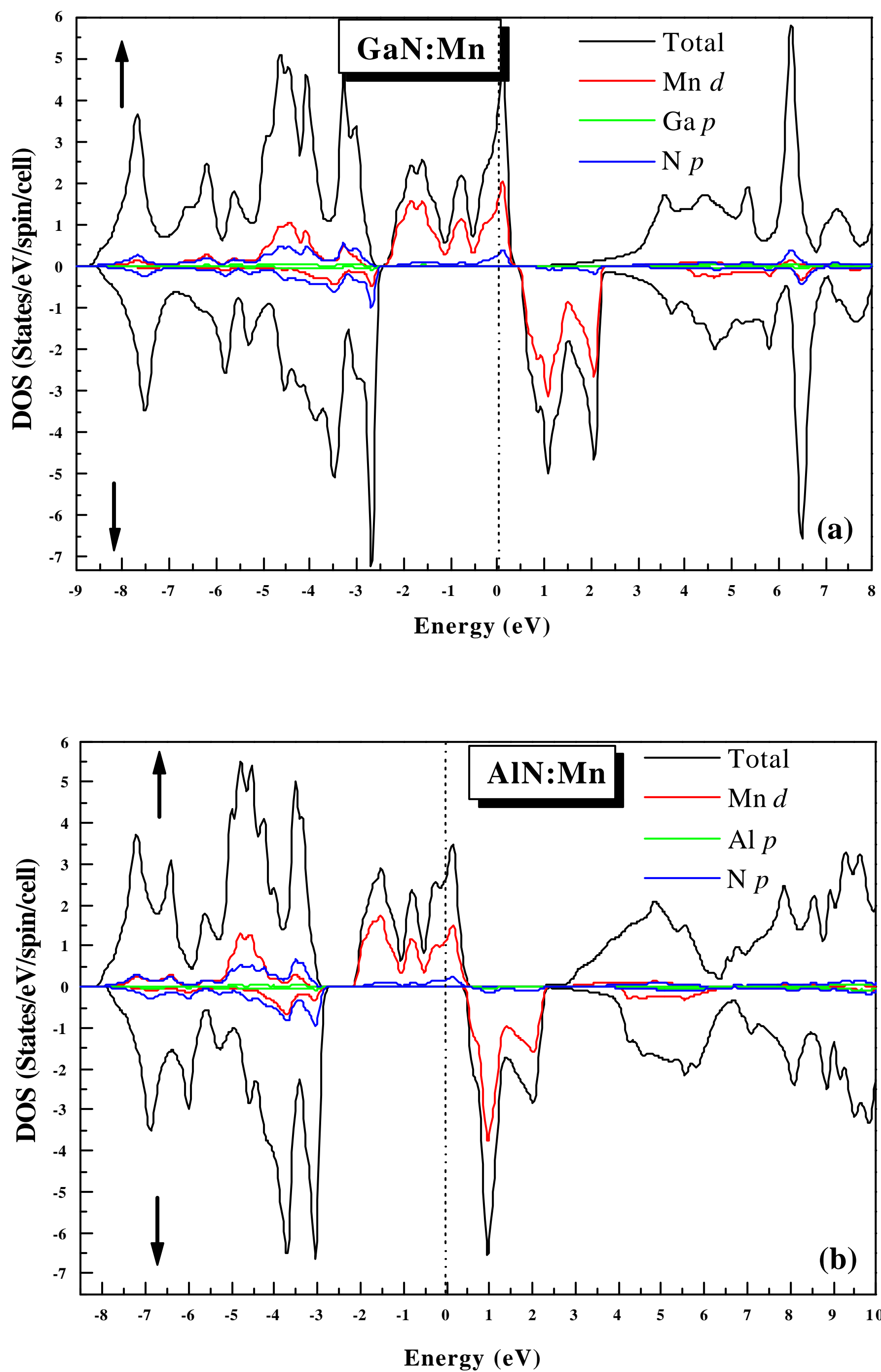

Figure V.II.2. Total and local partial densities of states in the ferromagnetic of (a) GaN:Mn (b) AlN:Mn at 25% of Mn.

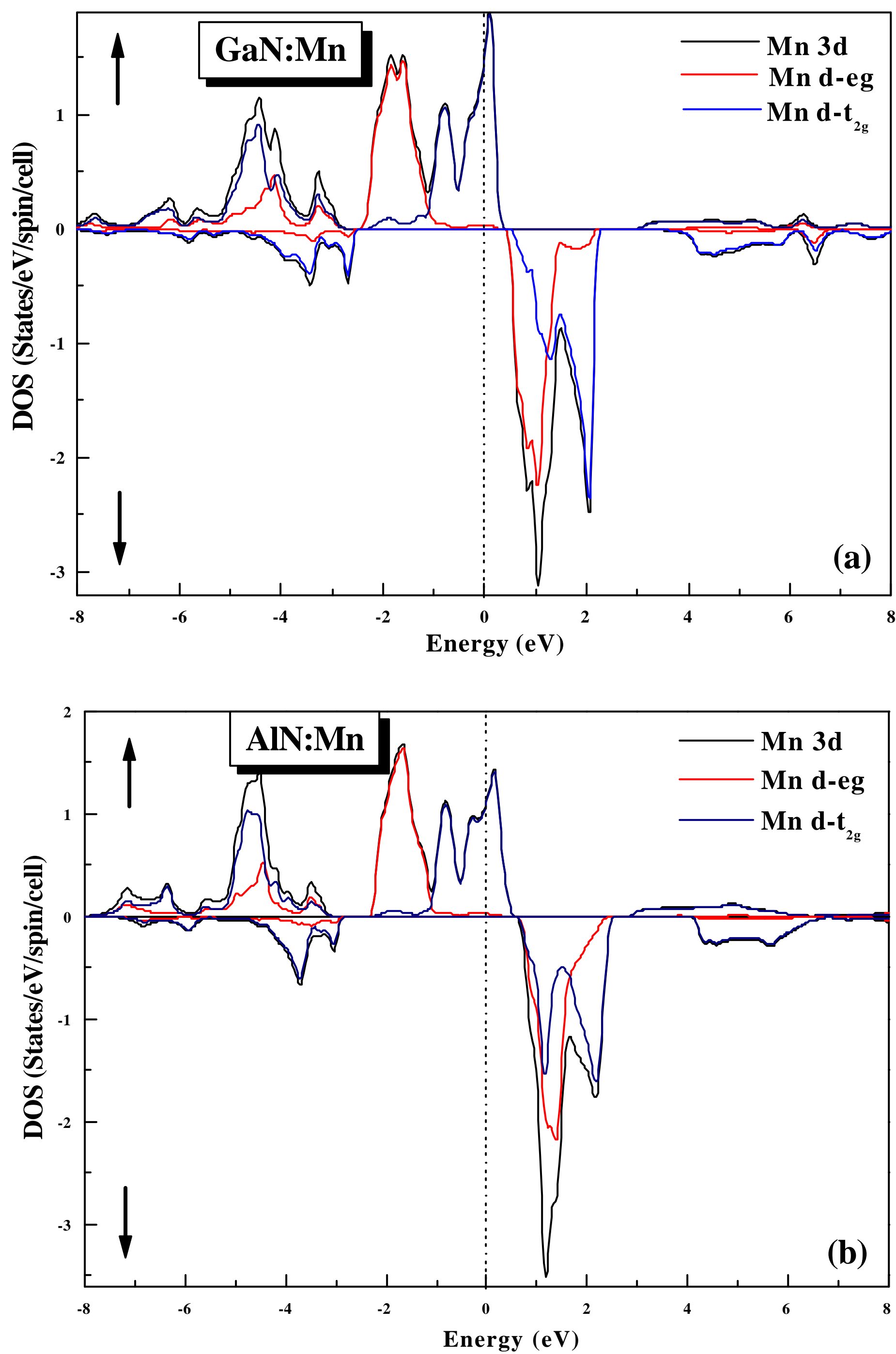

Figure V.II.3. Partial densities of states of Mn impurity in the ferromagnetic of (a) GaN:Mn (b) AlN:Mn at 25% of Mn. Peaks for majority and minority e_g and t_{2g} states are labelled.

In Figures V.II.4 and V.II.5, we present the corresponding spin-dependent energy bands along high-symmetry directions in the Brillouin zone for GaN:Mn and AlN:Mn. There are three bands slightly crossing the Fermi energy. One of them is almost fully filled, but the other two are approximately half-filled. There is a narrow energy gap (0.326 eV for GaN:Mn and 1.334 eV for AlN:Mn) of the majority-spin electrons, separating the bands derived from the valence and conduction bands of the host. For the minority-spin electrons, the band gap is much wider 2.05 eV and 3.24 eV of GaN:Mn and AlN:Mn, respectively, and the top of the valence band is reduced to under the Fermi Level. Since the exchange splitting ($\Delta E_{xc} \equiv$ 3.04eV for GaN:Mn and $\Delta E_{xc} \equiv$ 1.93eV for AlN:Mn) between the majority and minority is larger than the crystal field splitting ($\Delta E_{cryst} \equiv$ 1.71eV for GaN:Mn and $\Delta E_{cryst} \equiv$ 1.85eV for AlN:Mn) between the $d\text{-}t_{2g}$ and de_g (see Figures V.II.3).

Our calculations also show that the total $3d$ electron population within the Mn sphere in GaN:Mn and AlN:Mn is around 4.58 and 4.606, respectively, i.e., the atomic configuration of Mn is compatible with both $3d^4$ and $3d^5$. This result is in good agreement with the results obtained in Refs. [105,109-113].

For understating the origin of the spin-polarized feature in the DOS curves, we calculated patial DOS curves for the GaN:Mn and AlN:Mn. The N $2p$, Ga $4p$, Al $3p$, and Mn $3d$ contributions to the DOS are found in Figures V.II.2. It is readily apparent that the Mn $3d$ states hybridize strongly with N $2p$ states, and to a much lesser extent with Ga $4p$ and Al $3p$ states. However, for the spin-up states the Mn $3d$ states contribute roughly as much the original cation states, even though the Mn concentration is much lower than the Ga and Al one.

The spatial distribution of impurity states is intimately linked with the value of magnetic moments on different atoms. Table V.II.2 shows that the main contribution to magnetic moments comes from Mn atoms. In GaN:Mn and AlN:Mn, magnetic moments of all atoms are parallel. This may be interpreted as a tunneling of spin-up impurity states to neighboring atoms. In this way, parallel or antiparallel orientation of magnetic moments on the atoms nearest to Mn may be considered as a signal that impurity states are either localized or strongly hybridized with the valence band.

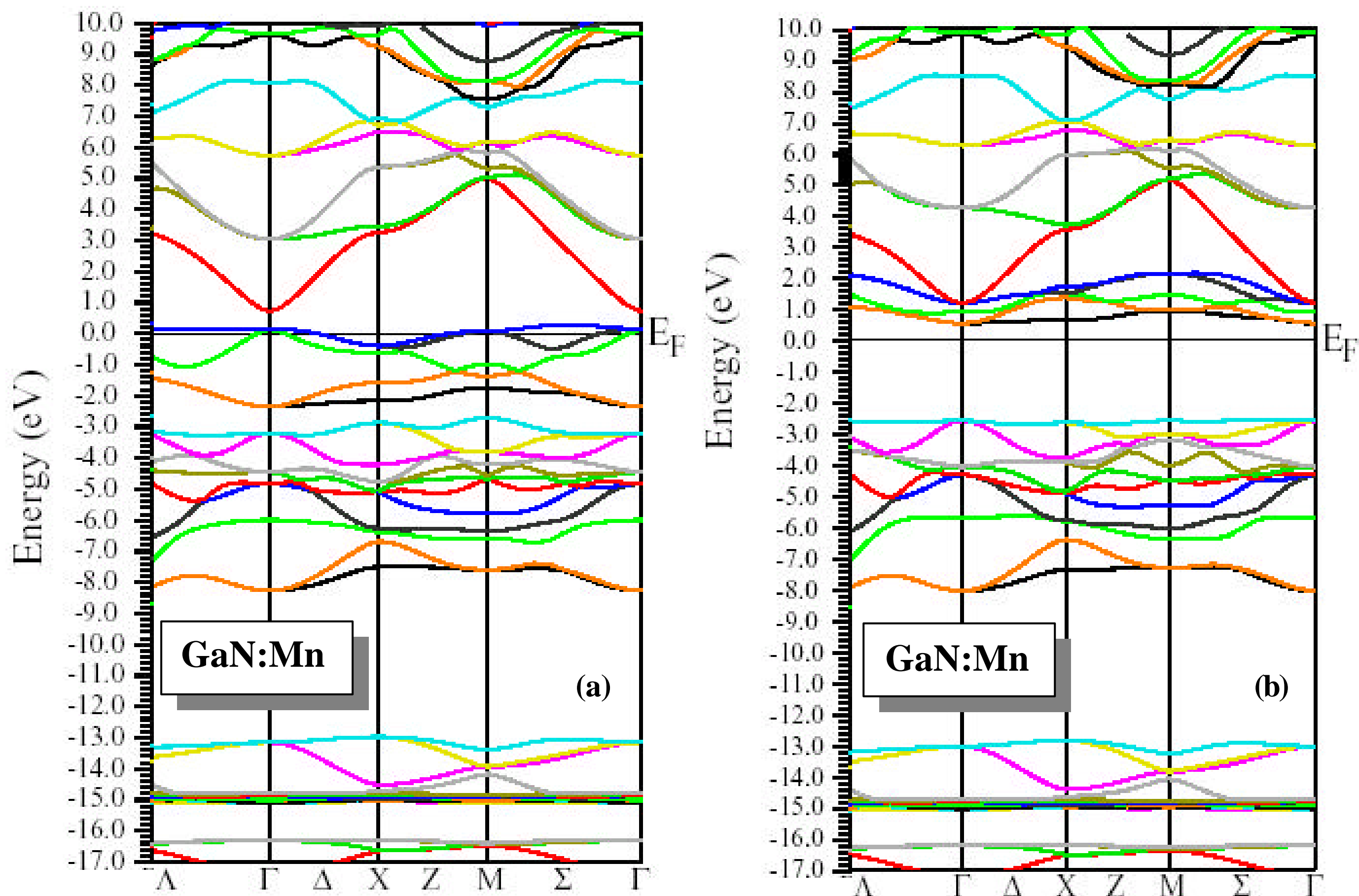

Figure V.II.4. Spin polarized band structure of GaN:Mn system, (a) majority spin and (b) minority spin

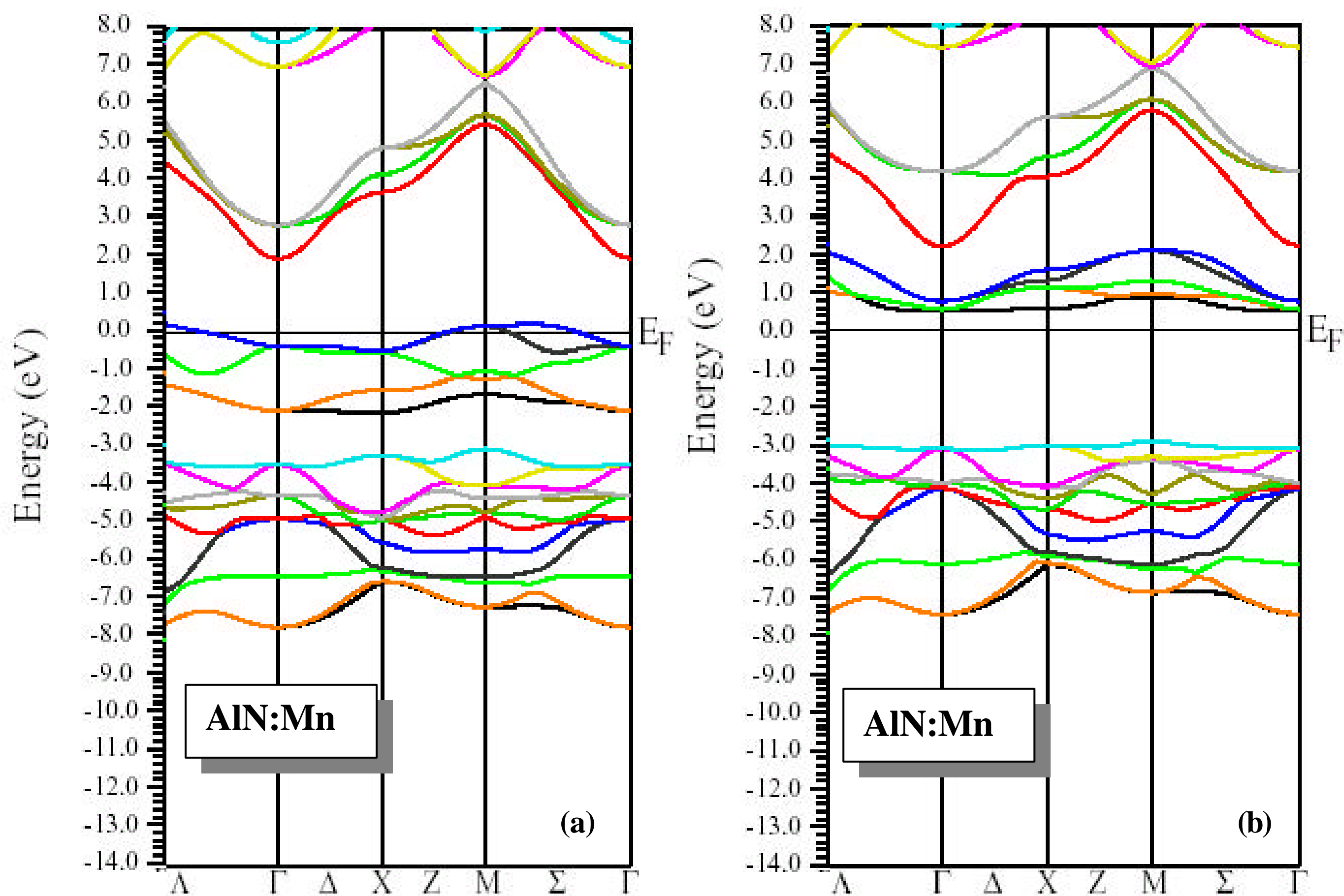

Figure V.II.5. Spin polarized band structure of AlN:Mn system, (a) majority spin and (b) minority spin

V. II. 4. The exchange coupling

We calculate the exchange constant by evaluating the spin-splitting of the conduction and valence bands. The main idea is that in the mean field theory based on the Hamiltonian model [111], the spin-splitting of the valence band depends linearly on the exchange constant $N_0\beta$ [111]. The same argument holds for the spin-splitting of the conduction band, which is regulated by a similar Hamiltonian with exchange constant $N_0\alpha$. Therefore the exchange constants can be directly computed from the conduction band-edge (valence band-edge) spin-splittings as follows:

$$N_0\,\alpha = \frac{\Delta E^c}{x\langle S\rangle}\,; \quad N_0\,\beta = \frac{\Delta E^v}{x\langle S\rangle} \qquad \text{(V-II-1)}$$

Where $\langle S\rangle$ is half of the computed magnetization per Mn ion.

Using the calculated band structures and $\langle S\rangle$ value for GaN:Mn and AlN:Mn, we have calculated the $N_0\alpha$ and $N_0\beta$. Our predicted values of ΔE^c, ΔE^v, $N_0\alpha$ and $N_0\beta$ are listed in Table V.II.3 for GaN:Mn and AlN:Mn systems. From Table V.II.3 one can conclude that the exchange coupling (s-d coupling) between the conduction band of Ga(Al)N and the Mn is ferromagnetic .

Table V.II. 3. *Conduction ΔE^c and valence ΔE^v band-edge spin-splitting, and exchange constants for GaN:Mn and AlN:Mn with a 25%.*

	GaN:Mn	AlN:Mn
ΔE^c	0.164	0.245
ΔE^v	-2.909	-2.3
$N_0\alpha$	0.328	0.5
$N_0\beta$	-5.81	-4.6

[1] P. Blaha, K. Schwarz, G.K.H. Madsen, D. Kvasnicka and J. Luitz, **WIEN2k**, *An Augmented-Plane-Wave + Local Orbitals Program for Calculating Crystal Properties* (Karlheinz Schwarz, Techn Wien, Austria), 2001. ISBN 3-9501031-1-2.

[2] R. Dreizler and E. K.U. Gross, *Density-Functional Theory* (Springer, New York, 1990).

[3] J.P. Perdew, S. Burke and M. Ernzerhof, Phys. Rev. Lett. **77**, 3865 (1996).

[4] D.M. Ceperley and B.J. Alder, Phys. Rev. Lett. **45**, 556 (1980).

[5] J.P. Perdew and Y. Wang, Phys. Rev. B **45**, 13 244 (1992).

[6] K. Schwarz and P. Blaha, Comput. Mater. Sci. **28**, 259 (2003).

[7] K. Schwarz, J. Solid. Stat. Chem. **176**, 319 (2003).

[8] G.H.K. Madsen, P. Blaha, K. Schwarz, E. Sjöstedt, L. Nordström, Phys. Rev. B **64**, 195134-1 (2001).

[9] K. Schwarz, P. Blaha, G.K.H. Madsen, Comput. Phys. Commun. **147**, 71 (2002).

[10] G.H.K. Madsen, B.B. Iversen, P. Blaha, K. Schwarz, Phys. Rev. B **64**, 195102-1-6 (2001).

[11] D.D. Koelling and B.N. Harmon, J. Phys. C **10**, 3107 (1977).

[12] H.J. Monkhorst and J.D. Pack, Phys. Rev. B **13**, 5188 (1976).

[13] *Properties of Group III Nitrides*, edited by J.H. Edgar, Electronic Materials Information Service (EMIS) Datareviews Series (Institution of Electrical Engineers, London, 1994).

[14] F.D. Murnaghan, Proc. Natl. Acad. Sci. USA **30**, 244 (1944).

[15] A. Trampert, O. Brandt and K.H. ploog, in *Crystal Structure of Group III Nitrides*, edited by J.I. Pankove and T.D. Moustakas, Semiconductors and Semimetals Vol. 50 (Academic, San Diogo 1998).

[16] M.E. Sherwin and T.J. Drummond, J. Appl. Phys. **69**, 8423 (1991).

[17] C.-Y. Yeh, Z. W. Lu, S. Froyen, and A. Zunger, Phys. Rev. B **46**, 10 086 (1992).

[18] V. Fiorentini, M. Methfessel, and M. Scheffler, Phys. Rev. B **47**, 13 353 (1993).

[19] L. Wenchang, Z. Kaiming, and X. Xide, J. Phys. Condens. Matter **5**, 875 (1993).

[20] K. Miwa and A. Fukumoto, Phys. Rev. B **48**, 7897 (1993).

[21] K. Kim, W. R. L. Lambrecht, and B. Segall, Phys. Rev. B **50**, 1502 (1994).

[22] N.E. Christensen and I. Gorczyca, Phys. Rev. B **50**, 4397 (1994).

[23] A. Rubio, J. L. Corkill, M.L. Cohen, E.L. Shirley, and S.G. Louie, Phys. Rev. B **48**, 11 810 (1993).

[24] A.F. Wright and J. S. Nelson, Phys. Rev. B **50**, 2159 (1994),

[25] A.F. Wright and J. S. Nelson, Phys. Rev. B **51**, 7899 (1995),

[26] K. Kim, W. R. L. Lambrecht, and B. Segall, Phys. Rev. B **53**, 16 310 (1996).

[27] A.F. Wright, J. Appl. Phys. **82**, 2833 (1997).

[28] D. Vogel, P. Krueger, and J. Pollmann, Phys. Rev. B **55**, 12 836 (1997).

[29] M.B. Nardelli, K. Rapcewicz, J. Bernholc, Phys. Rev. B **55**, R7323 (1997).

[30] M. Van Schilfgaarde, A. Sher and A.-B. Chen, J. Cryst. Growth. **178**, 8 (1997).

[31] K. Shimada, T. Sota, and K. Suzuki, J Appl. Phys. **84**, 4951 (1998).

[32] K. Karch, J.-M. Wagner, and F. Bechstedt Phys. Rev. B **57**, 7043 (1998).

[33] C. Stampfl and C.G. Van de Walle, Phys. Rev. B **59**, 5521 (1999).

[34] F. Bechstedt, U. Grossner and J. Furthmüller, Phys. Rev. B **62**, 8003 (2000).

[35] Zoroddu, F. Bernardini, P. Ruggerone and V. Fiorentini, Phys. Rev. B **64**, 045208 (2001).

[36] M. Fuchs, J.L.F. Da Silva, C. Stampfl, J. Neugebeaur, and M. Scheffler, Phys. Rev B **65**, 245212 (2002).

[37] V.I. Gavrilenko and R.Q. Wu, Phys. Rev. B **61**, 2632 (2000).

[38] I. Vurgaftmana and J. R. Meyer L. R. Ram-Mohan, J. Appl. Phys. **89**, 5815 (2001); I. Vurgaftman and J. R. Meyer, J. Appl. Phys. 94, 3675 (2003).

[39] A. Munoz, K. Kunc, Physica B **185**, 422 (1993).

[40] S. Goumri-Said, M.B. Kanoun, A.E. Merad, G. Merad and H. Aourag, Chemical Physics **302**, 135 (2004).

M.B. Kanoun, A.E. Merad and G. Merad. « Equilibrium and thermodynamic properties of GaN using a three body potential » *Second International Congress on Materials Sciences and Engineering - CISGM'2001* - Annaba, Algeria; November 13 and 14, 2001.

[41] T. Lei, M. Fanciulli, R.J. Molnar, and T.D. Moustakas, Appl. Phys. Lett. **59**, 944 (1991).

[42] J.H. Edgar, J. Mater. Res. **7**, 235 (1992).

[43] M. Abu-Jafara, A.I. Al-Sharifb, A. Qteish, Solid Stat. Comm. **116**, 389 (2000).

[44] J.-M. Wagner and F. Bechstedt, Phys. Rev. B **66**, 115202-1 (2002)

[45] J.C. Phillips, *Bonds and Bands in Semiconductors* (New York: Academic), 1973.

[46] Q. Xia, H. Xia, and A.L. Ruoff, J. Appl. Phys. **73**, 8198 (1993).

[47] S. Uehara, T. Masamoto, A. Onodera, M. Ueno, O. Shimomura, and K. Takemura, J. Phys. Chem. Solids **58**, 2093 (1997).

[48] H. Xia, Q. Xia, and A.L. Ruoff, Phys. Rev. B **47**, 12 925 (1993).

[49] J. Serrano, A Rubio, E. Hernandez, A. Munoz and A. Mujica, Phys. Rev. B **62**, 16612 (2000).

[50] W.H. Moon and H. J. Hwang, Phys. Lett. A **315**, 319 (2003).

[51] P. Perlin, C. Jauberthie-Carillon, Lti, A.S. Miguel, I. Grzegory, A. Polian, High Press. Res. **7**, 96 (1991).

[52] P. Perlin, C. Jauberthie-Carillon, Lti, A.S. Miguel, I. Grzegory, A. Polian, Phys. Rev. B **45**, 83 (1992).

[53] M. Ueno, M. Yoshida, A. Onodera, O. Shimomura, Takemura, Phys. Rev. B **49**, 49 (1994).

[54] A. Munoz, K. Kunc, Phys. Rev. B **44**, 10 372 (1991).

[55] H. Vollstädt, E. Ito, M. Akaishi, S. Akimoto, and O. Fukunaga, Proc. Jpn. Acad., Ser. B: Phys. Biol. Sci. **66**, 7 (1990).

[56] A. Munoz, K. Kunc, Comput. Mater. Sci. **2**, 400 (1994).

[57] M.J. Paisley, Z. Sitar, J.B. Posthill, R.F. Davis, J. Vac. Sci. Technol. A. **7**, 701 (1989).

[58] W.R.L. Lambrecht, B. Segall, S. Strite, G. Martin, A. Agarwal, H. Morkoc and A. Rockett, Phys. Rev. B **50**, 14155 (1994).

[59] S.K. Pugh, D.J. Dugdale, S. Brand and R.A. Abram, Semicond. Sci. Technol. **14**, 23 (1999).

[60] L.I. Berger, *Semiconductors Materials* (New York: Chemical Rubber Company) (1997) p 124.

[61] S.-H. Wei and A. Zunger, Phys. Rev. B **50**, 2719 (1996).

[62] M. Guadalupe, M. Armenta, A.R. Serrato and M.A. Borja, Phys. Rev. B **62**, 4890 (2000).

[63] S.A. Ding, S.R. Barman, K. Horn and V.L. Alpherovich, in Proceeding of ICPS-23, edited by M. Scheffler and R. Zimmermann (World Scientific, Singapore, 1996), p. 525.

[64] J. R. Chelikowsky and A. Jin, Phys. Rev. B **40**, 96644 (1989).

[65] P. E. Blöchl, O. Jepsen and O. K. Anderson Phys. Rev. B **49**, 16223 (1994).

[66] L. Pauling, *The Nature of the Chemical Bond* (New York: Cornell University Press), 1960.

[67] A. Garcia and M.L. Cohen, Phys. Rev. B **47**, 4215 (1993).

[68] M. Ferhat, A. Zaoui, M. Certier and B. Khelifa, Phys. Stat. Sol (b) **195**, 415 (1996).

[69] A. Tadjer, B. Abbar, M. Rezki, J.-P. Dufour, H. Aourag, M. Certier, Mat. Chem. Phys. **62**, 75 (2000).

[70] P.E. Van Camp, V.F. Van Doren and J.T. Devreesse Phys. Rev. B **44**, 9056 (1991); Solid State Commun. **81**, 23 (1992).

[71] C. Kittel, Introduction to Solid Physics, 6th Edition, Wiley, NewYork, 1986.

[72] T. Charpin, *A package for calculating elastic tensors of cubic phases using WIEN2k*, in User's Guide of WIEN2k, *An Augmented-Plane-Wave + Local Orbitals Program for Calculating Crystal Properties*, P. Blaha, K. Schwarz, G.K.H. Madsen, D. Kvasnicka and J. Luitz, Techn Wien, Austria), 2001. ISBN 3-9501031-1-2.

[73] M.B. Kanoun, A.E. Merad, J. Cibert, H. Aourag and G. Merad, Journal Alloys and Compounds **366**, 86 (2004).

[74] F. Grosse and J. Neugebauer, Phys. Rev B **63**, 085207 (2001).

[75] W.A. Harrison, *Electronic Structure and Properties of Solids* (Dover, New York, 1989).

[76] A.E. Merad, H. Aourag, B. Khelifa, C. Mathieu and G. Merad, Superlatt. and Microstruct. **30**, 241 (2001).

[77] A.E. Merad, M.B. Kanoun, J. Cibert, H. Aourag and G. Merad, Materials Chemistry and Physics **82**, 471 (2003).

[78] M. Posternak, A. Baldereschi, A Catellani and R. Resta, Phys. Rev. Lett. **64**, 1777 (1990).

[79] G.D. O'clock and M.T. Duffy, Appl. Phys. Lett. **23**, 55 (1973).

[80] K. Karch and F. Bechstedt, Phys. Rev. B **56**, 7404 (1997).

[81] S.Yu. Davydov and K. Tikhonov, Semiconductors **30**, 514 (1996).

[82] S. de Gironcoli, S. Baroni, and R. Resta, Phys. Rev. Lett. **62**, 2853 (1989).

[83] Dal Corso, R. Resta, and S. Baroni, Phys. Rev. B **47**, 16 252 (1993).

[84] S. de Gironcoli, S. Baroni, and R. Resta, Ferroelectrics **111**, 19 (1990).

[85] M. Kitamura, S. Muramatsu and W. A. Harrison, Phys. Rev. B **46**, 1351 (1992).

[86] R. Andre, J. Cibert, L.S. Dang, J. Zeman and M. Zigone, Phys. Rev. B **53**, 6951 (1996)

[87] A.E. Merad, M.B. Kanoun, H. Aourag, J. Cibert and G. Merad, Superlattices and Microstructures **32**, 25 (2002).

[88] S.-H. Wei and A. Zunger, Phys. Rev. B **60**, 5404 (1999).

[89] S. Fahy, K. J. Chang, S. G. Louie and M. L. Cohen, Phys. Rev. B **35**, 5856 (1987).

[90] G. Steude, B.K. Meyer, A. Goldner, A. Hoffmann, F. Bechstedt, H. Amano, and I. Amano and I. Akasaki, Jpn, J. Appl Phys. **38**, L498 (1999).

[91] H. Gleize, F. Demangeot, J. Frandon, M.A. Renucci, F. Widmann and B. Daudin, Appl. Phys. Lett **74**, 703 (1999).

[92] A. Polian and M. Grimsditch, Phys. Rev. B **60**, 1468 (1999).

[93] M.J. Herrera-Cabrera, P. Rodriguez-Hernandez, M. Gonzalez-Diaz and A. Munoz, Phys. Stat. Sol. (b) **223**, 411 (2001).

[94] J.-M. Wagner and F. Bechstedt, Phys. Rev. **B 62**, 4526 (2000).

[95] M.B. Kanoun, A.E. Merad, G. Merad, J. Cibert and H. Aourag, Solid-State Electronics **48**, 1601 (2004).

[96] M.B. Kanoun, S. Goumri-Said, A.E. Merad, G. Merad, J. Cibert and H. Aourag, Semiconductor Science and Technology **19**, 1220 (2004)

[97] J. L. Sanchez-Rojas, A. Sacedon, F. Gonzalez-Sanz, E. Calleja and E. Munoz, Appl. Phys. Lett. **65**, 2042 (1994).

[98] P. Perlin, T. Suski, J.W. Ager III, G. Conti, A. Polian, N.E. Christensen, I. Gorczyca, I. Grzegory, E.R. Weber and E.E. Haller, Phys. Rev. B **60**, 1480 (1999).

[99] K. Karch and F. Bechstedt, Phys. Rev. Lett. **77**, 1660 (1996).

[100] B.A. Weinstein and G.J. Piermarini, Phys. Rev. B **12**, 1172 (1975); R. Trommer, H. Muller, M. Cardona, and P. Vogl, ibid. **21**, 4869 (1980); D. Diego, M. Cardona, and P. Vogl, ibid. **25**, 3878 (1982).

[101] M. Nelhiebel, P.H. Louf, P. Schattschneider, P. Blaha, K. Schwarz and B. Jouffrey, Phys. Rev. B. **59**, 12807 (1999).

[102] C. Hébert, J. Luitz and P. Schattschneider, Micron **34**, 219 (2003).

[103] S. Lazar, C. Hébert, H.W. Zandbergen, Ultramicroscopy (in press 2004).

[104] K. Lawniczak-Jablonska, T. Suski, I. Gorczyca, N.E. Christensen, K.E. Attenkofer, R.C.C. Perera, E.M. Gullikson, J.H. Underwood, D.L. Ederer and Z.L. Weber, , Phys. Rev. B. **61**, 16623 (2000).

[105] E. Kulatov, H. Nakayama, H. Mariette, H. Ohta and Yu. A. Uspenskii, Phys. Rev. B **66**, 045203 (2002).

[106] H. Katayama-Yoshida, K. Sato, J. Phys. Chem. Solid. **64**, 1447 (2003).

[107] K. Sato and H. Katayama-Yoshida, Semicond. Sci. Technol. **17**, 367 (2002).

[108] H. Katayama-Yoshida, R. kato and T. Yamamoto, J. Cryst. Growth **231**, 428 (2001).

[109] L. Kronik, M. Jain and J.R. Chelkowsky. Phys. Rev. B **66**, 041203 (2002).

[110] M. Van Schilfgaarde and O. N. Mryasov, Phys. Rev. B **63**, 233205 (2001).

[111] S. Sanvito, G. Theurich and N. A. Hill, Phys. Rev. B **63**, 165206 (2001).

[112] K. Sato and H. Katayama-Yoshida, Jpn. J. Appl. Phys. **40**, L485 (2001).

[113] M. Zajac, J. Gosk, M. Kaminska, A. Twardowski, T. Szyszko and S. Podsiadlo, Appl. Phys. Lett. **79**, 2432 (2001).

General Conclusion

The aim of this thesis was to determine the structural, elastic and electronic properties of III-nitrides, AlN and GaN, with emphasis on their dependence on hydrostatic pressure. Furthermore, we have also extended our work to study the effect of doping with Mn on the properties of AlN and GaN compounds. We have performed a newest first-principles FP-L/APW+lo calculations within the DFT method of AlN and GaN crystallizing in both wurtzite and zincblende structures. Optimal bulk geometries have been calculated by total-energy minimization. The Ga 3d semicore electrons have been explicitly increases treated as valence electrons. This d state gives rise to the $p-d$ coupling, which enormously the number of plane waves in the basis set. The main results of our work can be summarized as follow:

We have calculated the bulk properties and band structures in wurtzite, zincblende rocksalt phases using both LDA and GGA for exchange-correlation functional. We have found that using GGA the lattice constants are larger and the bulk modulus are smaller compared to LDA results. Therefore the GGA does not appear to bring about any essential improvement, when compared with experiment. The band structures are found to be very similar in the LDA and GGA, when calculated at the experimental lattice constant. When calculated at the appropriate theoretical lattice constants, some differences are found, with smaller bandgap in the case of GGA. The total energy calculations suggest that the AlN and GaN under pressure transform to the semiconducting rocksalt structure. This result is a manifestation of the large ionicity of the nitrides.

We notice that our calculations provide an excellent description of the band structures of AlN and GaN compounds. We conclude also that GGA and LDA-eigenvalue spectrum differ significantly from experimental observations, and generally agree more closely with other ab initio calculations. The curve of the DOS present the same aspect for both zincblende Al(Ga)N and wurtzite -Al(Ga)N. Furthermore, A detailed study of several densities of states have shown the origin of $p-p$ and $p-d$ coupling with N p state which is due to the non-negligible dispersions of Al p state and Ga d states inside the upper valence bands, respectively.

The charge densities have been presented the similarity of the bond in AlN and GaN for both ZB and WZ structures. Our results show a highly ionic bonding and a charge transfer from Al or Ga to N. One notices that the situation in the ZB structure is analogous to that of the WZ structure. Since both polytypes have the same tetrahedral environment, where the local coordination of the first neighbor atomic positions is the same in the zincblende and the wurtzite structures. Consequently, their ionicity values are very close.

Because of the importance of AlN and GaN compounds in the zincblende structure, we have emphasized our attention to study the stress effects on band structures via the bandgaps coefficients. The AlN and GaN bandgaps conserve their characteristics; they are still indirect and direct gaps, respectively. Moreover the calculation of the hydrostatic deformation potential constants for direct and indirect gaps gives us an approximation about the strain effect. This consolidates also the successful implementation of the used numerical method when comparing these results to theoretical works given recently for zincblende AlN and GaN.

When plotting the charge density for small compression, we found a high ionicity of AlN and GaN, which increase with increasing pressure. This is originated from the increase in the charge density around the anion site and it decreases around the cation site under pressure.

Our determined elastic constants and strain-internal parameter agree well with the recent reported results. It is found that these parameters are varying linearly when the pressure is varied. Our results may be considered as reliable predictions of the pressure dependence of the elastic properties and internal-strain parameter of zincblende AlN and GaN.

The piezoelectric constants and transverse effective charges of AlN and GaN were determined by mean of Harrison approach. The results show that III-V nitrides resemble II-VI compounds in terms of the sign of the piezoelectric constants, which are much larger in absolute value than those of all III-V and II-VI compounds. Some remnant of normal III-V-like behavior survives, embodied in the trends of the piezoelectric constants and transverse effective charges when the chemical identity of the anion or cation changes. From this

investigation, it is found that the piezoelectric properties and transverse effective charge is varying in nonlinear behavior when we apply a pressure.

The characteristic ELNES coordination fingerprints have also been reported and analysed for the selected AlN and GaN compounds. Theoretical spectras indicate the possibility to differentiate the various phases by looking at the changing in the number and position of peaks in both Al, N K and Ga $L_{2,3}$ edges.

We have also presented structural parameters, formation energies, magnetic properties and electronic structures of AlN:Mn and GaN:Mn systems. From total energy calculations, we have found that AlN:Mn and GaN:Mn have ferromagnetic ground states. The impurity states are located deep inside the gap, strongly localized near Mn atoms which is primarily due to hybridization of Mn 3*d* and N 2*p* orbitals. We predict that Mn-doped AlN and GaN will exhibit the half-metallic ferromagnetic. We have also deduced the exchange splitting (ΔE_{xc}) and crystal field splitting (ΔE_{cryst}) and have found that the effective potential for minority spin is more attractive than that for the majority spin as is usually in spin polarized systems. We have determined the exchange constants $N_0\alpha$ and $N_0\beta$, which imitate a typical magneto-optical experiment. The magnetic moments of all atoms are parallel and magnetic interaction of Mn atoms is short ranged and that the total magnetic moment is equal to $4\mu_B$. This unique feature, together with the previously suggested high Curie temperature and inherent compatibility with GaN technology, makes GaN:Mn a potentially ideal material for spin-injection applications. If technological limitations can be overcome, it may emerge as a significant material for modern spintronic devices.

Moreover these results constitute a preliminary step to future works dealing with superlattice, complex system semiconductors and to study the problem not solved up to now related to the DMSs.